DRAFT

KOPIO
Measurement of the decay $\mathrm{K^0_L} \rightarrow \pi^0 \nu \bar{\nu}$

DRAFT TECHNICAL DESIGN REPORT FOR THE NATIONAL SCIENCE FOUNDATION

0-draft ... June 06, 2001...

KOPIO COLLABORATION

I-H. Chiang, J.W. Glenn, D. Jaffe, D. Lazarus, K. Li, L. Littenberg*, G. Redlinger, M. Sivertz,
A. Stevens, R. Strand
Brookhaven National Laboratory

K. Kinoshita
University of Cinncinnati

A. Ivashkin, M. Khabibullin, A. Khotjanzev, Y. Kudenko, A. Levchenko, O. Mineev,
N. Yershov
INR, Moscow

G. Anzivino, P. Cenci, P. Lubrano, A. Nappi, M. Pepe, M. Valdata
INFN-University of Perugia†

M. Kobayashi, T. Taniguchi
KEK

R. Takashima
Kyoto University of Education

T. Nomura, N. Sasao
Kyoto University

M. Blecher, M. Pitt, B. Vogelaar
Virginia Polytechnic Institute & State University

B. Bassalleck, N. Bruner, D.E. Fields, J. Lowe, T.L. Thomas
University of New Mexico

M. Ito
Thomas Jefferson National Accelerator Facility

M. Marx, D. Schamberger
State University of New York at Stony Brook

P. Amaudruz, E. Blackmore, D. Bryman*, A. Daviel, M. Dixit‡, J. Doornbos, P. Gumplinger,
M. Hasinoff, R. Henderson, A. Konaka, J. Macdonald, T. Numao, R. Poutissou
TRIUMF/UBC

G. Atoyan, S.K. Dhawan, V. Issakov, H. Kaspar, A. Poblaguev, M.E. Zeller*
Yale University

E. Frlez, D. Pocanic
University of Virginia

P. Robmann, P. Truöl, A. van der Schaaf
University of Zurich

---

* co-spokesperson

† Subject to approval by INFN.

‡ Carleton University

TABLE OF CONTENTS

4.1 AGS
    Booster F3 and AGS A5 kicker magnet pulse forming networks
    RF Development for micro-bunched beam
    Measurements of bunch lengths
    Measurements of bunch width and extraction efficiency dependence on rf voltage
    Four dimensional modeling of bunch width
    Beam present between bunches
    Primary beam modifications
    Magnet reconfiguration
    Primary beam and collimator
    Shielding reconfiguration and power supply removal
    Primary beam instrumentation
    Production target and target station design
    Neutral Beam
    Neutral flux and spectra
    Sweeping magnet design
    Collimator design
    Downstream sweeping magnet
    Construction schedule

    Design concept
    Mechanical construction
    Drift chamber
    Scintillator
    Construction
    Module support and installation
    Electronics

1 Introduction

CP violation is one of the most important outstanding issues in the study of elementary particle physics. It has profound implications for the relationship among the quarks (and now, perhaps, the leptons), and for the origin of matter in the universe. Since its discovery in 1964, CP violation has been the exclusive province of the K sector. With the advent of the Standard Model (SM), the primary question has revolved around establishing whether or not the observed CP violation was due to the complex phase in the Cabibbo-Kobayashi-Masakawa (CKM) quark-mixing matrix *i.e.* direct CP violation. Evidence supporting this picture was obtained in measurements of $K \rightarrow \pi\pi$ decays (ϵ'/ϵ) at CERN and Fermilab, although without a precise theoretical interpretation for the underlying parameters. CP-violating phenomena are also being vigorously pursued in the B sector which has great promise for revealing a rich new phenomenology. An array of major thrusts are underway to study CP violation in B decays such as the newly upgraded CDF experiment at the Tevatron, and several new experiments/accelerators constructed specifically for this purpose, including BaBar at SLAC's PEP-II, and BELLE at KEKB, LHCb, and the recently approved BTeV at Fermilab. Among many possible measurements relating to CP violation four "golden" processes which stand out as theoretically unambiguous will allow complete elucidation of CP violation in the SM. Two are the quarry of the B experiments mentioned above, asymmetries in $B \rightarrow \psi K_s$ decays and the ratio of B_s to B_d mixing, and two are the branching ratios of the charged and neutral $K \rightarrow \pi\nu\overline{\nu}$ decays.

Despite the great depth of activity in B physics, it has become evident that the single most incisive measurement in the study of direct CP violation is the measurement of the branching ratio for $K_L^0 \rightarrow \pi^0\nu\bar{\nu}$ (B$(K_L^0 \rightarrow \pi\nu\bar{\nu})$). In the SM B$(K_L^0 \rightarrow \pi\nu\bar{\nu})$ is a unique quantity which directly measures the area of the CKM unitarity triangles *i.e.* the physical parameter that characterizes all CP violation phenomena, or the height of the triangle. Measurements of both B$(K_L^0 \rightarrow \pi\nu\bar{\nu})$ and B$(K^+ \rightarrow \pi^+\nu\bar{\nu})$ (E787/E949 at BNL[1]) will allow the triangle to be reconstructed unambiguously from K decay information alone. Thus, the KOPIO measurement of B$(K_L^0 \rightarrow \pi\nu\bar{\nu})$ will add a vital new dimension to the world-wide effort to elucidate the nature of CP violation.

The $K_L^0 \rightarrow \pi^0\nu\bar{\nu}$ decay mode is also unique in that it is completely dominated by direct CP violation[3] and is governed entirely by short-distance physics involving the top quark. Theoretical uncertainties are extremely small because hadronic effects can be extracted from the well measured decay $K^+ \rightarrow \pi^0 e^+\nu$. Thus, the measurement of B$(K_L^0 \rightarrow \pi\nu\bar{\nu})$ will provide a standard against which all other CP violating observables will be compared, and even small deviations from expectations will unambiguously signal the presence of new physics. Using current estimates for SM parameters, B$(K_L^0 \rightarrow \pi\nu\bar{\nu})$ is expected to lie in the range $(3.1 \pm 1.3) \times 10^{-11}$[2].

The experimental aspects of measuring B$(K_L^0 \rightarrow \pi^0\nu\bar{\nu})$ are quite challenging. The mode is a three body decay where only a π^0 is observed. There are competing decays which also yield π^0s, but whose branching ratios are millions of times larger. And observing a decay mode with a branching ratio on the order of 3×10^{-11} requires a prodigious number of kaons in order to achieve the desired sensitivity. Because the measurement is so demanding a detection technique must be adoped that provides maximum possible redundancy for this kinematically unconstrained decay, that has an optimum system for insuring that the observed π^0 is the only observable particle emanating from the K_L^0 decay, and that has multiple handles for identifying possible small backgrounds that might simulate the signal. It is with these issues in mind that the KOPIO experiment has been designed.

KOPIO employs a low energy, time structured K_L^0 beam to allow determination of the incident kaon momentum. The intense beam required, with its special characteristics, can be provided only by the BNL Alternating Gradient Synchrotron (AGS) which is available for use during the operation of the Relativistic Heavy Ion Collider (RHIC). Utilizing low momentum also permits a detection system for the π^0 decay photons that yields a fully constrained reconstruction of the π^0 mass, energy, and, momentum. The system for vetoing extra particles is also well understood. These features, which are similar to those employed successfully in the E787 measurement of $K^+ \rightarrow \pi^+\nu\bar{\nu}$, provide the necessary redundancy and checks. The goal of KOPIO is to obtain about 40 $K_L^0 \rightarrow \pi^\circ\nu\overline{\nu}$ events with a signal to background ratio of at least 2:1. This will yield a statistical uncertainty in the measurement of the area of the CKM unitarity triangle of about 10%. While $K_L^0 \rightarrow \pi^0\nu\bar{\nu}$ is clearly the focus of KOPIO, many other radiative-type K decays of significant interest for study of low energy QCD, and numerous searches for non-SM processes will also be accessed simultaneously.

2 Theory

2.1 $K_L^0 \to \pi^0\nu\bar{\nu}$ – Theoretical Motivation

Standard Model

Understanding the phenomenology of quark mixing and CP violation is currently one of the central goals of particle physics. Examining the CKM ansatz of the Standard Model (SM) through precise determination of its basic parameters, several of which are poorly known at present, is crucial. To assure a clear interpretation of experimental results, the ideal observable must not only be sensitive to fundamental parameters, but must also be calculable with little theoretical ambiguity.

The rare decay $K_L^0 \to \pi^0\nu\bar{\nu}$ is unique among potential SM observables; it is dominated by direct CP violation[1] and is governed entirely by short-distance physics involving the top quark (for general reviews see[2,3]). Long distance effects have been shown to be negligible[4]. Theoretical uncertainties are extremely small because the hadronic matrix element can be extracted from the well-measured decay $K^+ \to \pi^0 e^+\nu$, where small isospin breaking effects have been calculated[5]. Since the dominant uncertainty due to renormalization scale dependence has been practically eliminated by including next-to-leading-order QCD corrections, the remaining theoretical uncertainty for $B(K_L^0 \to \pi^0\nu\bar{\nu})$ is reduced to $\sim 2\%$.

$K_L^0 \to \pi^0\nu\bar{\nu}$ is a flavor-changing neutral current (FCNC) process that is induced through loop effects in the Standard Model. The leading electroweak diagrams are shown in Fig. 1. The expression for the $K_L^0 \to \pi^0\nu\bar{\nu}$ branching ratio can be written as

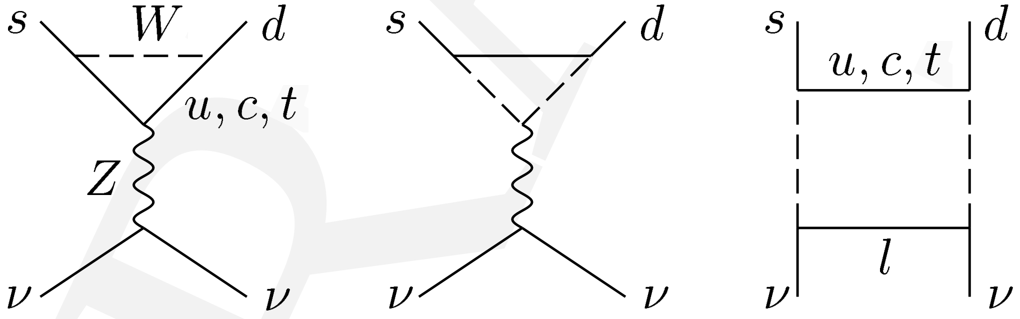

Fig. 1. The leading electroweak diagrams inducing $K_L^0 \to \pi^0\nu\bar{\nu}$.

$$B(K_L^0 \to \pi^0\nu\bar{\nu}) = r_{IB}\frac{B(K^+ \to \pi^0 e^+\nu)}{|V_{us}|^2}\frac{\tau(K_L^0)}{\tau(K^+)}\frac{3\alpha^2}{2\pi^2\sin^4\Theta_W}[Im(V_{ts}^*V_{td})X(x_t)]^2 \qquad (1)$$

where

$$X(x) \equiv \eta_X \cdot \frac{x}{8}\left[\frac{x+2}{x-1} + \frac{3x-6}{(x-1)^2}\ln x\right] \qquad \eta_X = 0.994 \qquad (2)$$

and $x_t = m_t^2/M_W^2$. Here the appropriate top quark mass to be used is the running $\overline{MS}$ mass, $m_t \equiv \bar{m}_t(m_t)$, which is related by $\bar{m}_t(m_t) = m_t^*(1 - 4/3 \cdot \alpha_s(m_t)/\pi)$ to the pole mass m_t^* measured in collider experiments. With this choice of mass definition the QCD correction factor is given by $\eta_X = 0.994$ and is essentially independent of m_t[6–8]. The coefficient $r_{IB} = 0.944$ summarizes the leading isospin breaking corrections in relating $B(K_L^0 \to \pi^0 \nu\bar{\nu})$ to $B(K^+ \to \pi^0 e^+ \nu)$[5].

$K_L^0 \to \pi^0 \nu\bar{\nu}$ is driven by direct CP violation due to the CP properties of K_L, π^0 and the relevant short-distance hadronic transition current. Since K_L^0 is predominantly a coherent, CP odd superposition of K^0 and $\bar{K}^0$, only the imaginary part of $V_{ts}^* V_{td}$ survives in the amplitude. Since the value of the sine of the Cabibbo angle is well known ($|V_{us}| = \lambda = 0.2205$), this quantity is equivalent to the Jarlskog invariant, $\mathcal{J} \equiv -Im(V_{ts}^* V_{td} V_{us}^* V_{ud}) = -\lambda(1 - \frac{\lambda^2}{2}) Im(V_{ts}^* V_{td})$. $\mathcal{J}$, in turn, is equal to twice the area of any of the six possible unitarity triangles[9]. A comparison of the area of any unitarity triangle obtained indirectly through studies of the B system or otherwise with the same quantity obtained directly from $K_L^0 \to \pi^0 \nu\bar{\nu}$ is then a critical test of the SM explanation of CP violation.

To facilitate the SM prediction of $B(K_L^0 \to \pi^0 \nu\bar{\nu})$ and exhibit its relation to other measurements, we employ the Wolfenstein parametrization (λ, A, ϱ, η) of the CKM matrix, which allows a display of unitarity in a transparent way. In this representation, Eq. 1 can be recast as

$$B(K_L^0 \to \pi^0 \nu\bar{\nu}) = 1.8 \cdot 10^{-10} \eta^2 A^4 X^2(x_t) \tag{3}$$

Inserting the current estimates for SM parameters into Eq. 3, the branching ratio for $K_L^0 \to \pi^0 \nu\bar{\nu}$ is expected to lie in the range $(3.1 \pm 1.3) \cdot 10^{-11}$[8]. The unitarity relation

$$1 + \frac{V_{td} V_{tb}^*}{V_{cd} V_{cb}^*} = -\frac{V_{ud} V_{ub}^*}{V_{cd} V_{cb}^*} \equiv \bar{\varrho} + i\bar{\eta} \tag{4}$$

determines the most commonly discussed triangle in the $(\bar{\varrho}, \bar{\eta})$ plane. Here $\bar{\varrho} = \varrho(1 - \lambda^2/2)$ and $\bar{\eta} = \eta(1 - \lambda^2/2)$. This unitarity triangle is illustrated in Fig. 2. A clean measure of its height is provided by the $K_L^0 \to \pi^0 \nu\bar{\nu}$ branching ratio. We note that, all other parameters being known, Eq. 3 implies that the relative error on η is half that on $B(K_L^0 \to \pi^0 \nu\bar{\nu})$. Thus, for example, a 15% measurement of $B(K_L^0 \to \pi^0 \nu\bar{\nu})$ can in principle determine η to 7.5%.

To construct the complete unitarity triangle in the K system, the charged mode $K^+ \to \pi^+ \nu\bar{\nu}$ which is closely related to $K_L^0 \to \pi^0 \nu\bar{\nu}$ is also needed. However, $K^+ \to \pi^+ \nu\bar{\nu}$ is not CP violating and receives a non-negligible charm contribution leading to a slightly higher theoretical uncertainty (about 5%)[10]. Measurement of $B(K^+ \to \pi^+ \nu\bar{\nu})$ allows the extraction of $|V_{td}|$ with the least theoretical uncertainty. The first evidence for $K^+ \to \pi^+ \nu\bar{\nu}$ was reported by E787 in 1997[11], and their latest result[12] gives a branching ratio, B($K^+ \to \pi^+ \nu\bar{\nu}$) $= (1.5^{+3.4}_{-1.2}) \times 10^{-10}$, that is twice as high as the central SM prediction (although statistically consistent with it). Analysis of substantial additional data is ongoing and will indicate whether there is consistency with the SM prediction. Together with $B(K_L^0 \to \pi^0 \nu\bar{\nu})$ the unitarity triangle is completely determined as shown in Fig. 2. Only a few other possible SM observables (*e.g.* x_s/x_d, $B \to l^+ l^-$ or certain CP asymmetries in B decays) provide similar opportunities for unambiguously revealing SM effects.

The pure B-system alternative to obtaining $\bar{\varrho}$ and $\bar{\eta}$ from $K \to \pi\nu\bar{\nu}$ discussed most frequently requires measuring B^0 or $\bar{B}^0 \to \pi\pi$ and B^0 or $\bar{B}^0 \to J/\psi K_S^0$. At B factories,

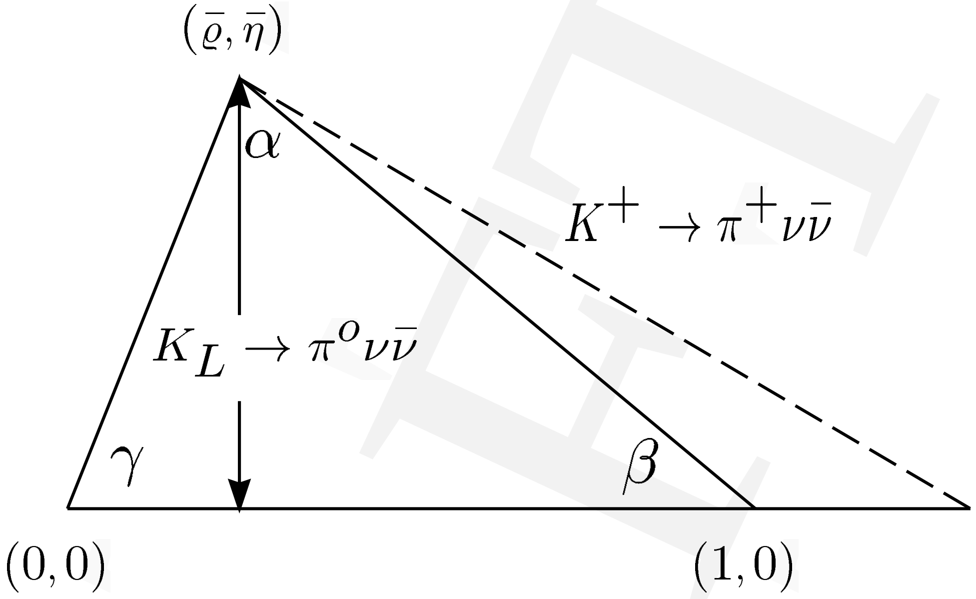

Fig. 2. The unitarity triangle.

the time-dependent asymmetry in the rate between B^0 and $\bar{B}^0$ must be measured in both cases. At hadronic colliders, both the time-dependent and time-integrated asymmtry can e used. These CP violating asymmetries measure $\sin 2\alpha$ and $\sin 2\beta$, respectively, and could in principle be used to infer $\bar{\varrho}$ and $\bar{\eta}$ (Fig. 2), completing the CKM determination. However, the extraction of $\sin 2\alpha$ from $B \to \pi\pi$ is complicated by the presence of penguin contributions. If only the channel $B_d \to \pi^+\pi^-$ is used, these contributions introduce potentially sizable theoretical uncertainties[13]. On the other hand, avoiding penguin effects requires a careful isospin analysis and a combination of several modes, including the challenging decay $B_d \to \pi^0\pi^0$. Also, inferring $\bar{\varrho}$ and $\bar{\eta}$ from $\sin 2\alpha$ and $\sin 2\beta$ involves discrete ambiguities, as does the measurement of η so that some additional information (*e.g.* on the size of V_{ub}) is necessary to single out a unique solution. The CKM analysis for $K \to \pi\nu\bar{\nu}$ is less complicated, which could turn out to be of advantage in the unitarity triangle determination.

Alternatively, results from the CP violation experiments in B physics and a $K_L^0 \to \pi^0\nu\bar{\nu}$ measurement could also be combined for high precision determinations of the CKM matrix. One could complete a CKM matrix determination that is essentially free of hadronic uncertainties[14]. The method could become particularly interesting when CP asymmetries in B decays are measured with improved precision at the LHC. Such a precise determination of the independent CKM parameters, in which $K_L^0 \to \pi^0\nu\bar{\nu}$ plays a crucial role, would provide an ideal basis for comparison with other observables sensitive to mixing angles, like $K^+ \to \pi^+\nu\bar{\nu}$, $B \to \pi l\nu$, x_s/x_d or V_{cb} from $b \to c$ transitions. Any additional, independent determination of CKM parameters would then constitute a test of the Standard Model. Any significant deviation would point to new physics.

Additional strategies for combining and comparing information from the rare K and the B sector are described in Refs.[3,15,16]. Finally, it should be emphasized that it is very desirable that such fundamental quantities as ϱ and η be measured redundantly via methods that do not share the same systematic errors.

Non-standard Models

Extensions of the Standard Model can in principle modify the physics discussed above in many ways. Usually extended models introduce a variety of new degrees of freedom and *a priori* unknown parameters, and it is therefore difficult to obtain definite predictions. However one can make a few general remarks relevant for $K_L^0 \to \pi^0 \nu\bar{\nu}$ and the comparison with information from the B system. For a review of CP violation in B physics beyond the SM see Refs.[17,18].

A clean SM test is provided by comparing η from $K_L^0 \to \pi^0 \nu\bar{\nu}$ with that triangulated from measurements of $|V_{ub}/V_{cb}|$ and x_d/x_s. Similarly, if B($K^+ \to \pi^+\nu\bar{\nu}$) is measured, a very clean test is to compare the value of $\sin 2\beta$ obtained from the two kaon decays with that determined from the CP-asymmetry in $B \to J/\psi K_S^0$[19]. Other incisive tests involve comparisons of the Jarlskog invariant obtained from $B(K_L^0 \to \pi^0 \nu\bar{\nu})$ with indirect determinations of the same quantity from the B system. Any discrepancy would clearly indicate new physics. The more theoretically precise the observables under discussion, the smaller the deviation that could be detected.

In some new physics scenarios, such as multi-Higgs doublet models[20,21] or minimal SUSY in which the CKM matrix remains the sole source of CP violation, the extraction of $\sin 2\alpha$ and $\sin 2\beta$ from CP asymmetries in B decays would be unaffected. Such effects might then show up in a comparison with $K_L^0 \to \pi^0 \nu\bar{\nu}$, where e.g. charged Higgs contributions modify the top quark dependent function $X(x_t)$ in (1).

In other new physics scenarios, such as supersymmetric flavor models[22], the effects in $K \to \pi\nu\bar{\nu}$ tend to be small, while there can be large effects in the B (and also the D) system. In these models the rare K decays are the only clean way to measure the true CKM parameters.

Examples for new physics scenarios that show drastic deviations from the Standard Model are provided by some of the extended Higgs models discussed in[21], in topcolor-assisted technicolor models[23], in left-right symmetric models[24], in models with extra quarks in vector-like representations[25], lepto-quark exchange[25], and in four-generation models[26].

In the past year, attention has been focussed on the contributions of flavor-changing Z-penguin diagrams in generic low-energy supersymmetric extensions of the Standard Model[22,27–30]. Such diagrams can interfere with the weak penguins of the Standard Model, and either raise or reduce the predicted $B(K_L^0 \to \pi^0 \nu\bar{\nu})$ by considerable factors. Although there is still some controversy about this mechanism, it appears that very large effects are possible, possibly even more than an order of magnitude.

The E787 result on $K^+ \to \pi^+\nu\bar{\nu}$ and recent confirmation of a large value for ϵ'/ϵ[31,32] have focussed much attention on rare K decays. Many of the Beyond the Standard Model

(BSM) effects mentioned above could lead to a considerable enhancement of $B(K^+ \rightarrow \pi^+\nu\bar{\nu})$ over the SM prediction. The same type of flavor-changing Z-penguin diagrams that can contribute to rare K decays can affect ϵ'/ϵ[29]. If ϵ'/ϵ is dominated by such new physics, $B(K_L^0 \rightarrow \pi^0\nu\bar{\nu})$ can be more than 20 times higher than the central Standard Model prediction[29,33]. It is also possible for such effects to suppress $B(K_L^0 \rightarrow \pi^0\nu\bar{\nu})$ significantly. We stress, however, that as opposed to the case of ϵ'/ϵ, deviations from the predicted value of $B(K_L^0 \rightarrow \pi^0\nu\bar{\nu})$ unambiguously indicate the presence of new physics. Figure 3 compares the possible range of outcomes of KOPIO with the predictions of both the Standard Model and the models described above. The numbers along the abscissa indicate:

1. Conventional Standard Model fit[8].
2. Conservative Standard Model fit[34].
3. Generic SUSY model with minimal particle content[30].
4. MSSM with no new sources of flavor- or CP-violation[15].
5. All CP-violation due to supersymmetric soft phases[35].
6. $SU(2)_L \times SU(2)_R$ Higgs[36].
7. Fourth generation[26].
8. Top-color assisted technicolor[23].
9. Multiscale walking technicolor[37]
10. Extra quarks in vector-like representations of the Standard Model gauge group[25].
11. Seesaw Left-Right model[24].

An indication of the power of KOPIO to probe new physics is that the experiment is sensitive to a factor of more than 500 below the Reference Grossman-Nir bound, of which only about 1% is allowed by the Standard Model. Figure 3 shows that this territory is stocked with many accessible candidates.

Theoretical summary

As a consequence of unprecedented theoretical precision and anticipated experimental accessibility, a measurement of $K_L^0 \rightarrow \pi^0\nu\bar{\nu}$ can unambiguously test the SM origin of CP violation, directly measure the area of the unitarity triangle, and ultimately yield the most accurate determination of the CKM CP violating phase η. This rare decay mode therefore provides a unique opportunity for making significant progress in our understanding of flavor-dynamics and CP violation. It is competitive with and complementary to future measurements in the B meson system. If new physics is manifesting itself in $K^+ \rightarrow \pi^+\nu\bar{\nu}$ and ϵ'/ϵ, it is virtually certain to show up in an unambiguous way in a measurement of $K_L^0 \rightarrow \pi^0\nu\bar{\nu}$. Absence of $K_L^0 \rightarrow \pi^0\nu\bar{\nu}$ within the range of about $(3 \pm 2) \times 10^{-11}$ or a conflict with other CKM determinations would certainly indicate new physics.

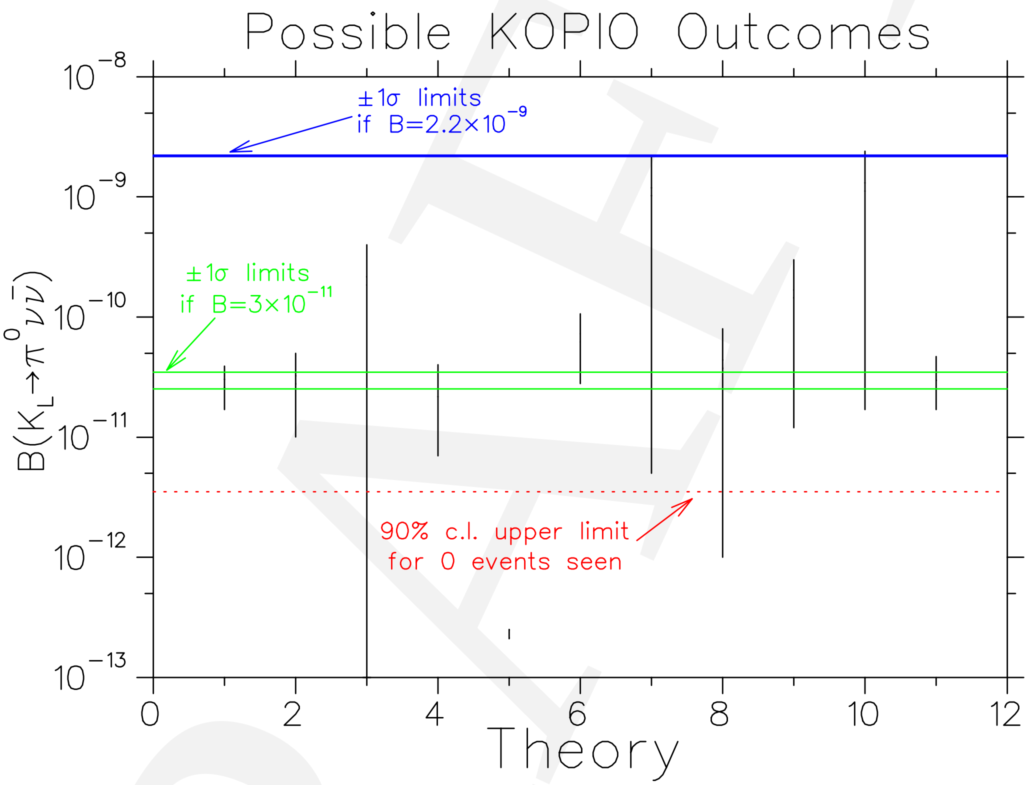

Fig. 3. Range of possible KOPIO outcomes compared with theoretical predictions for $K_L^0 \to \pi^0 \nu \bar{\nu}$. The lowest horizontal line (dotted) indicates the 90% confidence level upper limit that will be extracted if no events are seen above background. The two horizontal lines near the center are the 1σ limits that would be extracted if $B(K_L^0 \to \pi^0 \nu \bar{\nu})$ is measured to be near the center of the current Standard Model predicted range. The horizontal line near the top is actually two lines, which are the 1σ limits that would be extracted if the branching ratio were equal to the current Grossman-Nir bound. The vertical lines show the ranges of various theoretical predictions. These are described in the text.

2.2 Radiative decays

Introduction

The KOPIO apparatus is designed on the basis of the requirements for the decay $K_L^\circ \to \pi^0 \nu \overline{\nu}$. It has a list of remarkable properties, which can be summarized as follows:

- sensitivity corresponding to $\sim 10^{14}$ K_L° decays;
- hermetic veto coverage;
- measurement of energy and direction of photons and electrons;
- measurement of the K_L^0 momentum.

These characteristics make it an ideal tool for the measurement of rare K_L° decays with photons and electrons in the final state (for simplicity $radiative$ decays in the following) , exploiting, in many cases, overconstrained kinematics.

The study of these decays has received continued interest in the last decade[1]. On one hand, they can provide phenomenological information needed to interpret the measurement of other rare decays in terms of fundamental parameters of the SM. On the other hand they are a testing ground for theoretical approaches to the calculation of non perturbative effects of strong interactions in weak decays.

In this context chiral perturbation theory[2] (χPT) has grown to be one of the most fruitful tools. This low energy effective theory, in which the fundamental fields are those associated with the octet of pseudoscalar mesons, is based on a power series derivative expansion of a Lagrangian, the form of which is fixed by the ansatz of the chiral symmetry of the QCD Lagrangian in the limit of massless quarks. Within this framework, amplitudes for physical processes can be expressed as a perturbative expansion in terms of few free parameters. Relations among different processes can be established and precision measurements serve the dual purpose of verifying the assumptions on which the theory is based and fixing its parameters.

$\boldsymbol{K_L^\circ \to \gamma\gamma, K_L^\circ \to \gamma\gamma^*, K_L^\circ \to \gamma^*\gamma^*}$

Interest in these channels arises mainly in connection with the theoretical description of the decay $K_L^\circ \to \mu^+\mu^-$, whose branching ratio has been measured with ~ 6200 events by the E871 collaboration[3]

$$B.R.(K_L \to \mu^+\mu^-) = (7.18 \pm 0.17) \times 10^{-9}.$$

The short distance contribution to this decay proceeds through internal quark loops, dominated by the top quark. Thus it can provide information on the ρ parameter of the Wolfenstein parametrization of the CKM matrix. However the description of the decay includes the absorptive contribution, dominated by the $K_L^\circ \to \gamma\gamma$ contribution, and a long distance dispersive contribution dominated by virtual photon exchange. These contributions can be constrained by precision measurements of the branching ratio of the two photon decay, as well as by accurate information on the branching ratio and form factors for channels involving virtual photon exchange such as $K_L^\circ \to \gamma e^+e^-$, $K_L^\circ \to \gamma\mu^+\mu^-$, $K_L^\circ \to e^+e^-e^+e^-$, $K_L^\circ \to e^+e^-\mu^+\mu^-$, $K_L^\circ \to \mu^+\mu^-\mu^+\mu^-$.

A summary of the present knowledge on these decays is provided in the Table T2.2.

Decay	Exp.	kaon decays	Ev.	BKG	Measurement
$\gamma\gamma$	NA31[4]	4.7×10^8	110000	700	$BR = (5.92 \pm 0.15) \times 10^{-4}$
γe^+e^-	NA48[5]	4.1×10^9	6864	10	$BR = (1.06 \pm 0.05) \times 10^{-5}$ $\alpha_{K^*} = -0.36 \pm 0.06$
$\gamma\mu^+\mu^-$	KTEV[6]	3×10^{11}	9327	222	$BR = (3.66 \pm 0.08) \times 10^{-7}$ $\alpha_{K^*} = -0.157^{+0.025}_{-0.027}$
$e^+e^-e^+e^-$	NA48[7]	4.6×10^{10}	132	~ 0	$BR = (3.67 \pm 0.40) \times 10^{-8}$
	KTEV[8]	3×10^{11}	441	4	$BR = (3.72 \pm 0.29) \times 10^{-8}$
$e^+e^-\mu^+\mu^-$	KTEV[9]	3×10^{11}	38	?	$(2.50 \pm 0.44) \times 10^{-9}$

Although detailed calculations of acceptances and background separation have yet to be performed, a rough comparison of the number of kaon decays with the $\sim 10^{14}$ expected in KOPIO indicates the possibility of high statistics studies also for the rarest channels. Muon identification and measurement, for muons ranging in the calorimeter, will also be considered. This possibility, which relies on the low average density of the preradiator, the favourable sampling fraction of the calorimeter and the use of kinematic fits to improve resolution, will be studied in due course.

Valuable information will thus be provided by KOPIO on the following items:

a) precision measurements of the branching ratios; these will probably be limited by the knowledge of the branching ratios for the normalization channels (for which, however, an improved situation is expected after completion of the KLOE program);

b) study of the form factors for the decay γe^+e^-, with good sensitivity in the region of high e^+e^- effective mass. This will allow a more stringent comparison with different models[10][11] and clarify the discrepancy between the α_{K^*} parameter of the BMS[10] parametrization measured in γe^+e^- and in $\gamma\mu^+\mu^-$, which is more sensitive to the form factor;

c) measurement of the form factor for $K_L^\circ\gamma^*\gamma^*$, by a study of the decay to two lepton pairs, expecially in the high mass region; this study will be best performed in the $K_L^\circ \to e^+e^-\mu^+\mu^-$ channel since the decay $K_L^\circ \to e^+e^-e^+e^-$ would suffer from ambiguity in the charge assignment.

$K_L^\circ \to \pi^0\gamma\gamma$

The measurement of this decay provides information on a possible CP conserving contribution to the decay $K_L^\circ \to \pi^0 e^+ e^-$, a channel which could exhibit large effects of direct CP violation[12] (although its measurement could be hindered by an overwhelming physics background from the decay $K_L^\circ \to \gamma\gamma e^+ e^-$). The CP conserving contribution to $K_L^\circ \to \pi^0 e^+ e^-$, is associated to two-photon exchange and its estimate can be constrained by the measurement of $K_L^\circ \to \pi^0\gamma\gamma$.

In terms of the invariant variables

$$y = \frac{p_K \cdot (q_1 - q_2)}{m_K^2}\,;\, z = \frac{(q_1 + q_2)^2}{m_K^2} = \frac{m_{\gamma\gamma}^2}{m_K^2},$$

in the approximation of CP conservation, the double differential rate for unpolarized photons is given by an expression involving two amplitudes (A and B) corresponding to two different total angular momentum states for the 2 gammas (J=0 and J=2 respectively).

$$\frac{d^2\Gamma}{dydz} = \frac{m_K}{2^9\pi^3}\left\{ z^2|A+B|^2 + \left[y^2 - \frac{1}{4}\lambda\left(1, z, \frac{m_\pi^2}{m_K^2}\right)\right] |B|^2 \right\}$$

with

$$\lambda\left(x, y, z\right) = x^2 + y^2 + z^2 - 2\left(xy + xz + yz\right).$$

The existing experimental information[13] gives a B.R. $\sim 1 \times 10^{-7}$ and shows a z distribution concentrated at high values ($z > 0.3$), indicating a dominance of the A amplitude. This would lead to a small contribution of two-photon exchange to $\pi^0 e^+ e^-$, since, in the coupling to two electrons, the J=0 amplitude (A) is subject to helicity suppression. This conclusion is not without problems for the χPT description of this decay[14]. The calculation at $O(p^4)$ would indeed predict a vanishing B amplitude, but it underestimates the rate ($K_L^\circ \to \pi^\circ\gamma\gamma$) by a factor 3. This has led theorists to consider contributions that go beyond $O(p^4)$. These include vector meson contributions for which phenomenological models have been formulated. Experimental information on this rather complicated situation requires a study of the z distribution in the low z region, where present data are insufficient. In KOPIO this will require adequate suppression of the $2\pi^0$ background, which is important in this z region.

Other radiative decays

The decay $K_L^\circ \to \gamma\gamma\gamma$ is allowed, but suppressed by gauge invariance and boson statistics. Estimates for the B.R. are on the order of 10^{-19}[15]. Observation would indicate new physics. The best limit, from NA31[16] is B.R. $< 2.4 \times 10^{-7}$. Since this channel is very well constrained in KOPIO, it is reasonable to expect that the limit can be pushed to the 10^{-11} 10^{-12} range.

$K_L^\circ \rightarrow \pi^0\pi^0\gamma$ proceeds through $O(p^6)$ terms in χPT. There is a conflict in the prediction of the rate with Heiliger and Sehgal[17] predicting $\sim 1 \times 10^{-8}$ and Ecker, Neufeld and Pich[18], predicting $\sim 7 \times 10^{-11}$. KOPIO should be able to reach below the existing limit of NA31[19] ($B(K_L \rightarrow \pi^\circ\pi^\circ\gamma) < 5.6 \times 10^{-6}$).

3 Overview of the $K_L^0 \rightarrow \pi^0 \nu \bar{\nu}$ measurement technique

Along with the challenge of obtaining sufficient detection sensitivity, one of the main issues in measuring an ultra-rare process is the control of systematic uncertainties in estimating tiny levels of backgrounds. In general Monte Carlo calculations are of limited value in assessing minute problems or low level physics processes which can simulate the signal. The only reliable recourse is to use data to systematically study the backgrounds. This is feasible when there is enough experimental information for each event so that the signal can be securely grasped, the backgrounds confidently rejected, and the background levels independently measured in spite of limited statistics. Only with reliable background determinations at a level well below the experiment's sensitivity can observation of an extremely small signal be firmly established. The KOPIO experiment has been designed with this approach in mind.

The complete experimental signature for the $K_L^0 \rightarrow \pi^0 \nu \bar{\nu}$ decay mode consists of exactly two photons with the invariant mass of a π^0, and nothing else. The experimental challenge arises from the 34% probability that a K_L^0 will emit at least one π^0 in comparison with the expected decay probability for $K_L^0 \rightarrow \pi^0 \nu \bar{\nu}$ which is ten orders of magnitude smaller. Compounding the difficulty, interactions between neutrons and kaons in the neutral beam with residual gas in the decay volume can also result in emission of single π^0s, as can the decays of hyperons which might occur in the decay region, *e.g.* $\Lambda \rightarrow \pi^0$n. The current experimental limit B($K_L^0 \rightarrow \pi^0 \nu \bar{\nu}$) $<$ 5.9 $\times 10^{-7}$[1] comes from a Fermilab experiment which employed the Dalitz decay $\pi^0 \rightarrow \gamma e^+ e^-$. Further improvement in sensitivity by perhaps an order of magnitude may be expected during the next few years. Thus, an experimental improvement in sensitivity of more than four orders of magnitude is required to obtain the signal for $K_L^0 \rightarrow \pi^0 \nu \bar{\nu}$ at the SM level of B($K_L^0 \rightarrow \pi^0 \nu \bar{\nu}$) = 3 $\times$ 10^{-11}.

For any experiment seeking to measure $K_L^0 \rightarrow \pi^0 \nu \bar{\nu}$ the most important means of eliminating unwanted events is to determine that nothing other than one π^0 was emitted in the decay, *i.e.* to veto any extra particles. The most difficult mode to suppress in this manner is $K_L^0 \rightarrow \pi^0 \pi^0$ ($K_{\pi 2}$). If this were the only defense against unwanted events, however, an extremely high (perhaps unachievable) photon veto detection efficiency would be required. Thus, to increase the probability that the source of an observed signal is truly $K_L^0 \rightarrow \pi^0 \nu \bar{\nu}$, another handle is needed.

That handle is provided by measurement of the K_L^0 momentum via time-of-flight (TOF). Copious low energy kaons can be produced at the AGS in an appropriately time structured beam. From knowledge of the decaying K_L^0 momentum the π^0 can be transformed to the K_L^0 center-of-mass frame and kinematic constraints can be imposed on an event-by-event basis. This technique facilitates rejection of bogus kaon decays and suppression of all other potential backgrounds, including otherwise extremely problematic ones such as hyperon decays and beam neutron and photon interactions.

The background suppression is achieved using a combination of hermetic high sensitivity photon vetoing and full reconstruction of each observed photon through measurements of position, angle and energy. Events originating in the two-body decay $K_L^0 \rightarrow \pi^0 \pi^0$ identify themselves when reconstructed in the K_L^0 center-of-mass system. Furthermore, those events with missing low energy photons, the most difficult to detect, can be identified and eliminated. With the two independent criteria based on precise kinematic measurements and demonstrated photon veto levels, not only is there enough experimental information so that $K_L^0 \rightarrow \pi^0\pi^0$ can be suppressed to the level well below the expected signal, but the background level can also be measured directly from data.

The beam and detectors for KOPIO employ well known technologies. Important aspects of the system are based on previously established measurement techniques and new aspects have been studied in beam measurements and with prototypes and simulations. Figure 4 shows a simplified representation of the beam and detector concept and Fig. 5 gives a schematic layout of the entire apparatus. The 25.5 GeV primary proton beam is presented to the kaon production target in 200 ps wide pulses at a rate of 25 MHz giving a microbunch separation of 40 ns. A 500 μsr solid angle neutral beam is extracted at 45° to produce a "soft" K_L spectrum peaked at 0.65 GeV/c; kaons in the range from about 0.4 GeV/c to 1.3 GeV/c are used. The vertical acceptance of the beam (5 mrad) is kept much smaller than the horizontal acceptance (100 mrad) so that effective collimation can be obtained to severely limit beam halos and to obtain another constraint on the decay vertex position. Downstream of the final beam collimator is a 4 m long decay region which is surrounded by the main detector. Approximately 16% of the kaons decay yielding a decay rate of about 10 MHz. The beam region is evacuated to a level of 10^{-7} Torr to suppress neutron-induced π^0 production. The decay region is surrounded by a thin walled vacuum tank which encloses a triple layer of plastic scintillators. Outside the vacuum is an efficient Pb/scintillator photon veto detector ("barrel veto"). In order to simplify triggering and offline analysis, only events with the signature of a single kaon decay producing two photons occurring within the period between microbunches are accepted.

Photons from $K_L^0 \rightarrow \pi^0\nu\bar{\nu}$ decay are observed in a two-stage "pointing calorimeter". It is comprised of a 2 radiation length (X_0) fine-grained preradiator calorimeter followed by a 16 X_0 electromagnetic calorimeter. The preradiator section obtains the energies, times, positions and angles of the interacting photons from π^0 decay by determining the initial trajectories of the first e^+e^- pairs. It consists of 64 0.034 X_0-thick layers each composed primarily of a plastic scintillator and a dual coordinate drift chamber. The preradiator measures the photon positions and directions accurately in order to allow reconstruction of the K_L decay vertex. In addition, since it is nearly fully active, the preradiator contributes principally to the achievement of excellent energy resolution.

The calorimeter located behind the preradiator consists of "Shashlyk" tower modules, roughly 11 cm by 11 cm in cross section. A Shashlyk calorimeter module consists of a stack of square tiles with alternating layers of Pb and plastic scintillator read out by penetrating Wavelength Shifting (WLS) fibers. The preradiator-calorimeter combination is expected to have an energy resolution of $\sigma_E/E \simeq 2.7\%/\sqrt{E}[GeV]$. Shashlyk is a proven technique which has been used effectively in BNL experiment E865 and is presently the main element in the PHENIX calorimeter at RHIC.

Suppression of most backgrounds is provided by a hermetic high efficiency charged particle and photon detector system surrounding the decay volume. The system includes scintillators inside the vacuum chamber, decay volume photon veto detectors and detectors down-

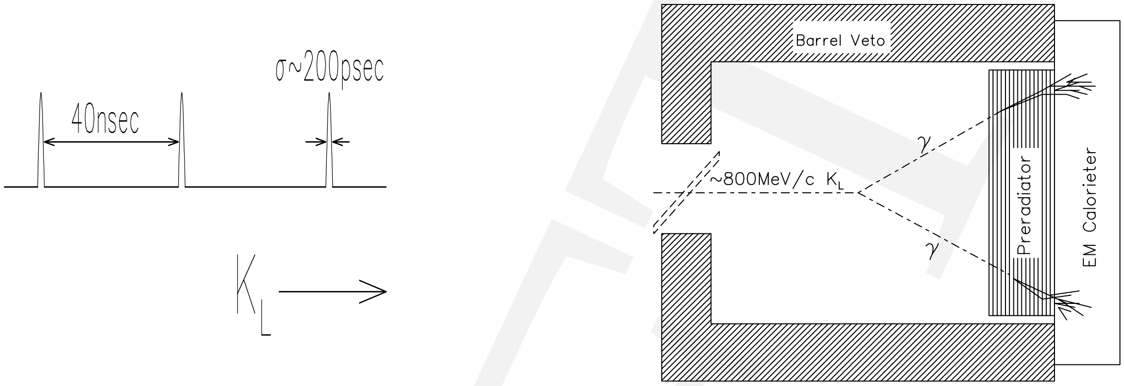

Fig. 4. Elements of the KOPIO concept : a pulsed primary beam produces low energy kaons whose time-of-flight reveals their momentum when the π^0 from $K_L^0 \to \pi^0\nu\bar{\nu}$ decay is reconstructed.

stream of the main decay volume. The barrel veto detectors are constructed as Pb/scintillator sandwiches providing about 18 X_0 for photon conversion and detection. The detection efficiency for photons has been extensively studied with a similar system in BNL experiment E787. The downstream section of the veto system is needed to reject events where photons or charged particles leave the decay volume through the beam hole. It consists of a sweeping magnet with a horizontal field, scintillators to detect charged particles deflected out of the beam, and photon veto modules. A special group of counters - collectively, the "catcher" - veto photons that leave the decay volume but remain in the beam phase space. This system takes advantage of the low energy nature of our environment to provide the requisite veto efficiency while being blind to the vast majority of neutrons and K_L^0s in the beam. The catcher uses Čerenkov radiators read out with phototubes.

The KOPIO system described above will clearly identify the $K_L^0 \to \pi^0\nu\bar{\nu}$ decay signal and effectively reject all backgrounds using a combination of kinematic measurements and photon vetos. Fig. 6 illustrates KOPIO's extensive arsenal of weapons including the measured quantities and constraints available. Reference values for the resolutions in the measured quantities are given in Table 1.

To illustrate how KOPIO will function to reject backgrounds, we consider bogus events originating with $K_{\pi 2}$ decays. The two types of $K_{\pi 2}$ background are the "even pairing" cases when the two observed photons come from one π^0 and the odd pairing cases when each photon originates from a different π^0. The odd pairing events will generally not reconstruct to the π^0 mass and are also suppressed by kinematic constraints as will be discussed below. Fig. 7 shows the π^0 energy distribution to be detected in the K_L center of mass frame ($E^*_{\pi^0}$) for the $K_L \to \pi^0\nu\bar{\nu}$ and $K_L \to \pi^0\pi^0$ ($K_{\pi 2}$) decays and Fig. 8 gives the 2-gamma mass spectrum $M_{\gamma\gamma}$ for the signal ($M_{\gamma\gamma} = M_\pi$) and for the odd-pairing gammas.

By tagging the K_L momentum as well as determining the energy and direction of γs, one can fully reconstruct the kinematics in 2-body decays. In the case where one π^0 is missing from a $K_{\pi 2}$ decay ("even pairing"), a kinematic cut on the monochromatic center of mass energy $E^*_{\pi^0}$ is effective, as shown in Fig. 7. In the case where one photon from each π^0

Table 1. Parameters and nominal resolutions (σ's) for photon energy (E), angles (θ_{xz},θ_{yz}), conversion positions (x, y), and timing (t) anticipated for KOPIO. In simulations, each measured quantity is smeared by adding a quantity $G\sigma$ where G is a random value chosen from a normal distribution with zero mean and unit variance, and σ is given in the table.

Quantity	Nominal value	σ used in smearing
E	C_E (0.027 GeV$^{1/2}$)	$C_E/\sqrt{E}$
θ_{xz}	$\sigma_{\theta xz}$ (8.2mrad·GeV$^{0.7}$)	$\sigma_{\theta xz} \cdot E^{-0.7}$(96%) $3.6 \cdot \sigma_{\theta xz} \cdot E^{-0.7}$(4%)
θ_{yz}	$\sigma_{\theta yz}$ (8.2mrad·GeV$^{0.7}$)	$\sigma_{\theta yz} \cdot E^{-0.7}$(96%) $3.6 \cdot \sigma_{\theta yz} \cdot E^{-0.7}$(4%)
x	C_x (0.45 cm-GeV$^{1/2}$)	$C_x/\sqrt{E}$
y	C_y (0.45 cm-GeV$^{1/2}$)	$C_y/\sqrt{E}$
t	σ_t (0.2 ns)	σ_t

is missed ("odd pairing"), a π^0 mass requirement ($m_{\gamma\gamma}$) is effective as shown in Fig. 8. Additional photon energy cuts on $E^*_{\pi^0}$ vs. $|E^*_{\gamma 1} - E^*_{\gamma 2}|$, where $E^*_{\gamma 1}$ and $E^*_{\gamma 2}$ are the energies of γs in the K_L center of mass system, are especially effective in further suppressing the $K_{\pi 2}$ background. This is illustrated in Fig. 9 which shows distributions of $E^*_{\pi^0}$ vs. $|E^*_{\gamma 1} - E^*_{\gamma 2}|$ (using the energy resolution indicated in Table 1 and after the π^0 mass requirement was imposed) for the $K_L \rightarrow \pi^0\pi^0$ (left plot) and for the $K^0_L \rightarrow \pi^0\nu\bar{\nu}$ signal (right plot). The band in the left hand figure at $E^*_{\pi^0}$ =249 MeV corresponds to the even pairing background, which is suppressed by a $E^*_{\pi^0}$ cut at 225 MeV/c as discussed above. The remaining band corresponds to the odd pairing background, which is confined to a region constrained by the π^0 mass. The solid lines show the signal regions in both plots for nominal cuts The signal region in Fig. 9 appears low in $E^*_{\pi^0}$. This is because the photon veto, which is not applied to the events shown in this figure, is especially effective at eliminating those odd-pairing events which appear in the signal box. Further background suppression can be had at the cost of modest acceptance loss providing a certain margin of safety. When reasonable photon veto efficiency values based on E787 measurements are also assumed, the added capability of full kinematic reconstruction leads to the $K_{\pi 2}$ background being suppressed to a level well below the anticipated signal. A more complete discussion of the potential backgrounds is given below.

Evaluation of the KOPIO system leads to the expectation that a signal of about 40 $K^0_L \rightarrow \pi^0\nu\bar{\nu}$ events will be collected if the SM prediction holds. In the following sections, we provide details on the KOPIO beam, detection apparatus, sensitivity and backgrounds.

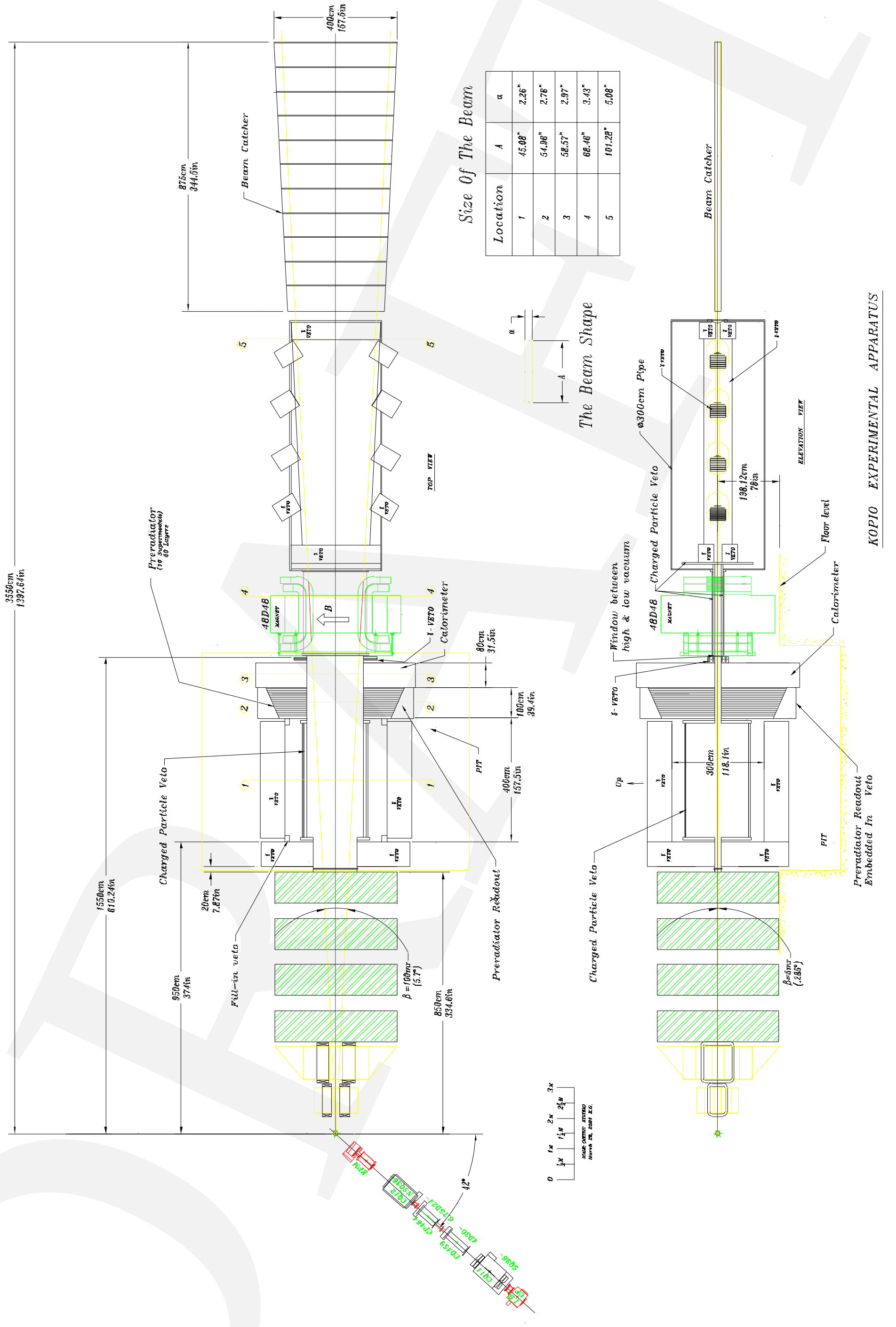

Fig. 5. Plan and elevation views of KOPIO detector.

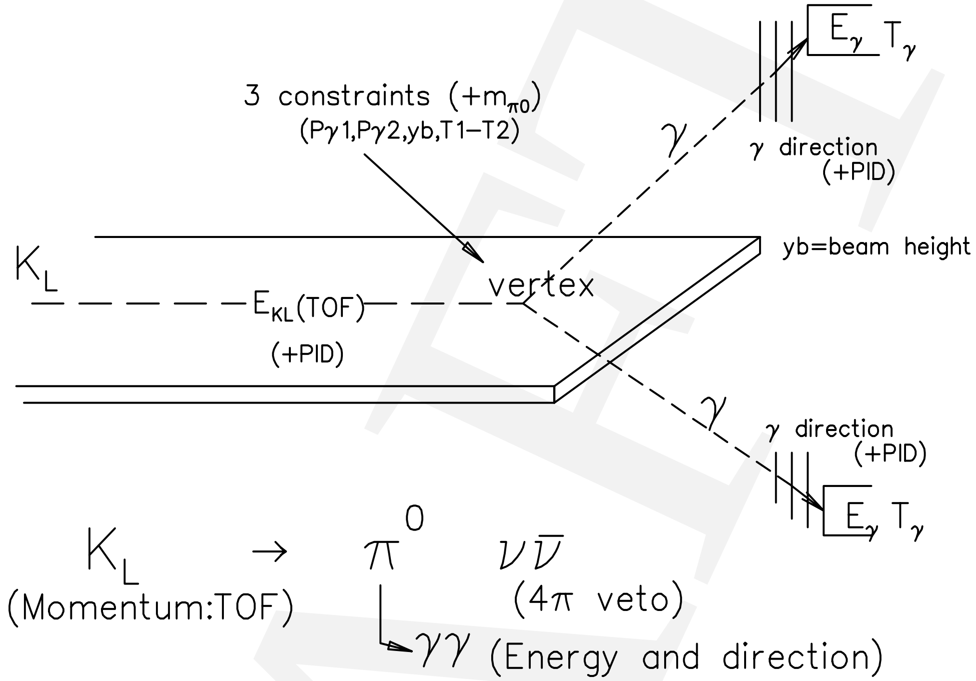

Fig. 6. An illustration of quantities measured and constraints available in the KOPIO experiment. Measurements include the K_L energy, and the gamma energies, directions and times. Particle identification (PID) is also available. Constraints include the π^0 mass (M_π^0), the beam vertical extent (y_b) and relative timing of the photons.

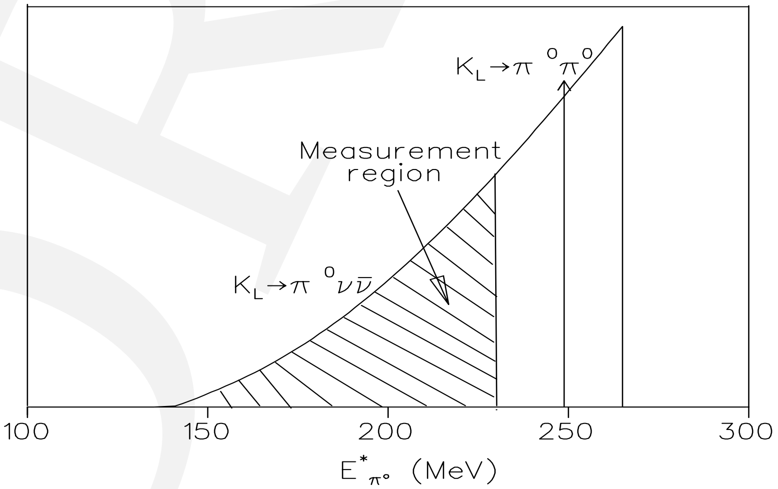

Fig. 7. Energy spectrum of π^0 in the K_L center of mass frame (left).

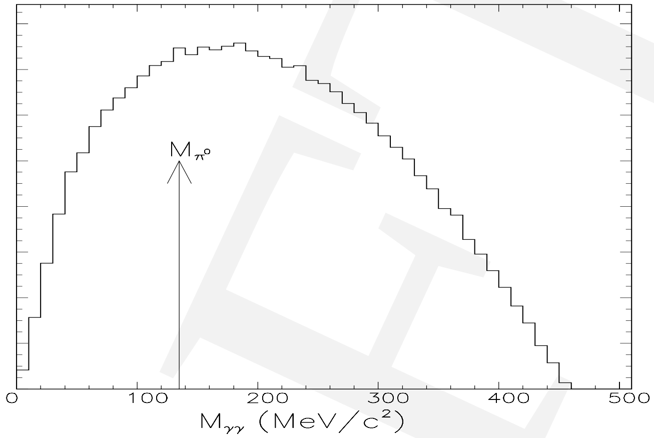

Fig. 8. The 2-gamma mass spectrum ($M_{\gamma\gamma}$) for “odd-pairing” gammas in $K_{\pi 2}$ decays.

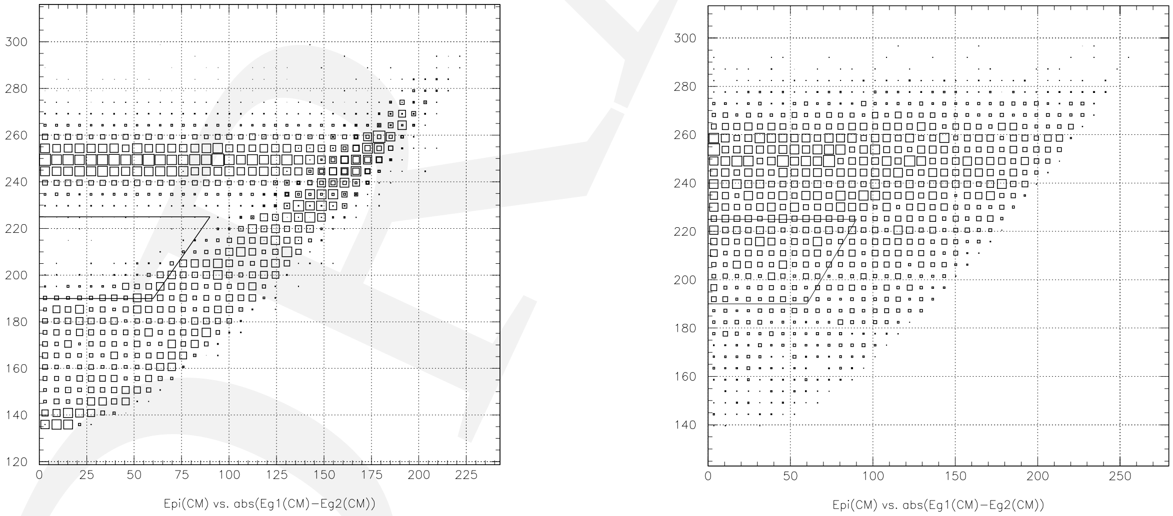

Fig. 9. Distributions of $E^*_{\pi^0}$ vs. $|E^*_{\gamma 1} - E^*_{\gamma 2}|$ after π^0 mass requirement for the $K_L \to \pi^0\pi^0$ (left) and for the signal (right). The solid line encloses the signal region.

4 Beams

4.1 AGS

The AGS intensity has increased more than a thousand-fold over its initial design value so that it is presently the most intense source of multi-GeV protons in the world. Figure 10 displays the peak intensity per cycle in each year of AGS operation. A flux of 0.73×10^{14} protons per AGS cycle has been accelerated in the AGS with six booster cycles per AGS cycle. A further upgrade to 10^{14} protons (100 TP) per AGS cycle could be accomplished by raising the extraction energy from the booster for transfer to the AGS from 1.7 GeV to 2 GeV which would improve the space charge limits by a factor of 1.4 for injection into the AGS.

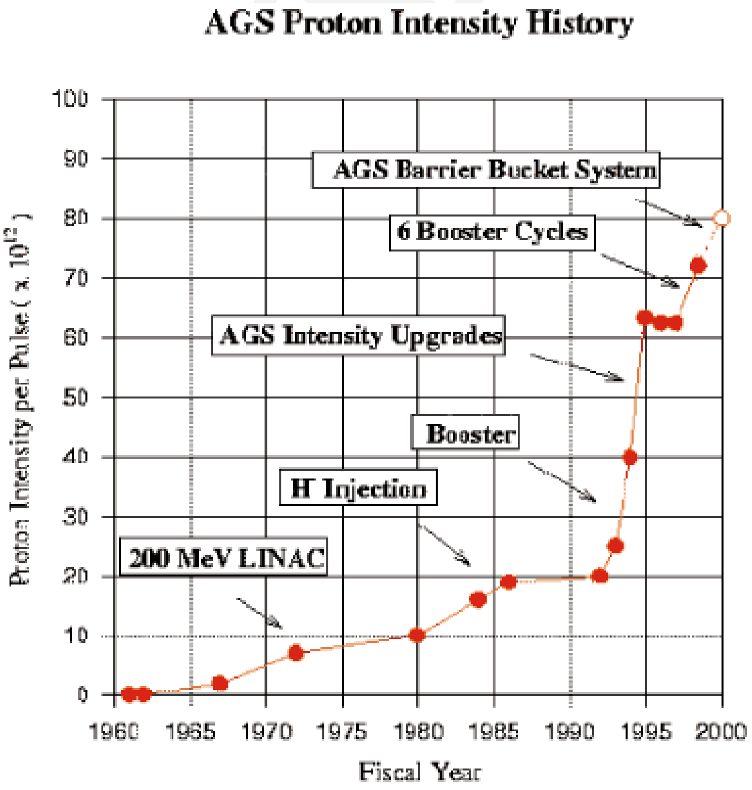

Fig. 10. AGS Proton Intensity History. The peak proton intensity accelerated in each year.

RF Development for micro-bunched Beam.

Measurements of bunch lengths.

Micro-bunching the proton beam extracted from the AGS to produce micro-bunched neutral kaons at the production target allows determination of the K_L^0 momentum by time-of-flight and is therefore a key element in the kinematic separation of signal from background.

Micro-bunching is achieved by slowly extracting a coasting, debunched proton beam with finite momentum spread in the AGS by ramping the magnetic field through a betatron resonance with an rf field on but asynchronous with the proton beam except for the fraction at the maximum momentum prior to extraction. As the magnetic field is slowly decreased, the resonant fraction of the beam briefly becomes synchronous with the rf frequency and is forced between the empty rf buckets as it is extracted.[1]

A frequency of 25 MHz was chosen to balance the requirements of bunch spacing sufficient to prevent wrap around, i.e. the fastest particles in the neutral beam produced by a primary proton bunch overtaking the slowest ones of the preceding bunch, with the higher voltage required to compress the bunches at lower frequency. Since the bunch length is inversely proportional to the frequency and to the inverse of the square root of the rf voltage, reducing wrap around by lowering the frequency requires a disproportionate increase in gap voltage to compensate for the increase in micro-bunch width. A figure of merit for micro-bunching is the ratio of the period between bunches to the rms bunch width. This is defined as the Bunching Factor, Bf=$1/f\Delta t$ where f is the bunching frequency. The results of model scaling calculations for Bf as a function of rf voltage for different rates of AGS magnetic field variation during extraction of the micro-bunched beam are presented in Fig. 11.

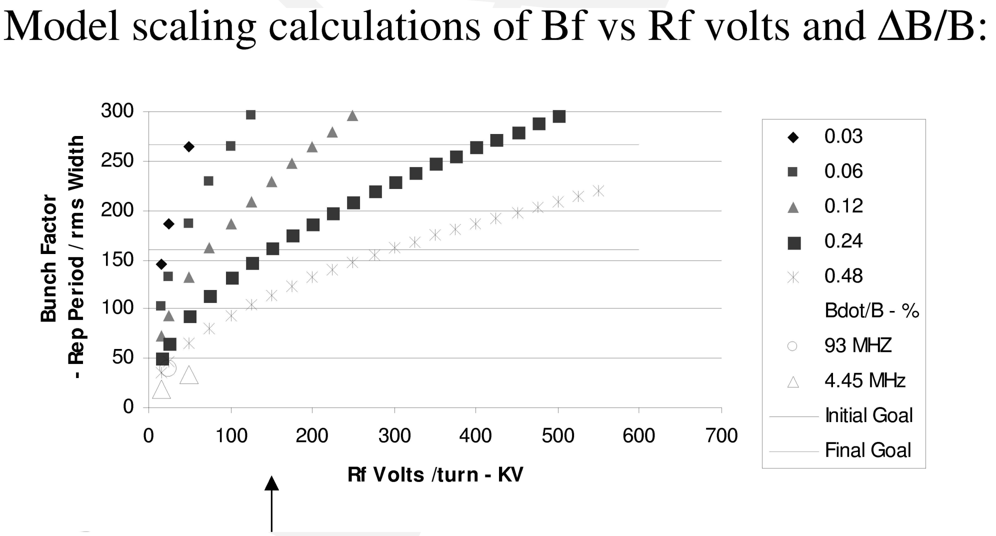

Fig. 11. Calculated dependence of bunching factor on rf voltage for various rates of magnetic field variation during extraction.

The rf optimization of a 25 MHz 150 KV cavity reference design for primary proton beam micro-bunching to produce less than 500 ps rms bunch width is being carried out at TRIUMF. This work includes the cavity and power amplifier/ driver design specifications. R & D is required for the possible addition of an harmonic cavity at 100 MHz which has the potential to further reduce the bunch width to less than 200 ps. This will involve a cooperative effort between BNL and TRIUMF.

Previous measurements at the AGS have been made with the 93 MHz dilution cavity

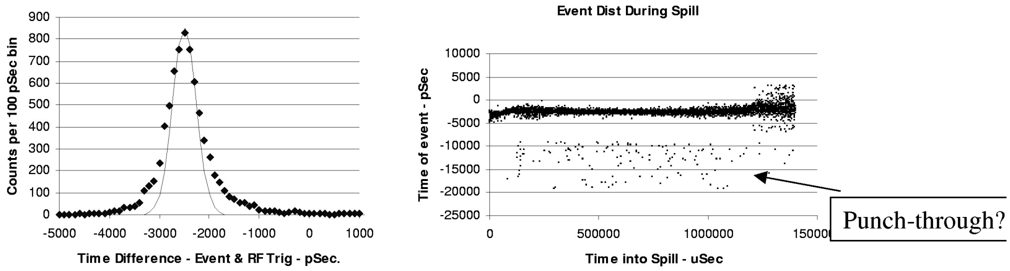

Bunches down to 250 pSec rms have been measured at 93 MHz with Gold beam

Fig. 12. Left:Bunch width produced at 93 MHz with 11 GeV/N Au ions incident on a 75μ quartz Čerenkov radiator. Right:Time distribution of micro-bunched and punch through Au ions during a spill.

which produced a significant micro-bunch width variation within a single AGS cycle as measured with an 11 GeV/N Au beam incident on a 75μm quartz Čerenkov radiator. Some of these data are displayed in Fig. 12. Micro-bunch widths of 270 and 160 ps rms were observed within the illustrated spill. Further studies are needed to understand this variation and its dependence on machine parameters.

The best measurement obtained for a micro-bunched proton beam was 280 ps rms which was obtained with the 93 MHz cavity with ≈ 25 KV across the gap.

Measurements of bunch width and extraction efficiency dependence on rf voltage.

The main 4.4 MHz AGS cavities were operated at higher than usual voltage to more tightly bunch the beam. As expected the bunch width decreased with increased voltage and the extraction efficiency did not decline with higher voltage. Plans are being made for further bunching measurements at 2.2 and 4.4 MHz to confirm that a two frequency system works and at 4.4 MHz to better measure bunch shrinkage with increased voltage during C Line operation in the summer of 2001.

Current plans call for the detection of prompt γ's from π^0 decay at a production target surface viewed through a collimated port at 90$^{\rm o}$ to the primary proton beam direction. Installation of a sweeping magnet to remove charged particle background will likely be required although a charged particle veto counter is planned to precede the converter in front of the electron detectors. Currently, the latter are planned to be a scintillator followed by a shower counter whose signal thresholds will be set to reject charged particle punch-through and interacting neutrons.

Four dimensional modeling of bunch width.

Early micro-bunching calculations were based on independent transverse and longitudinal models. More recent efforts have combined these models into a four dimensional phase space of transverse position and angle with rf phase ϕ and its time derivative $\dot{\phi}$. Four dimensional modeling of the bunching quality is continuing at TRIUMF and BNL.

Beam present between bunches.

Analysis of data obtained during the previous rf bunching measurements indicates the residual beam present between rf bunches at 4.4 MHz was at the level of $< 10^{-2}$ of the intensity in the bunch.

Primary Beam Modifications.

The primary proton beam required by KOPIO is resonantly extracted from the AGS at 25.5 GeV/c over 2.4 seconds with a micro-bunch structure of less than 200 ps rms. It is anticipated that the full AGS intensity of $(0.7 - 1.0) \times 10^{14}$ protons per AGS acceleration cycle of 4.7 seconds will be available.

Measurements indicate the emittances of the 25.5 GeV/c slowly extracted primary proton beam are $\epsilon_H = 26.4\pi \pm 5.0$ mm-mr and $\epsilon_V = 54.7\pi \pm 5.0$mm-mr in the horizontal and vertical planes, respectively.[2] These emittances as well as the relevant Twiss parameters at the extraction point have been used in the simulation of the proposed C3 Beam Line modification.

Figure 13 gives the proposed extracted proton beam magnet configuration in the downstream section of the C Line and the KOPIO experimental area configuration. The primary proton beam in the C line would be made parallel through the C target region by the present CQ11 and CQ12 and brought to a final focus at C′.

Magnet reconfiguration

Modification of the primary proton beam consists of bringing the present beam through the C Target Station area approximately parallel in both planes and producing a new final focus 50 meters downstream. A new quadrupole doublet using 5Q36 magnets is planned for the final focus at new target (C′) for the KOPIO neutral beam. Vertical and horizontal trim magnets will center the focussed beam on the KOPIO production target at C′. Calculated horizontal and vertical beam envelopes from AGS extraction to the final focus are displayed in Fig. 14.

Results of simulation of the vertical phase space distribution at the KOPIO beam production target is given in Fig. 15. This simulation includes multiple Coulomb scattering contributions due to vacuum windows and air gaps in the beam line. The horizontal phase space has a 7 mm spot with small angular divergence. Since the target is viewed at 45° with a large horizontal acceptance by the neutral beam, this is relevant only because of a small additional absorption of neutral kaons in the target. Although the vertical image is ≈ 1 mm FWHM at the target center, the 40 mr of vertical divergence at the ends of a one interaction length long platinum target will contribute additional spread to the wings of the vertical distribution. A 2 mm high vertical source of the neutral beam would contribute little to the error in the determination of the K_L^0 trajectory which would be dominated by the angular resolution of the preradiator. However the small vertical aperture of the neutral beam collimator array requires a small vertical neutral beam source in order to minimize the illumination of the aperture surfaces by the beam.

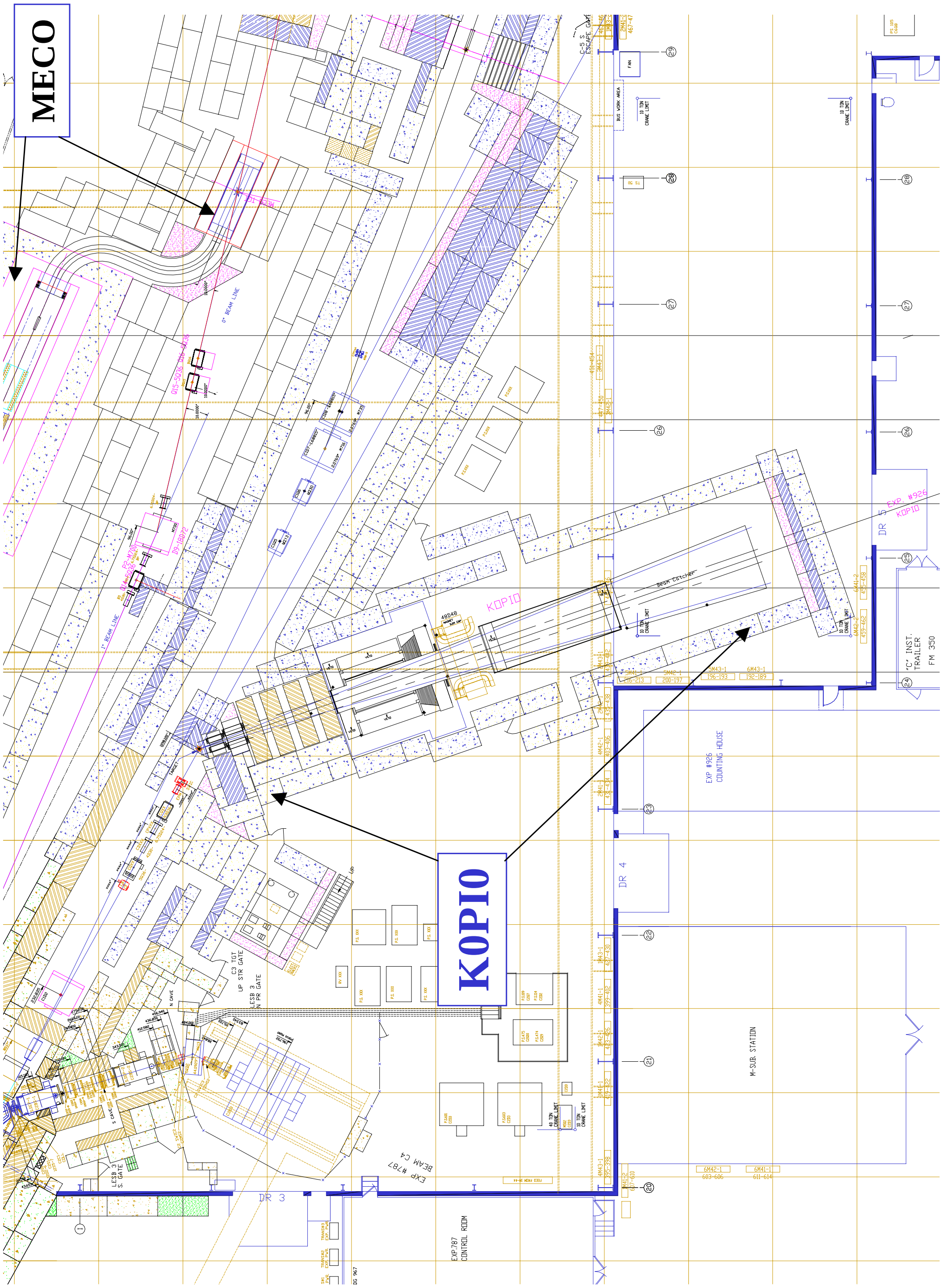

Fig. 13. Plan view of KOPIO. The grid spacing is 200 inches.

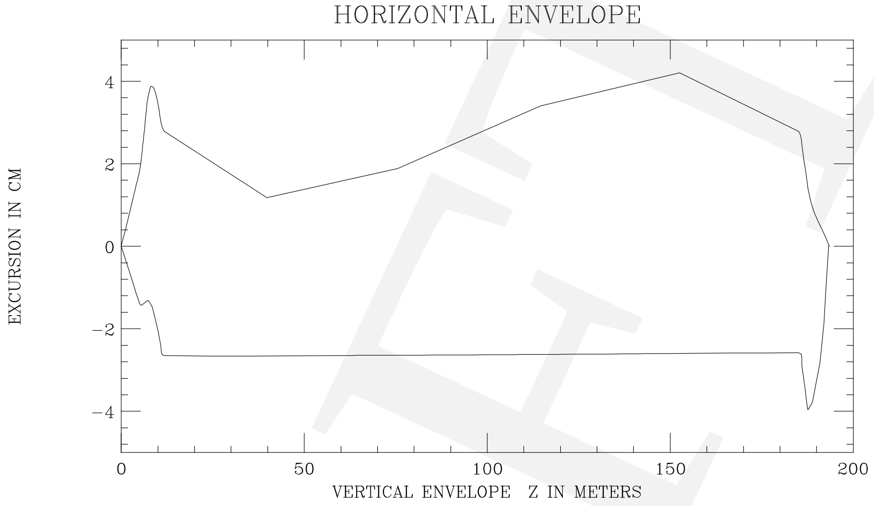

Fig. 14. Horizontal (upper) and vertical (lower) primary proton beam envelopes

Proton Vertical Phase Space at the Production Target

20-														
							3	4	3					
					1	7	6	5	7	6	1			
				1	2	9	13	11	12	15	7			
			3	7	17	11	18	16	6	10	8	14	7	
		4	10	11	15	17	8	20	17	9	17	16	4	
	2	13	8	15	13	14	9	14	23	18	9	10	7	
	3	11	12	15	13	18	14	17	17	19	18	22	9	
Y’	2	11	13	18	17	17	24	16	13	15	13	13	8	
mr	2	20	13	18	19	21	20	16	17	17	16	14	17	
		19	12	18	16	14	16	22	17	20	18	11	16	1
		13	19	11	16	11	20	12	18	16	19	13	15	4
		4	15	14	21	13	22	24	15	17	9	18	13	3
		11	14	13	17	22	20	21	9	16	20	17	9	1
			14	7	10	13	12	16	12	18	13	5	6	
		2	16	9	14	10	13	14	19	15	3	3		
			2	4	7	13	11	10	5	1				
-20-						1	5	5	1	2				

-.5 Y mm .5

Fig. 15. Simulation of the Y vs. θ_Y distribution of the primary proton beam at the center of the production target.

Construction will include removal of much of the C line proton transport downstream of the C Target (E949). The new transport will simplify the area bringing a parallel beam through the C Target area with E949 off and a final focus at the new C′ Target produced by a quadrupole doublet similar to the present one at the C Target Area. In addition to the magnet rearrangement, it will be necessary to clear the magnet power supply area where KOPIO will be located. Although most of the power supplies will no longer be needed, six will have to be relocated since they are required for the primary beam transport.

Primary beam and collimator.

A proton beam plug will be installed immediately downstream of E949 in order to minimize activation of components in the area in which the proton beam modifications have taken place and where KOPIO neutral beam construction is to occur. A hole in the plug would allow some beam to reach the KOPIO target for testing purposes. The installation of the primary beam plug/collimator will therefore be on remotely controlled jacks.

Shielding reconfiguration and power supply removal.

The shielding arrangement on the east side of the C Line must be reconfigured to allow for the neutral beam penetration and the substantially increased intensity that will be transported to the C′ Target. Significant addition to the proton beam stop will also be required. An engineering run to determine the validity of the simulations that led to the collimator and sweeping magnet designs to minimize beam halo is planned for early in FY04.

Primary beam instrumentation.

The beam monitoring instrumentation for the new C′ Target Station will include the usual secondary emission monitor (SEM) for beam intensity measurement, a fluorescent flag and two dimensional segmented wire ionization chamber (SWIC) for beam profile monitoring and to servo the beam position on the target in order to compensate for the beam momentum variation during extraction from the AGS.

Additional instrumentation will be required for evaluation of the beam bunching quality. The bunch width will be measured during beam studies starting in the summer of 2001 by observing the time distribution of prompt γ's from the decay of π^0's at the production target surface which reach a small calorimeter located behind a collimated port in the shield wall at 90^o to the primary proton beam direction. A charged particle veto consisting of a thin scintillation counter in front of the calorimeter should reduce the incident charged particle background to a manageable level despite their two to three times greater numbers because of their continuous momentum spectrum which is reflected in their time distribution. This can be carried out at several target stations but is most likely to occur at the C Target.

During KOPIO running, an on-line monitor of bunching quality which includes measuring the proton flux between bunches as well as the bunch width would be required. The C′ target would be viewed through a port at a large production angle, i.e. greater than 90^o, containing precise collimation. This would be followed by a charged particle sweeping magnet, a drift space preceding the charged particle veto counters, and a compact CsI or $PbWO_3$ calorimeter.

The large production angle and small angular acceptance of the calorimeter will be chosen to provide acceptable counting rates in the monitor.

Production target and target station design.

The water cooled target under consideration is 10.6 cm in length, 8 mm in width and 2 mm in height. Both BNL and TRIUMF have experience with high intensity targets. The production target may be similar to the present water cooled C target but since it will be subjected to 2-3 times the instantaneous rate this design may be inadequate. The temperature rise is being modeled using the same codes that were used in the design of the C Target. Other target design options such as water cooled rotating disks and cooling water enclosed targets are being considered. Target cooling and personnel shielding from the target must be designed so that they do not contribute to background, in particular, neutron halo.

Booster F3 and AGS A5 kicker magnet pulse forming networks.

Transfer of 2 GeV protons from the booster to the AGS will require modification of the power supplies for two kicker magnets, F3 in the booster and A5 in the AGS. Their locations are indicated in Fig. 16. Presently, it is estimated that losses during injection into the AGS are as high as 30%. The Booster was designed to operate at 2 GeV/c in order to reduce space charge limitations on injected AGS intensity. The A5 kicker magnet and power supply are inadequate to cleanly deflect 2 GeV/c beam bunches from the booster past the injection septum onto a central orbit in the AGS. Consequently, coherent oscillations are induced leading to beam loss. A new full aperture A5 kicker magnet has been designed for the AGS intensity upgrade[*]. A new pulse forming network (PFN) or a power supply redesign using modulators will be required as well. Optimization of this work will require engineering studies to determine the most effective improvements.

The new PFN would be located outside the AGS tunnel thereby removing it from a high radiation environment while providing greater ease of maintenance. The new PFN will also reduce the decay time of the kicker pulse which has interfered with six bunch transfer from the Booster to the AGS.

The present F3 kicker magnet for Booster extraction is adequate but capacitors must be added to the PFN. Completion of this upgrade is expected to result in the acceleration of more than 100 TP per AGS cycle.

Neutral Beam

Neutral flux and spectra

For 25.5 GeV/c primary protons, the continuous K_L^0 momentum spectrum at 45^o peaks in the vicinity of 650 MeV/c as indicated in the spectrum at the entrance to the KOPIO decay volume presented in Fig. 17. This spectrum was calculated from previous fits to production data for charged kaons with corrections for absorption in the target and decay of K_L^0's in the upstream section of the beam. A single AGS cycle is anticipated to yield $\approx 10^8$ K_L^0.

---

[*] Construction of a new A5 kicker will be postponed to a later stage of KOPIO.

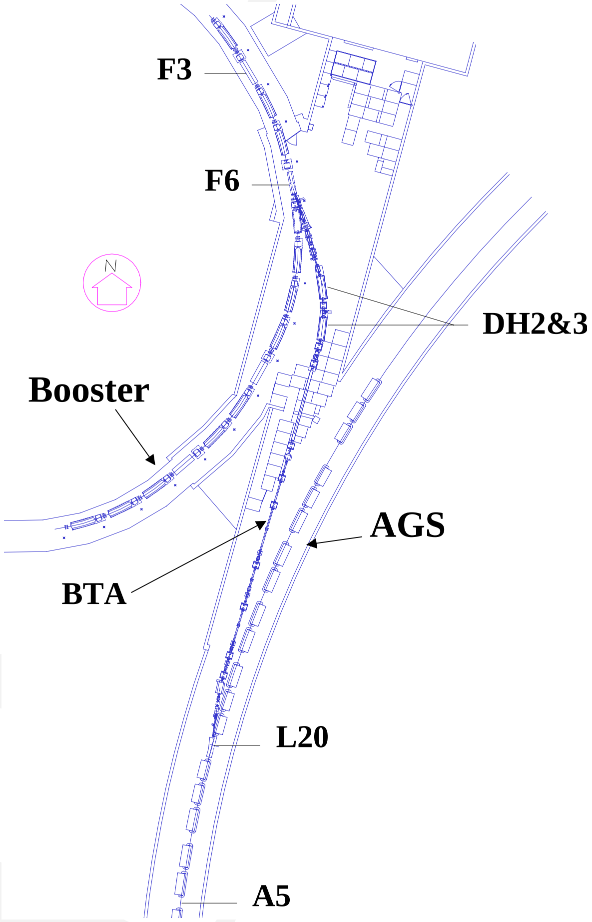

Fig. 16. Booster to AGS transfer line. The locations of the kicker magnets for Booster extraction and AGS injection are at F3 and A5, respectively.

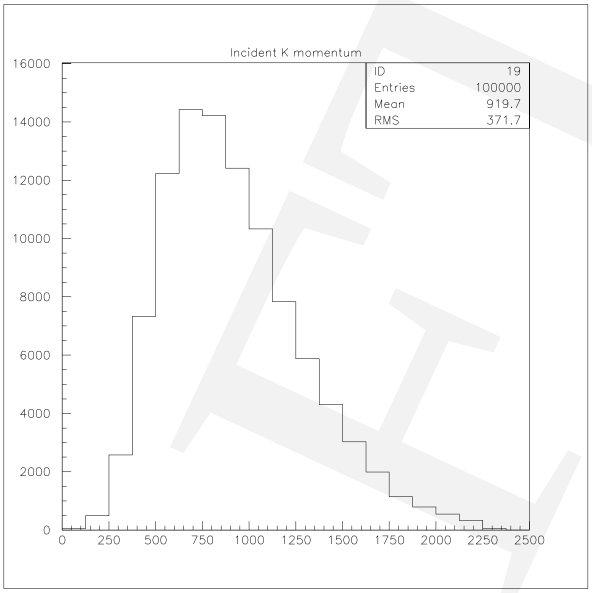

Fig. 17. The calculated K_L^0 momentum spectrum (MeV) at the entrance to the decay region.

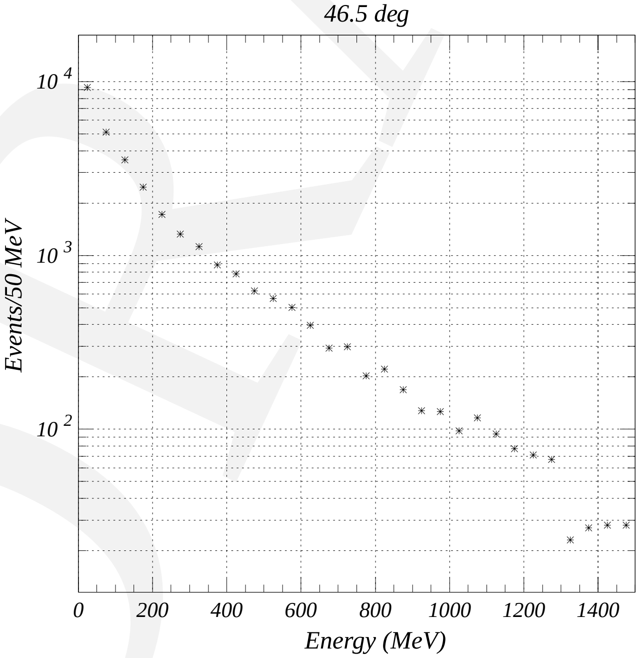

Fig. 18. The measured neutron energy spectrum at 46.5°

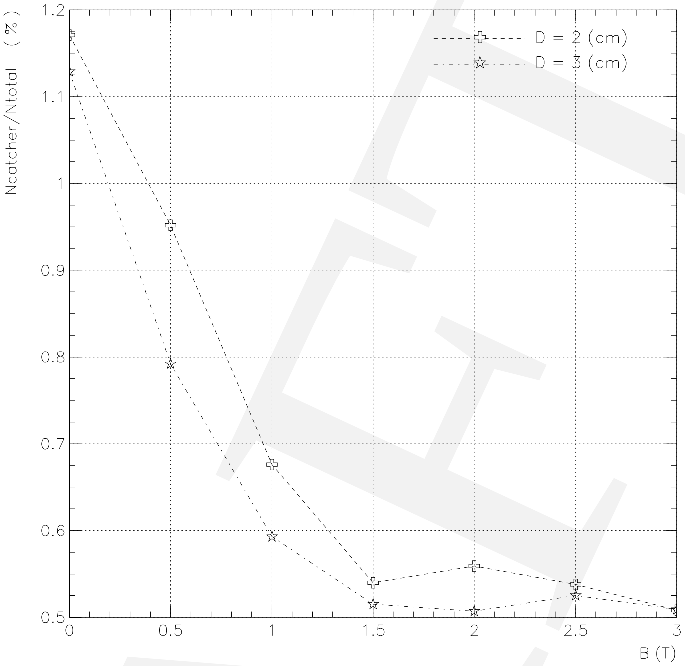

Fig. 19. Fraction of photons in the neutral beam as a function of the magnetic field integral of the upstream sweeper magnets.

The neutron component expected in the beam was measured by the collaboration in a test run using primary protons in the B Line at the AGS with a scintillation counter time of flight wall and BaF_2 detector. The resulting neutron spectrum measured at 46.5^{o} is given in Fig. 18.

Sweeping magnet design

Photons originating from the production target region, primarily from π^0 decays, are to be converted by a series of 70 1mm thick Pb foils in the magnetic field of a pair of sweeping magnets which deflect charged particles vertically. The beam divergence in the vertical direction was chosen to be small, 5 mr, by collimators immediately downstream of the sweeper magnets to constrain reconstruction of candidate π^0 decay vertices to a limited region of space and to effectively reduce the charged component of the beam as well as the the e^+e^- pairs resulting from photon conversion. The dependence of the transmitted photons on the magnetic field along the neutral beam axis as determined by simulation is given in Fig. 19. The horizontal collimation defines an acceptance of 100 mr.

The conceptual design drawings of the upstream charged particle sweeping magnets at the front end of the neutral secondary beam were developed with 3 dimensional field simulations using the *OPERA* program. The magnet cores and coil configurations for the first and second sweeper magnets are displayed in Fig. 20 and Fig. 21, respectively.

The charged particles are swept vertically for better separation from the neutral beam since the vertical phase space was chosen to be much smaller than the horizontal in the KOPIO configuration. Although the coil design is based on a circular cross section mineral

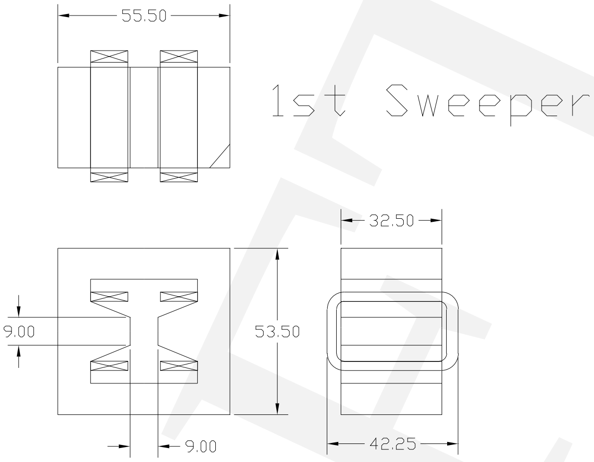

Fig. 20. Configuration of 1st sweeper magnet. Dimensions are given in inches.

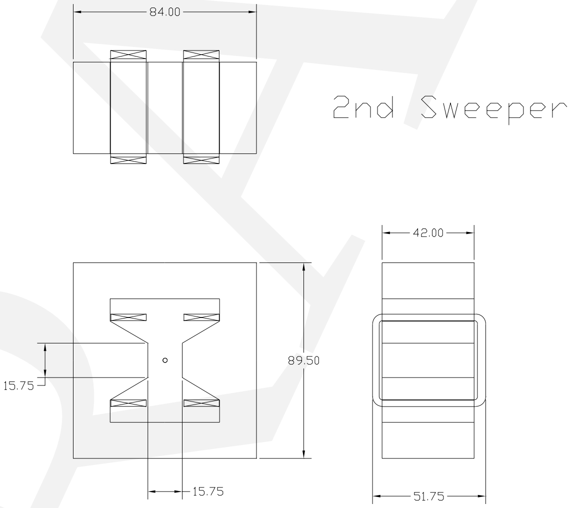

Fig. 21. Configuration of 2nd sweeper magnet. Dimensions are given in inches.

insulated (radiation hard) copper conductor that is presently available, square cross section conductor produced by Hitachi has recently been found which will give an enhanced current density in the coil package of the first sweeping magnet and allow better shielding in this area by replacing some of the volume required by low density coils with lead and/or hevimet.

Simulations using conceptual configurations of the sweeper magnets including the coil packages have met the design criterion of 3.5 Tm for the horizontal integral magnetic field. The dependence of the horizontal magnetic field along the neutral beam axis is given in Fig. 22.

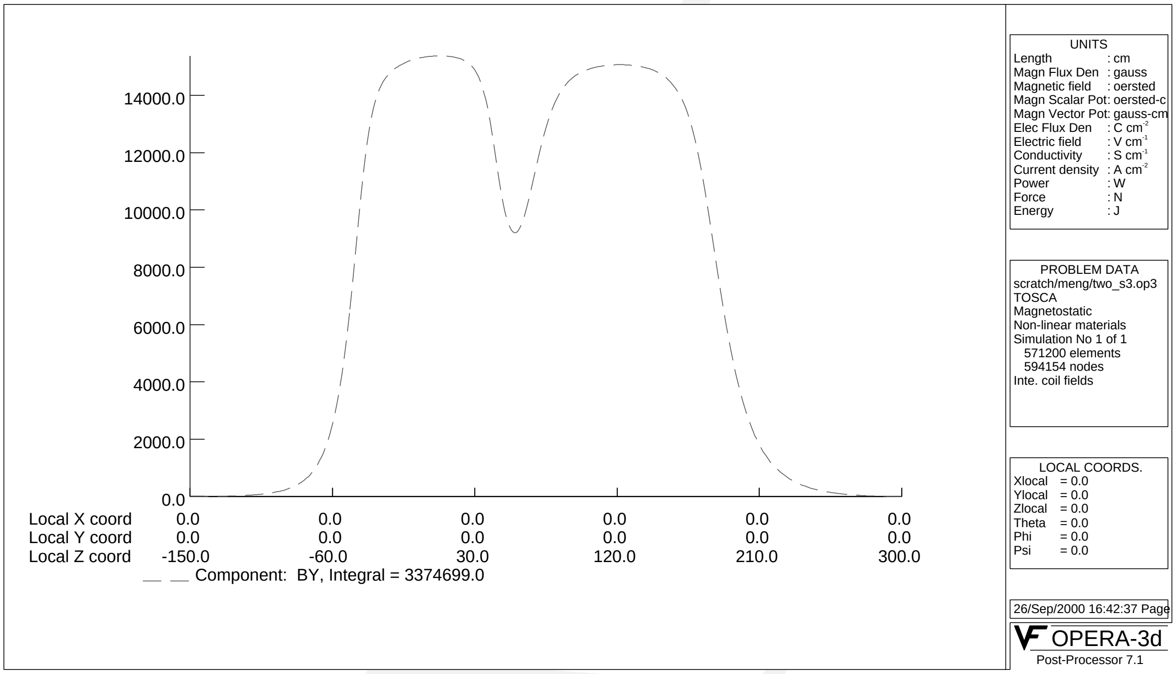

Fig. 22. The horizontal component of magnetic field as a function of longitudinal position along the sweeper magnet axes. The magnetic field is in Gauss and the horizontal axis is in cm.

Collimator design

Since the suppression of neutron background, particularly in the wings of the neutral beam distribution, will be critical to the success of the experiment, two independent simulations are in progress. The first employs GEANT3/GCALOR to study neutron interactions at all energies. The second simulation is based on a different code, Monte Carlo Neutral Particle (MCNPX), which is optimized to the region below 1 GeV.

Figure 23 depicts the collimator design concept in which the first two apertures are opened to move the projected apex upstream of the production target and the last two collimators are opened to minimize beam halo produced in the last collimator. GEANT3/GCALOR has been used to study π^0 production by neutrons in the KOPIO neutral beam since this background could be a major source of spurious triggers. The simulations included the photon spoiler consisting of 70 1 mm thick Pb γ converter foils at 2 cm intervals in the sweeper magnet region. It was found that the halo of neutrons with momentum greater than 0.5 GeV/c, the π^0 production threshold, resulted from beam neutrons interacting in the last collimator. Figure 24 shows the calculated neutron halo for this geometry with the last collimator consisting of tungsten (rather than lead used in the upstream collimators). The distributions were obtained in both geometries for 4×10^{10} protons incident on a model production target (dimensions $2 \times 2 \times 100$ mm^3).

Vertical misalignment of the target and collimator axis of more than 1 mm has been shown by simulation to produce large neutron background. Figure 26 illustrates the result of ver-

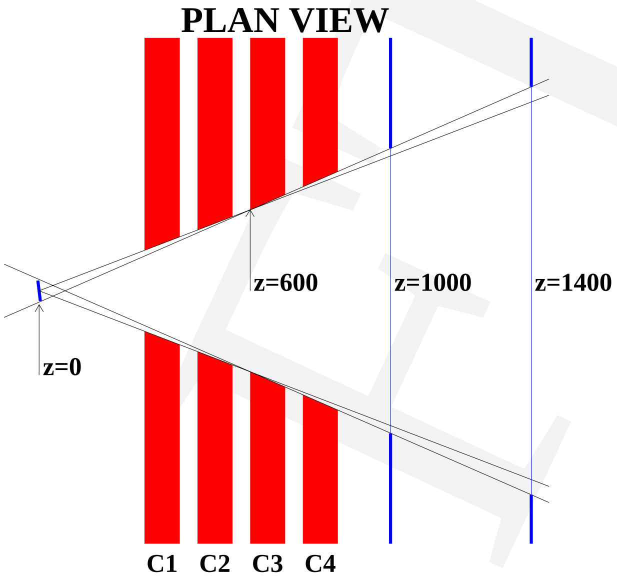

Fig. 23. Collimator Configuration.

tical source misalignment with respect to the collimator system. The collimators are to be mounted on a strongback, i.e. a thick steel plate, in order to maintain their vertical relative motion to less than 1 mm. The strongback will be supported on three vertical adjustment jacks which can be remotely adjusted. Positional reference markers will be installed that will allow direct monitoring of the vertical collimator position. In addition, a remotely controlled vertical positioning of the production target is under consideration.

Since the collimator region of the beam will be maintained at a vacuum of 10^{-7} Torr, the collimators will be coupled by a flanged vacuum pipe with a rectangular cross section. The coupling sections will be of significantly larger transverse dimensions than the collimator apertures in order to avoid interactions with the neutral beam. Simulations will determine the dimensions. It will be necessary to electroplate the surfaces of the lead and hevimet collimator that are in the vacuum region in order to obtain the requisite vacuum.

Simulations with MCNPX are in progress to study the effect of materials such as hevimet, steel, concrete and borated polyethylene in various positions in the collimator array on neutron halo. The MCNPX code lacks magnetic field capability and requires many hours of computer time to acquire statistical accuracy in cases of deep penetration such as the 23 interaction lengths of Pb in the KOPIO collimators. The first simulation results were based on a model collimator array that was similar to that of the KOPIO proposal along the beam axis but had cylindrical symmetry about the axis rather than rectangular apertures in order to study the material effects with good statistics. The introduction of polyethylene between the Pb walls resulted in a large reduction of 20 MeV or less neutron flux penetrating the collima-

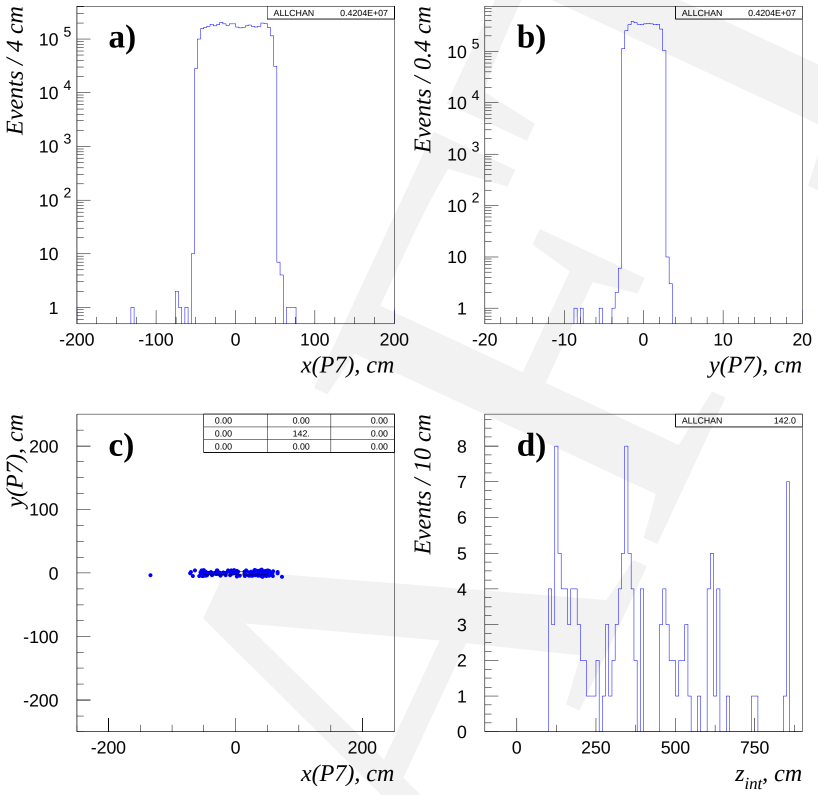

Fig. 24. Neutron halo in the proposed collimator configuration. a) horizontal profile; b) vertical profile; c) X-Y distribution of halo neutrons at Z=1000 cm; d) Z distribution for production of neutrons of 0.5 GeV/c or more.

tors. This flux is plotted as a function of depth in Fig. 26. Although γ's produced in neutron capture are below the threshold for π^0 production, they have the potential to introduce significant dead time unless veto counter thresholds are raised to undesirable levels. Further studies of neutron attenuation with borated polyethylene and concrete are in progress. Following optimization of the collimator design, simulations of the low energy neutron distributions outside the neutral beam are planned with emphasis on the veto counter regions.

An early test run is planned when the primary beam modifications are complete, the upstream sweeper magnets are installed and powered and the collimators are in place. This will allow verification of the simulations and tests of possible modifications of the collimator arrangement and materials. Bonner spheres and He^3 proportional counters will be employed to study the neutron profile at the beam edges and to search for weak spots in the shielding and collimation.

Although a general layout of the collimators has been included in beam simulations, a

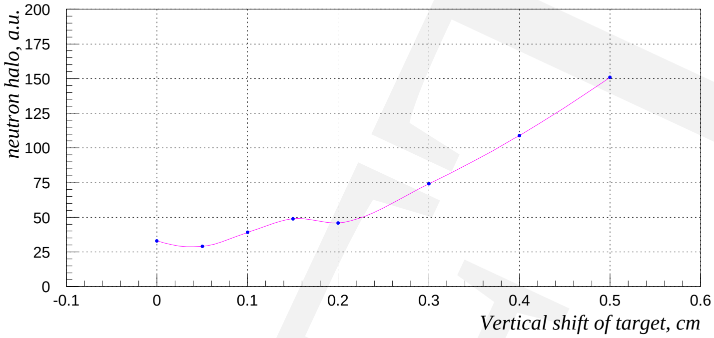

Fig. 25. The relative dependence of the neutron halo on vertical target misalignment with the collimator system axis (arbitrary units).

mechanical design of the collimator system has not been undertaken at this time. The configuration of hevimet and possibly other materials close to the beam region remains to be modeled. Inasmuch as the floor in the AGS experimental areas is known to settle by as much as 3 mm under load and to have a seasonal dependence that is believed to vary with the water table level, it is anticipated that means of periodic survey and remotely controlled jacks under the collimator elements will be required. A similar requirement was satisfied by this method some 15 years ago for AGS E791.

Downstream sweeping magnet.

A large sweeping magnet will be required downstream of the detector region in order to sweep charged particles out of the beam region into the downstream veto counters and away from the beam catcher. A 48D48 spectrometer with a pair of booster coils opened to a 2.4 m gap has been modeled and the results appear to meet the field requirements. Figure 27 illustrates the 48D48 configuration. The horizontal magnetic field component in the median plane varies from 886 Gauss at the center of the gap to 1083 Gauss at the poles. The variation of the horizontal component of field is relatively small over the much smaller vertical acceptance of the neutral beam. Magnetic field simulation gives an integral field along the axis of the magnet of 1.5 Kg-m which increases to 2.1 Kg-m for a parallel path near the corner of the neutral beam envelope. This is sufficient to deflect charged particles of less than 3 GeV/c out of the downstream beam into the veto counters. This would include the peak of the charged particle spectrum from the decay of neutral particles produced at 45^o.

Construction Schedule.

Construction of the primary beam and the upstream section of the neutral beam including the upstream sweeping magnets and the first two stages of collimation is planned for an early test run. This has been given high priority in order to have an advanced measurement of the neutral beam halo and to verify the predictions of the background simulations. The present

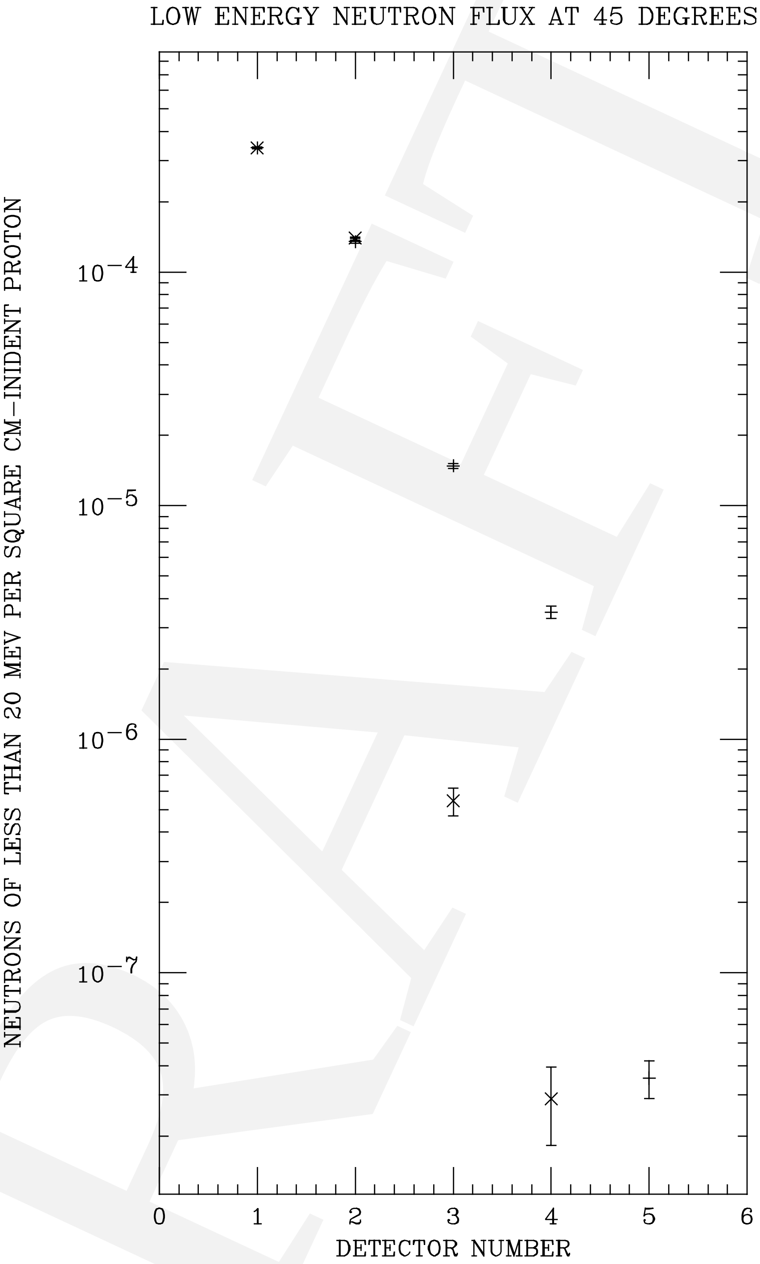

Fig. 26. MCNPX simulation results giving neutrons/cm^2/incident proton as a function of depth in the collimator array. The data is given for points behind each of four 1 meter thick Pb collimators separated by 50 cm with a conical aperture whose axis is at 45^o to the production target. The points indicated by × were obtained with polyethylene filling the spaces between the Pb collimators whereas those represented by + are for empty spaces.

estimate anticipates 18 to 24 months of construction.

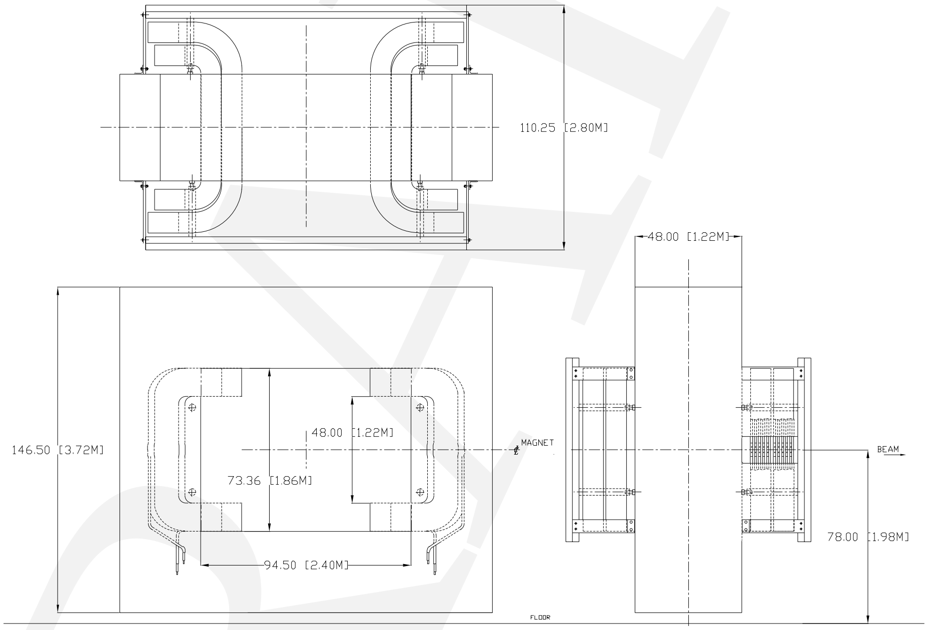

Fig. 27. The Downstream Sweeping Magnet. A 48D48 spectrometer oriented to produce a horizontal magnetic field across a 2.4 m horizontal gap.

5 Detector

5.0 Vacuum

The entire vacuum can be seen in Fig. 5. The decay volume and the beam path upstream of the detector to the spoiler must be at high vacuum ($\sim\ 10^{-7}$ Torr) in order to suppress background from neutron and K^0 interactions with the residual gas. These interactions are problematical, especially in the detector decay region, since they can produce π^0s which might simulate $\pi^0\nu\bar{\nu}$ events. The motivation for this level of vacuum is described in the section on sensitivity and backgrounds. The upstream end of this high vacuum region begins directly after the photon spoiler, in the magnetic field region of the sweeping magnet. The window at this location is part of the spoiler.

The vacuum region from the spoiler to the decay volume houses the collimators which define the neutral beam (described in the beam section). It is thus lined with lead and tungsten which is electroplated or coated with high vacuum paint to minimize outgassing.

There will be several pumping stations along the beam line to maintain the high vacuum. These are yet to be designed. A vacuum engineer has examined the beam layout, however, and is confident that an adequate pumping system can be built. One advantageous feature of this vacuum section is that it will be totally metallic and will not house active detector elements. Thus there will be a minimum of outgassing, little reason to open the system, and a long duration for pumping.

In the decay region the vacuum must be contained in a vessel whose walls are constructed of a minimum of material ($\leq\ 5\%$ X_0) in order to reduce photon conversions and photon production from electrons and positrons. It must have entrance and exit beam pipes which are as close to the beam as practicable. These pipes must also be made of thin material (both in thickness and radiation lengths) to minimize absorption of photons or interactions of neutrons that impinge upon them.

The vacuum vessel in the decay region is shown in Fig. 28. An exploded view showing assembly of the vessel and charged particle veto is shown in Fig. 29. The latter figure was prepared by Advanced Energy Systems, Inc., an engineering firm employed to collaborate in the design of the vessel.

The primary method of construction of the barrel and flat end covers utilizes aluminum honeycomb core material with bonded thin metal skins. The beam-pipes are thin-walled externally-ribbed tubes that will either be adhesively-bonded, brazed, or welded to the end-plates, depending on the final combination of materials. There are flanges between the end cap and barrel regions of the vessel which contain feed-throughs for the charged particle veto system.

Because of the large horizontal to vertical aspect ratio of the beam, the mechanical design of the beam pipes deserve special consideration. To give the pipes sufficient strength while maintaining a thin wall, external ribs are brazed, welded, or bonded to the pipe material. Their thickness, in radiation lengths, will be comparable to that of the inactive components of the preradiator modules so that particle detection near the beam pipe will not suffer.

Preliminary structural analyses indicate that this design approach is viable, and additional engineering consultants have verified this. Trade-offs on the choice of materials and assembly concept development are in progress. Beryllium would be the material of choice, due to its relative stiffness to weight ratio and long radiation length (35.3 cm vs. 8.9 cm for aluminum). However, beryllium is very expensive, so we are considering other materials, *i.e.*, aluminum, in less critical areas - specifically the barrel and upstream barrel end cover.

The downstream beam-pipe extends through the preradiator and calorimeter, and terminates in a thin window separating the high vacuum from the abutting low vacuum. Downstream of the window is a large evacuated region at a pressure less that 10^{-3} Torr. This region contains the downstream veto system and terminates with a 3 m wide by 20 cm high aluminum window. There are few constraints on the housing of this volume, and engineering design has yet to begin.

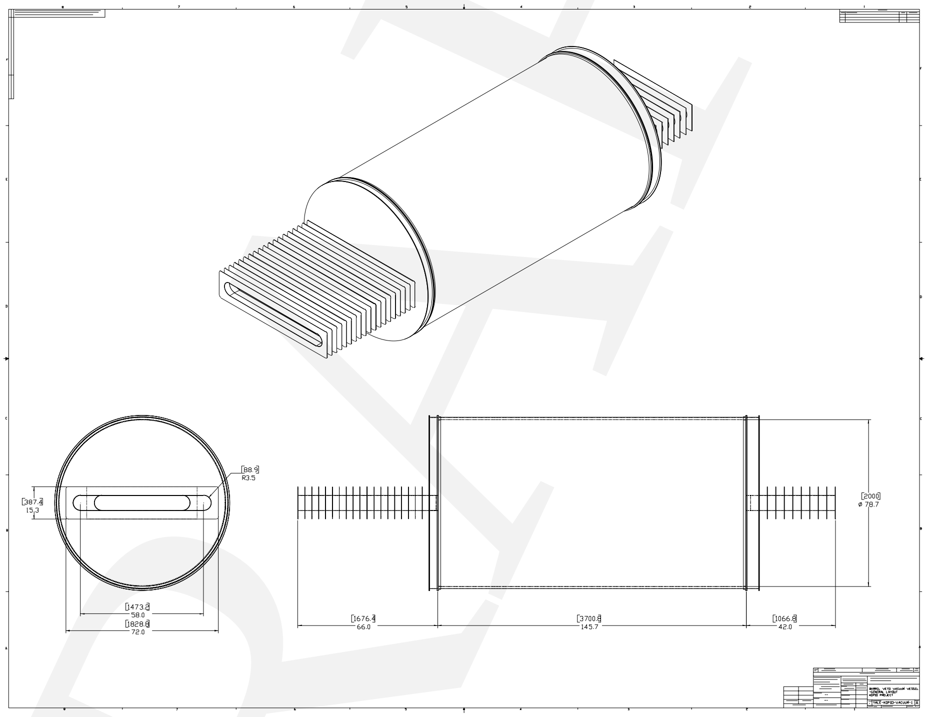

Fig. 28. The vacuum vessel in the decay region. The diameter of the vessel is 2 m, and the length of the cylindrical barrel is 4 m. Dimensions on the engineering drawing are in inches.

5.1 Preradiator

The energy and direction measurements of photons by the KOPIO preradiator/calorimeter combination along with momentum tagging of the K_L by time-of-flight provide positive identification of the signal and powerful kinematic constraints for suppressing backgrounds. Among the most effective constraints are the mass of the two photons ($m_{\gamma\gamma}$), and the center of mass energy of the π^0 ($E^*_{\pi^0}$). Vertex restrictions from photon tracking help in rejecting

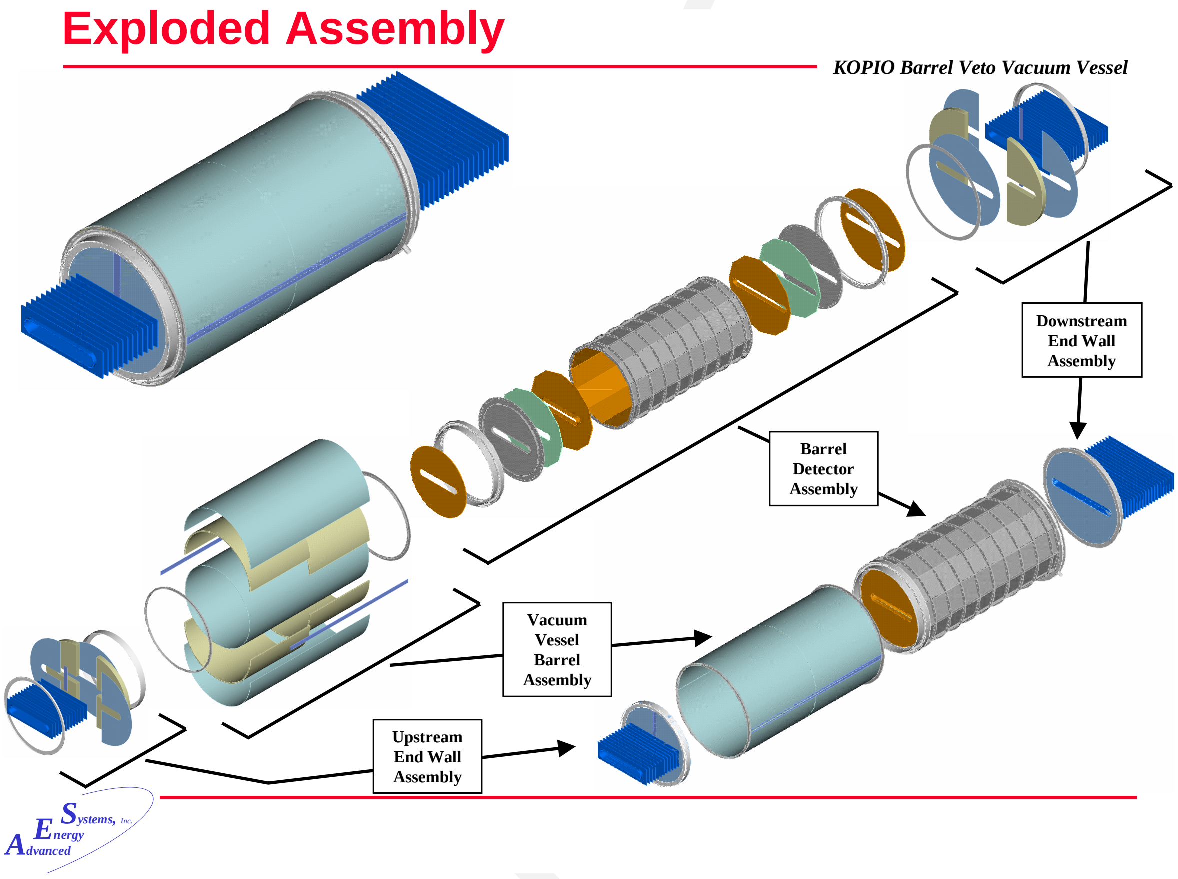

Fig. 29. Exploded view of construction of the decay region vacuum vessel including the charged particle veto, *i.e.*, Barrel Detector Assembly.

accidentals and vetoing particles produced near the surface of the detector by the beam halo. The preradiator (PR) also works as a part of the photon veto system, detecting extra photons.

The requirements of the PR include a photon angular resolution of approximately 25 mrad, a photon conversion efficiency of about 0.7 ($\sim$2 X_0), a shower position measurement of 0.45 cm, and a good measurement of the deposited energy since a large fraction of the photon energy will be deposited in the PR. The linear extent along the beam direction needs to be as short as possible to limit the shower size at the calorimeter. The first-level trigger requires information on the number of converted photons, which can be obtained by segmenting the detector.

5.1.1 Design concept

Since tracking precision is limited by Multiple Coulomb Scattering (MCS) and the later parts of the initial e^+e^- tracks following photon conversion are distorted, the PR obtains the initial direction of the photon from the positions of the e^+e^- pair in the first few consecutive converter/detector layers after the conversion. To keep MCS at the 25 mrad level, the PR layers each containing ≤ 0.035 X_0 are separated by about 1.5 cm and have position resolution of 150–200 μm. Each PR layer consists of planes of inactive converter material, dual coordinate drift chambers for position measurements, and 8 mm thick plastic scintillator for energy and time measurements.

The detectors chosen for the PR position measurements are planar cathode-strip drift-chambers with small cells in which one cathode plane is segmented into strips running perpendicular to the wires—the use of small cells allows the chamber to operate at high rates. One coordinate is given by the drift time and the second by the charge centroid on the cathode strips; an avalanche produced on the anode wires by drifting ionization induces a charge distribution on the cathode plane, and interpolation of the charge induced on the strips allows measurement of the track position along the wire to an accuracy of ≤ 70 μm limited (for normal incidence) by the signal-to-noise ratio of the charge measurement. Strips can be manufactured to high mechanical precision, and control of gas pressure, temperature and mixture is not critical to high quality operation.

Because the separation between the e^+e^- pair in the PR is generally not large enough to generate separate pulses, the drift-time measurements from anodes only trace the particle nearest to each anode wire and sometimes mixing of the two tracks can occur. The expected angular resolution (based on Monte Carlo (MC) calculations) using only anode information is of order of 30–40 mrad and does not depend on the entrance angle of the photon to the plane. On the other hand, because of the two contributions to the induced charges on the strips, the cathode measurement detects the average position of the e^+e^- pair and provides an angular resolution of 15–35 mrad[1], which is, however, dependent on the entrance angle due to statistical fluctuations. To complement these effects the direction of the anode wires (cathode strips) will be alternated vertically and horizontally (horizontally and vertically) for each PR layer.

Figure 30 shows the angular resolution of photons as determined by a GEANT simulation of the PR assuming 150 μm position resolution for both the cathode strip measurements of e^+e^- pairs and drift times of initially detected ionization. The resolutions (σ) obtained are dominated by MCS and vary from 15 mrad at $E_\gamma = 450$ MeV to 33 mrad at $E_\gamma = 150$ MeV. Using position resolutions up to 350 μm worsened the angular resolutions by about 10 %. The case shown in Fig. 30 uses anode drift time information from the first chamber struck by the e^+e^- pair and averaged position measurements from the cathode strips of the second and fourth chambers hit.

The concept of early e^+e^- pair measurements was confirmed by the KOPIO group[2] using a low energy photon beam (100–300 MeV) at the BNL NSLS. As shown in Fig. 31, the angular resolutions obtained from cathode strips agreed with the MC calculations; $e.g.$ 31 mrad at 150 MeV and 25 mrad at 250 MeV. The results also showed that the resolution obtained from anode information is comparable with the expectation of the simulation. The energy deposited in the PR will be measured in the scintillator layers with sufficient precision to allow the full energy measurement (including the PR and the calorimeter) to be better than 2.7%/$\sqrt{\mathrm{E}}$. The large fraction of active material (scintillator) in the PR is crucial for obtaining good energy resolution. In addition, the scintillation counters are used for triggering and timing measurements. The scintillator will be segmented into 20 cm wide strips to provide

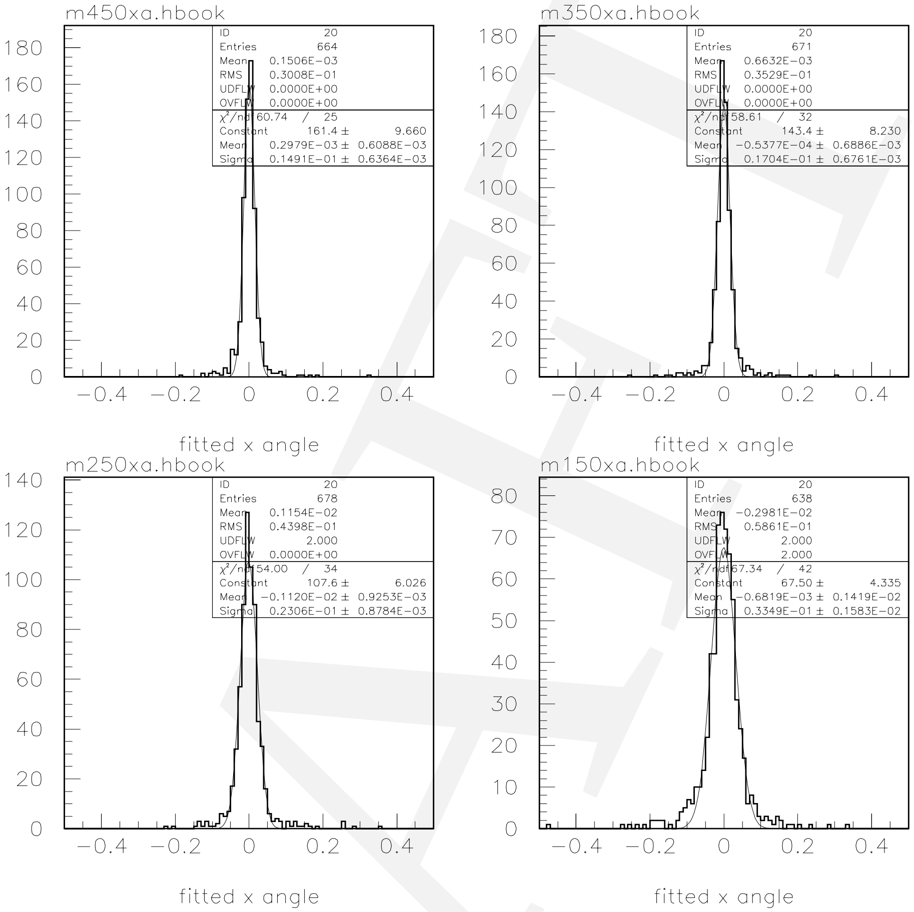

Fig. 30. Results of GEANT simulations for angle measurements at incident photon energies of 450, 350, 250 and 150 MeV.

information on the number of converted photons using the numbers of hits and clusters.

5.1.2 Mechanical construction

As shown in Fig. 32, the PR system will be divided horizontally and vertically at the center lines into four 2.5-m×2.5-m quadrants.

The inner 2-m×2-m areas are instrumented with drift chambers, radiator materials and scintillators, while the outer areas are instrumented with radiator and scintillator only for photon vetoing; there are additional 1-mm thick lead plates in the outer regions to augment the photon detection efficiency. At the inside corner of each quadrant there is a rectangular cut-off to accommodate the beam hole. A quadrant has 64 layers, each consisting of an 8-mm thick scintillator plane, a 0.10-mm thick copper radiator sheet and a drift chamber plane. Eight layers are mechanically combined, forming a self-supporting module. Because of the asymmetric beam hole, there will be two types of mirror image modules.

Drift chamber: Figure 33 shows the structure of one layer. The 2 m × 2 m Al comb chambers

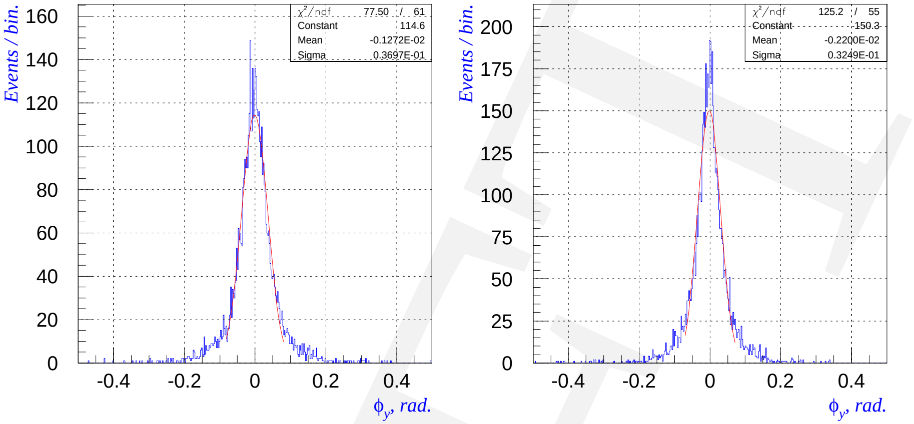

ϕ_y distribution of detected photons. E_γ = 150 MeV. **ϕ_y distribution of detected photons. E_γ = 250 MeV.**

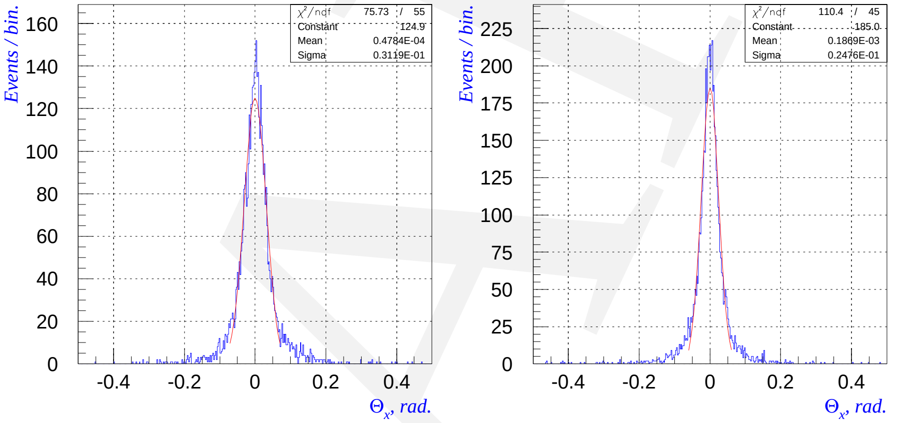

Θ_x distribution of detected photons. E_γ = 150 MeV. **Θ_x distribution of detected photons. E_γ = 250 MeV.**

Fig. 31. Angular resolution measurements using photon beams. The plots at the top row are obtained using only anode information and the bottom, using only cathode information. The plots in the first column are taken at $E_\gamma = 150$ MeV and the second at $E_\gamma = 250$ MeV.

based on extruded Al channels provide a simple, compact PR with adequate performance and mechanical stability. 30 μm thick Au-plated tungsten wires are strung at the centers of 5 mm$\times$5 mm square drift-cells through crimp pins sitting in precision-machined holes. The Al channels surround three sides of the square cell with a 0.5 mm thick base and fins that are 3.5 mm high and 0.25 mm thick. The fourth cell-side is a 0.15 mm thick G-10 plate with 7-mm pitched cathode strips of thin copper coating oriented at 90° to the wires and spaced 2.5 mm from the wires. For long horizontal wires, small plastic wire-support pieces will be installed about every meter.

The high voltage is applied to each anode wire, simplifying the extraction of pulse height information from the cathode strips and allowing 'problem' regions of a detector-layer to be turned off by removing HV; the Al extrusion design removes the need for guard wires at the edges and largely isolates each of the wires. This feature, plus the use of crimp pins, allows

Table 2. Unit parameters

Units	Number	Size	r.l. (X_0 along Z)
Quadrant	4		
whole assembly		2.5m×2.5m×1.1m	14.9 (outer 0.5m)
with chambers		2.0m×2.0m×1.1m	2.2
Module	8 /quad.	13 cm thick	0.28
Layer	8 /mod.	1.39 cm thick	0.035

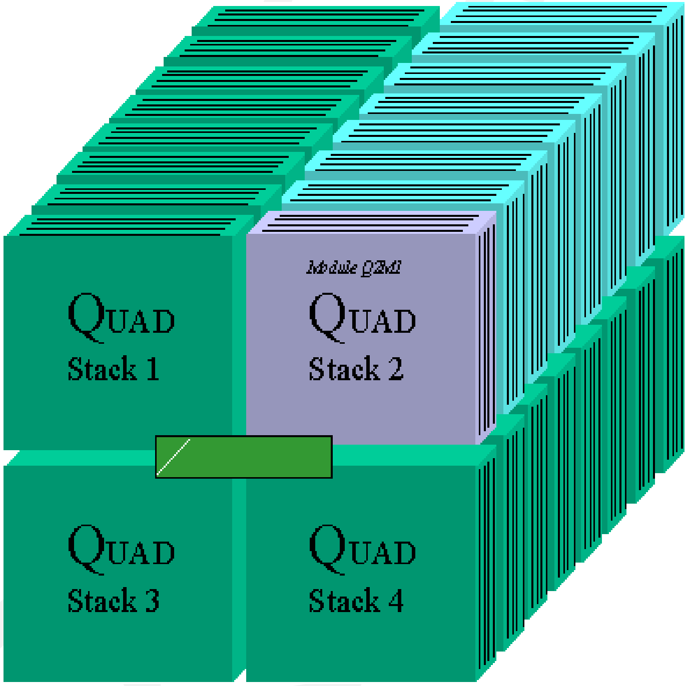

Fig. 32. The PR is devided into four quadrants. The rectangular cut out in the middle is for the beam hole. The gaps between the quadrants are for illustration.

the possibility of removing and replacing a broken or loose wire without disassembling a module. Alternatively, a problem wire can be removed and the crimp holes plugged; the Al extrusion allows one to have a missing wire, without causing high gas gain on the adjacent wires.

The cell performance simulated by GARFIELD was adequate; the cathode field is ≤10 kV/cm when the anode field is ∼300 kV/cm. A typical isochrone plot is shown in Fig. 34, where each isochrone represents 5 ns drift time. The maximum drift time from the corner of the cell is about 70 ns for an Ar/ethane (50/50) mixture.

Extruded Al channels have been produced with the specifications indicated in Fig. 33 by the Northern State Metal Corp.[3]. The tolerance on the overall flatness of the extruded Al

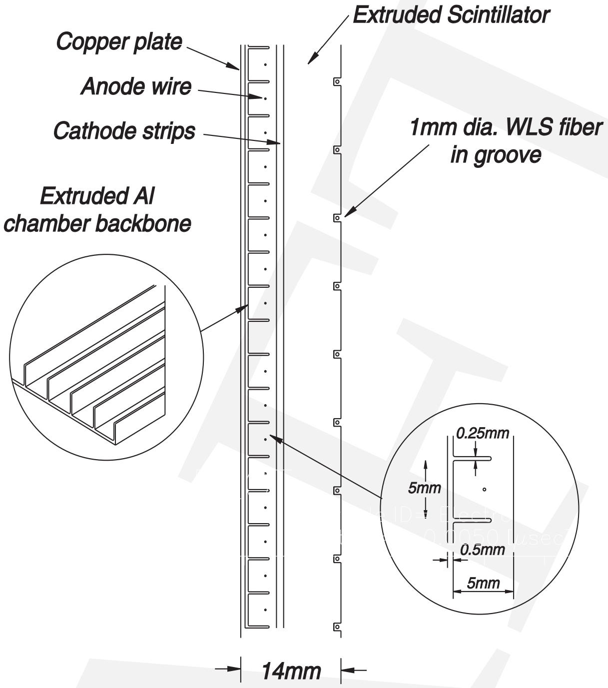

Fig. 33. Layout of one layer; planary drift chambers in Al channels, extruded scintillator with grooves, and converter.

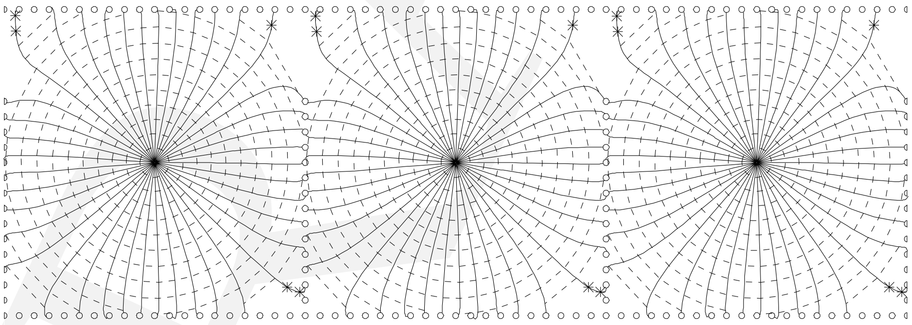

Fig. 34. Isochrones; each isochrone corresponds to 5 ns of drift time in Ar/ethane (50/50) gas mixture.

structure up to 2 m in length is of order of 150 μm.

Three short eight-cell prototype chambers with extruded Al channels have been constructed to test the anode performance of the cell design. They were operated with an Ar/isobutane (75/25) mixture and a CF_4/isobutane (80/20) mixture. The cell has a plateau of $\geq$200 V around 1300 V. The results are shown in Fig. 35. For the Ar/isobutane (75/25) mixture, the maximum drift time was 75 ns which corresponds to the drift time from the corner of the cell.

As shown in Fig. 31, the principle of strip readout for the angle measurement has been

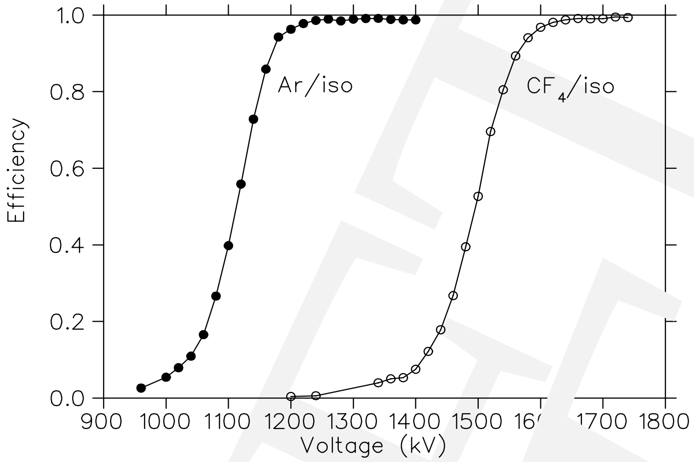

Fig. 35. Efficiency curves for Ar/isobutane (closed [illegible] and CF_4/isobutane mixtures (open circles).

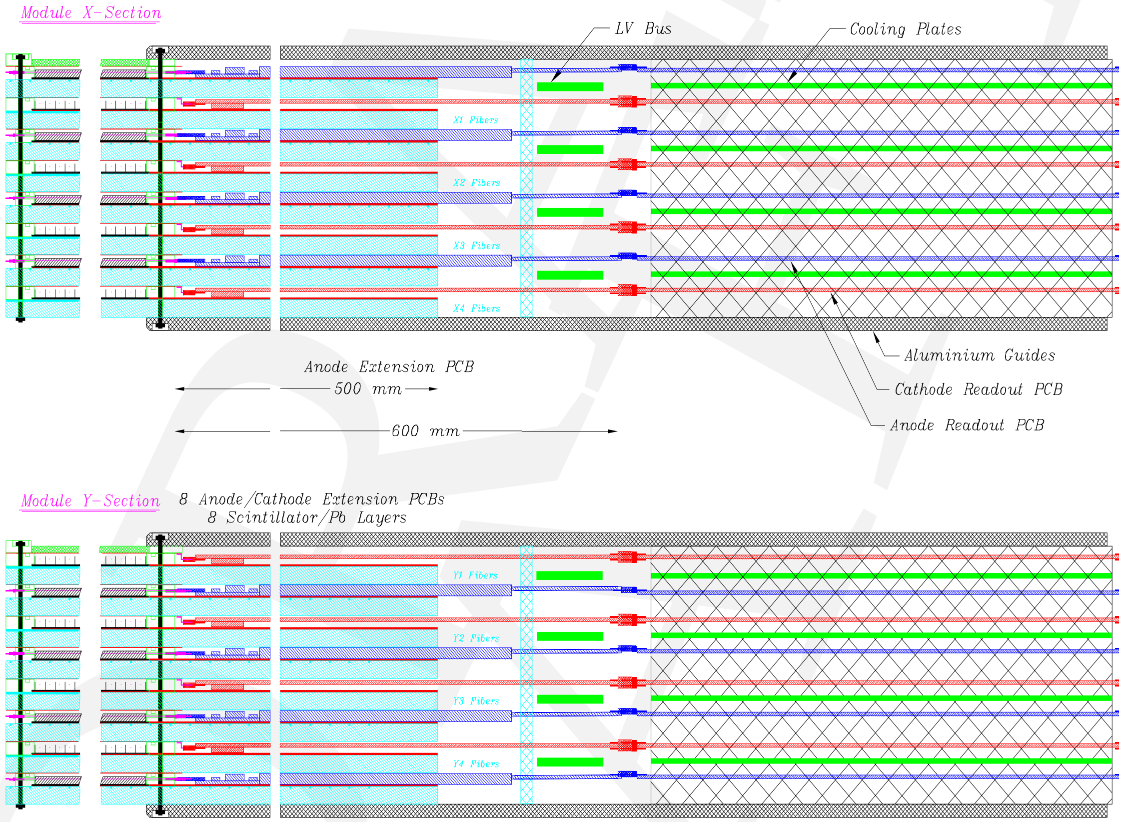

Fig. 36. Module consists of eight layers; the orientation of the chamber plane is alternated in the horizontal and vertical wire direction.

tested using photon beams at several energies. Since the tests were done with a similar cathode geometry but with hexagonal cells, three 30-cm$\times$30-cm Al-channel prototype chambers with strip readouts are being constructed for further tests. Two quarter-size modules fully instrumented with electronics will be constructed to develop construction procedures and test the readout system. These will also be tested in photon and π^0 beams.

Scintillator: Planes of 8-mm thick extruded scintillator (BC404 or equivalent) cover the whole 2.5-m$\times$2.5-m area. To provide two-dimensional information, each plane is divided into 12 horizontal (X) or vertical (Y) strips; 20 cm wide in the inner 2-m region and 25 cm wide in the outer 0.5 m region.

The collection of the light from the scintillator is done by embedded 1-mm diameter wave-length-shifting (WLS) fibers (BCF99 or equivalent) in 1.1 mm deep grooves every 1 cm running along the strip. The barrel photon veto system has the same light-readout scheme with a slightly different thickness of scintillator. The estimated number of photoelectrons based on the prototype studies is 16 p.e./MeV for the PR geometry. The timing resolution for one scintillator plane is 0.7–0.8 ns (see the barrel photon veto section). Since there are two particles causing signals in the scintillator and the average number of hit planes is $\sim$30, the expected timing resolution is better than 0.2 ns. To reduce the influence of phototube noise in the photon energy measurement, we group together fibers from four planes with the same fiber direction, *i.e.* four X planes and four Y planes in each module. One volume unit is then roughly 6 cm in Z and 20 cm in X and Y.

Construction: A PR layer is made from several pre-fabricated parts: (1) the 0.15 mm thick PCB with cathode strips, (2) the 8 mm scintillator layer with its fibers already glued into it and subsequently coated with light reflecting paint (or etched as described in the barrel photon veto section), (3) the 0.10 mm thick copper radiator sheet, (4) the Al extrusion pieces, and (5) the plastic parts for the ‘frame edges’ of the wire-plane which have precision-machined holes for anode-wire crimping pins. The total thickness of a layer is 13.9 mm including the glue thickness of 0.15 mm. Since each layer is very flexible, the layer will be assembled on a large granite table. Layer fabrication consists of holding components in precise alignment with jigs during a series of gluing/laminating steps using a hydraulic press on the granite table. The layer laminated in the above order has the wire-plane at the top of a detector-layer for ease of stringing. After laminating, there will be considerable hand finishing and inspection of the detector layer before it is moved to a clean room for cleaning, stringing and storage. This laminate supports the wire tension load of $\sim$30 kg by the 384 anode wires.

Module assembly will take place in the clean room on another granite table with a hydraulic press. The plastic frame edges (5) also have an O-ring groove at the perimeter of each layer on the top for a gas seal. When a module is assembled, the plastic frame edges on the top and the cathode PCB plane on the bottom of the next layer provide the O-ring seal. The “lid” on the top of the module consists of a cathode PCB and a 4-mm thick plastic backing. The tightening bolts are long (125 mm) and thin (#2-56) since they need to be placed between crimp pins. The only restriction is that the pitch of the bolts be a multiple of the cell pitch (5.25 mm). The hydraulic press will compress the eight O-rings and flatten the module, allowing easy and reliable tightening of the edge bolts. When eight layers are bolted tight to form a module as shown in Fig. 36, the module will be 600 times stiffer than a single layer. The goal of overall module flatness is 150 μm.

In total, each module is 13 cm thick including two 6-mm thick Al support plates on both sides of each module (see Fig. 36). With a charged-particle veto scintillator attached to the upstream face of the first module and gaps of 6 mm between modules, the eight module PR stack will be 1.1 m long, and provide 2.2 X_0 ($\sim$15 X_0 in the outer region). There are approximately 85000 anode wire readouts in the central active region and 65000 cathode strip readouts. There are also 768 photo-tubes. Each PR module, when fully equiped with electronics boards (0.3 t), the Al support (0.15 t) and Cu cooling plates (0.06 t), is $300\times300\times13$ cm^3 and weighs approximately 1.3 t. With 32 modules, the total weight of the KOPIO PR is 42 t.

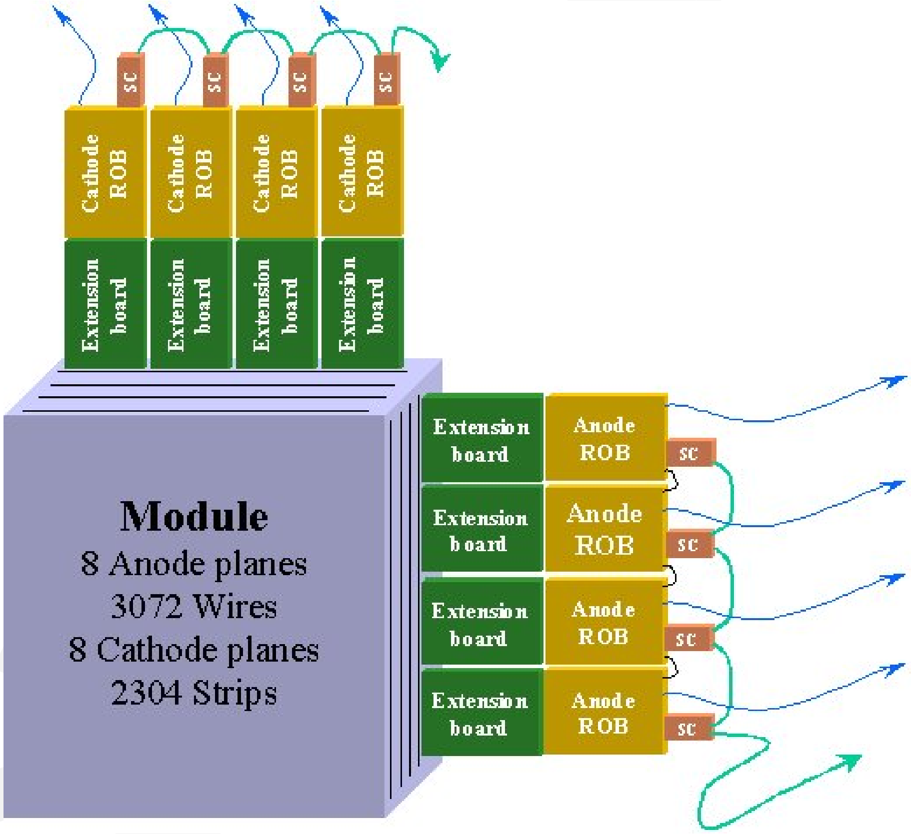

Fig. 37. Readout scheme. Extension and readout boards for only one of the eight layers are shown here. Also, to show the extension cards, scintillator and converter are not shown beyond the active region of the chamber.

Module Support and Installation: Support of the upper two quadrants of the PR is provided from the top, since one of the strong readout edges is facing upwards—in order to minimize the gap between the modules at the vertical and horizontal center lines, there is almost no structural material in the region of the two inner sides of the module. Two aluminium or steel support brackets can extend down to each module from two trolleys on individual overhead beams. To remove one of these modules, it is slid sideways (away from the beam pipe) out of the 8-module stack. It is then lowered down onto a transport/support cradle. Installation would be the reverse of this procedure. The modules of the lower two quadrants will be held on support carts guided by rails.

5.1.3 Electronics

The fully instrumented areas with the chamber electronics increases from 1.5m × 1.5m at the upstream end to 2m × 2m at the downstream end. In order to accommodate the additional lead radiator beyond the active chamber regions, there is not enough gap for electronics and cooling. The signals from the anodes and cathodes in each PR are first transmitted outside the 2.5-m×2.5-m boundary through 0.5 m long transmission lines (extension boards) as indicated in Fig. 37. In the area outside the 2.5-m×2.5-m boundary, the full layer thickness is available for electronics and air cooling. The concept of readout is shown in Fig. 38 for the anode and Fig. 39 for the cathode. The anodes and cathodes from each PR panel will be read out and digitized individually; only digitized information will be taken from the chamber area. Thus, the readout boards on the chambers will each contain the appropriate preamplifiers, discriminators (for time measurements), track and hold circuits (for analog measurements), multiplexing, and digitization circuitry. The front-end system will be optically connected to the DAQ system.

Table 3. Number of channels

Electronics	Number of ch./mod.	Total number of ch.
Anode	3072	84480
Cathode	2304	64512
PMT	24	768

Slow Control Boards (SC) will be mounted on the readout boards as shown in Figs. 38 and 39. Their function is to control, diagonose, and monitor the anode and cathode boards, and to provide communication between back-end computer and front-end read-out boards. The threshold levels, amplifier gains and pulse-shaping constants are loaded through the SC board. Data compaction and buffering Field Programmable Gate Arrays (FPGAs) are also controlled by them (see the DAQ section).

Anodes: The anode preamplifier is required to provide fast timing ($\sim$ 1 ns time resolution) under a large capacitance (up to 200 pF). The anode preamplifier Application Specific Integrated Circuit (ASIC) being considered and tested is the CMP16 chips made by the UC Davis Laboratory for CMS. It is a 16-ch amplifier/discriminator chip,[4] which takes about

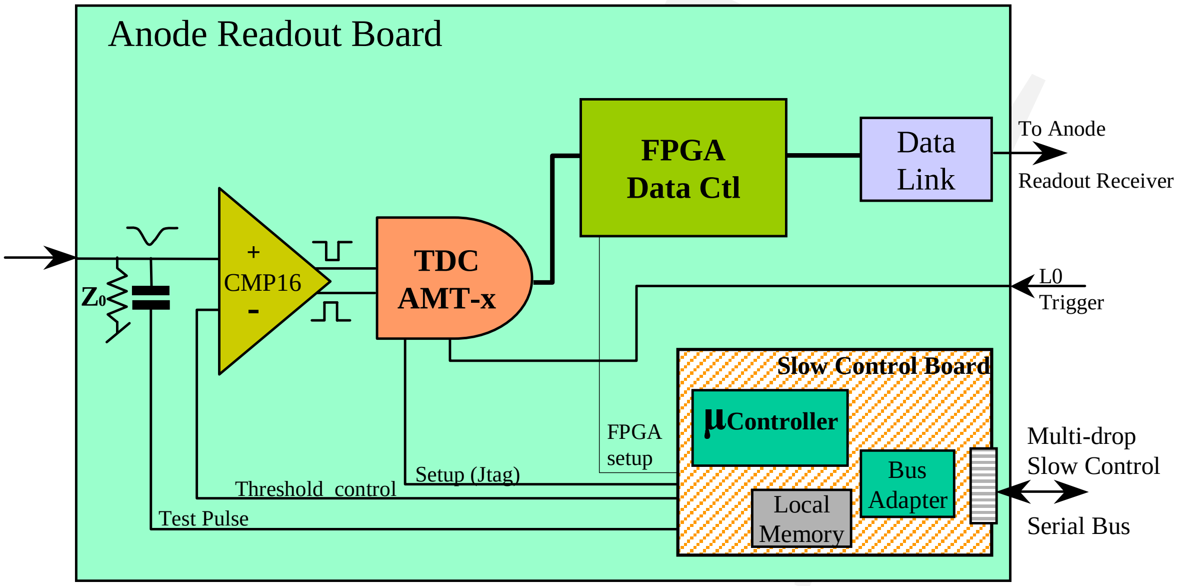

Fig. 38. Anode readout scheme.

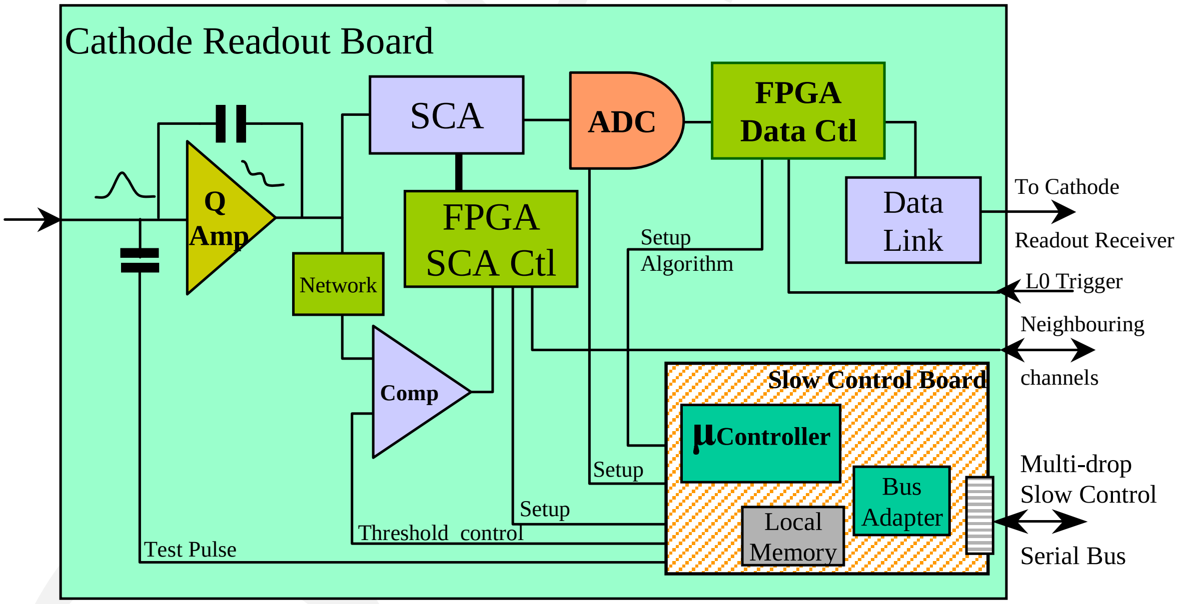

Fig. 39. Cathode readout scheme.

20 mW/ch for the present application. For proper tests of the dynamic performance of the readout system including cross-talk and pulse-shape measurements, a full length Al-comb chamber. though only 10 cm wide is being constructed. The TDC ASIC, AMT-x[5], is based

on the 0.3 μm CMOS gate-array technology. It has been developed by the KEK ATLAS group and is currently under a second revision. This is a low-cost, low-power 24-channel chip which is commercially available. It operates with a 40 MHz clock and fine time interpolation is done by a phase-locked-loop time memory cell. The power consumption is 24 mW/ch when the time resolution is 0.8 ns/bit. It has a built-in buffer memory for each channel and upon receiving a trigger signal the corresponding data are transferred to the next buffer for readout. The trigger latency can be as long as 51 μs. The maximum rate it can handle per channel is 0.5 MHz, which is larger than the expected wire rate of 100 KHz near the beam for KOPIO. All functions of the chip can be controlled externally through a JTAG port. We have obtained four AMT-1 chips to build a 96-channel prototype anode-readout system and test the performance. Further digital buffering and control will be handled by FPGAs.

Cathode: Although centroid measurement requires only relative measurements of the adjacent strips, timing jitter and pulse shape variation affect the results. We attempt to minimize possible contributions to a level lower than 1 %, which roughly corresponds to 70 μm resolution. In order to accurately measure the average position of the e^+e^- pair, whose signals may arrive at the electronics at different times due to the drift time, both contributions of induced charges on each strip need to be added without bias. Our approach is to fully integrate the charge in the amplifier/shaper and measure the maximum height of the integrated pulse.[†] The integrated charge is slowly discharged at a rate of 5 μs. This scheme maintains 1% accuracy in the measured charge ratio of the two tracks for the maximum drift time of 50 ns, while the charge stored in the capacitor is kept low enough to allow the necessary dynamic range.

For the cathode preamplifier, options being considered include an in-house design based on a commercial chip (MAX4223 or CLC425). We have built a test preamplifier as shown in Fig. 40a. Two pulses separated by 400 ns were injected through 1 pF capacitors and integrated with a decay constant of 20 μs as shown at the top of Fig. 40b, and the differentiated pulse shape at the bottom is the output for the comparator. The preamplifier will be tested further and developed first using the three 30 cm × 30 cm prototype chambers and then the full length chambers which provide more dynamic tests.

The pulse shape will be stored in a 20-MHz, 16-channel, 96-bucket deep switched capacitor array (SCA) developed for CMS muon chambers.[6] The noise level of each SCA channel is of order of 0.5 mV for a 1-V pulse. The output of the preamplifier also feeds the self-triggering comparator ASIC which is also from CMS. The comparator output informs the FPGA where the valid time buckets are stored in the SCA. The charge in a valid bucket is then converted by a 20-MHz 12-bit ADC and the digitized output is stored in the buffer FPGA. As long as the number of valid buckets in the 16 SCAs are less than the bucket depth at a time, the pipeline feature can be maintained without any dead time. There will be a conversation between the neighboring FPGAs so that when one strip is hit the adjacent ones are also read out regardless of the amount of charge. The digital section handling data filtering

---

[†] If not integrated, coarse sampling introduces variation, in the observed pulse shape, with the relative phase between the signal and the clock. Fast sampling ADC's (∼100 MHz or faster) with a modest pulse shaping constant (∼100 ns), after digital integration of the ADC counts, could provide desired accuracy for any phase. However, those ADC's consume much greater power.

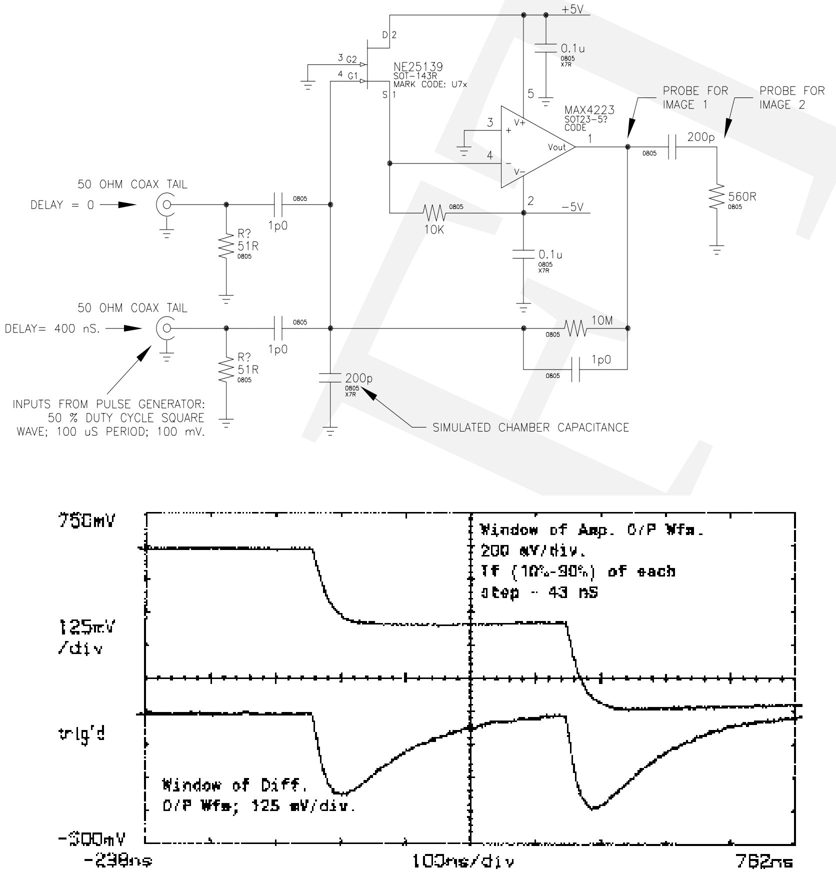

Fig. 40. a) Cathode preamplifier and b) Pulse shapes after cathode amplifier with a step-function pulse input through 1-pF capacitors; integrated (top) and differentiated afterward (bottom).

and buffering will be carried out in-house. The FPGAs are used to correlate adjacent hits in space and time, and to reduce, format and buffer the data for further processing.

Scintillator readout: A detailed description of the readout scheme is given in Section 5.2.7. The photo-tube signals from the scintillators are split into two lines; one line feeds a discriminator for the time measurement and the second one goes to a fast ADC for the energy measurement. The discriminator output also goes to the trigger system for cluster counting and other logic.

5.2 Calorimeter

In the KOPIO experimental configuration the endcap calorimeter occupies an area of 5.2×5.2 m^2 behind the preradiator. Photons of interest from π^0 decays first convert to e^+e^- pairs in the preradiator. These electrons and positrons then traverse one radiation length of preradiator, on average, before entering the calorimeter. Thus the photon energy measurements are made through a combination of the preradiator and calorimeter which implies that a calorimeter of modest energy resolution will suffice - modest with respect to that achievable with scintillating crystals.

Because the calorimeter does not see the primary photons, but rather secondary electrons and photons, the granularity of the calorimeter need not be exceedingly high. In fact, because of the need for high efficiency in vetoing background, a ‘coarse’ granularity serves well in reducing the total volume of cracks between modules.

The above considerations lead us to employ the Shashlyk technique for the KOPIO calorimeter. Parameters that can be achieved with such a technique are shown below, and are consistent with the needs of the experiment.

1. Time resolution: approximately 60 ps/ $\sqrt{E(GeV)}$.
2. Energy resolution: $3 \div 3.5\%/\sqrt{E(GeV)}$.
3. Granularity: 11 cm.
4. Radiation lengths: 15.0 (17.0 including the preradiator).
5. Physical length: approximately 60 cm.

Shashlyk modules are lead-scintillator sandwiches read out by means of wave length shifting (WLS) fibers passing through holes in the scintillator and lead. While we propose a module with significantly improved performance over previous manifestations, the technique is well proven, *e.g.*, E865 at Brookhaven[1], and has been adopted by others, *e.g.*, the PHENIX RHIC detector[2], the HERA-B detector at DESY[3], and the LHCb detector at CERN[4].

We have significant experience with the E865 calorimeter which is composed of 600 such modules and ran reliably in a higher rate environment than that expected in the KOPIO experiment. It is from that experience, and improvements which have been prototyped and simulated, that we draw our confidence that the design goals can be reached.

The E865 Shashlyk module had an energy resolution of $8\%/\sqrt{E\,(\mathrm{GeV})}$. In 1998 a prototype module was constructed, studied in a test beam, and measured to have a resolution of $4\%/\sqrt{E\,(\mathrm{GeV})}$. Using this experimental study as a reference point for tuning Monte Carlo simulations, mechanisms for further improvements to achieve the desired performance were determined and have been implemented recently in new prototype modules.

5.2.1 The Shashlyk module.

The design of a module is shown in Fig. 41. The module is a sandwich of alternating perforated stamped lead and injection molded polystyrene-based scintillator plates. The cross sectional size of module is $110 \times 110\ \mathrm{mm}^2$. As presently designed there are 300 layers, each layer consisting of a $0.25\ \mathrm{mm}$ lead plate and $1.5\ \mathrm{mm}$ scintillator plate with a diffuse reflector of white paper between each plate. Each plate has 144 holes equidistantly arranged in a 12×12 matrix, the spacing between the holes is $9.5\ \mathrm{mm}$. The diameter of the holes is 1.5

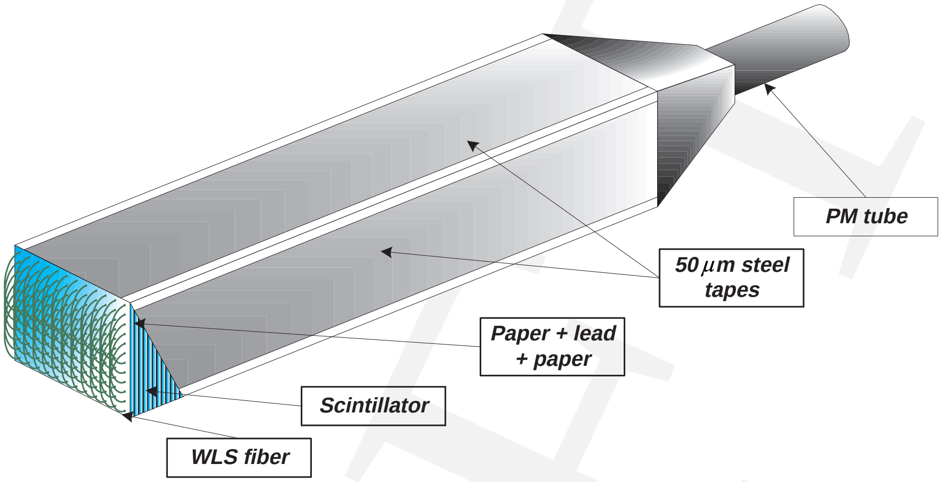

Fig. 41. Shashlyk module design

mm in the lead plates, while the holes in the scintillator have a conical shape with diameter ranging from 1.4 to 1.5 mm. 72 WLS fibers are inserted into the holes, with each fiber looped at the front of the module so that both ends of a fiber are viewed by the photodetector. Such a loop (radius ~ 3 cm) may be considered as a mirror with reflection coefficient of about 90%. The fiber ends are collected in one bunch, glued, cut and polished, and connected to a photodetector.

The complete stack of all plates is held in compression by the four $50\ \mu$m stainless steel side strips that are pre-tensioned and welded to both front and back special endcaps.

5.2.2 Experimental study of prototype modules

The characteristics of various module designs have been studied in the B2 test beam at the AGS with 0.5 - 2 GeV/c electrons and pions in 1998, and in the X5 tagged photon beam at the BNL NSLS in 2000[5]. These prototype calorimeters examined the response to tagged electrons and photons of different energies and the uniformity of response as a function of incident position of the beam within a module. Different photomultiplier tubes (FEU85, FEU115, and EMI - 9903B) and three different WLS fibers (KURARY:Y11(200)M-DC, BICRON: BCF-99-29A-SC and BCF-92-SC) were examined.

The results of resolution measurements (σ_E/E) for the best light collection system (Y11(200)M-DC-S, EMI - 9903B), as well as fits to our Monte Carlo simulation points (where σ_E/E is parameterised as $\sqrt{\mathrm{p_1}^2 + (\mathrm{p_2}/\sqrt{\mathrm{E}})^2 + (\mathrm{p_3}/\mathrm{E})^2}$, and E is expressed in GeV) are shown in Fig. 42. One sees from these results that Shashlyk with the Kuraray fiber and EMI-9903B tube achieves a resolution of 6.7% at 250 MeV/c. If this resolution is expressed as a single number in the customary way, it is $3.4\%/\sqrt{E\,(\mathrm{GeV})}$. The parameters for the more precise expression of resolution are shown in Fig. 42.

GEANT simulations are in good agreement with the data of Fig. 42 when sampling, leakage, holes, light attenuation, photostatistics, and noise are included in the calculation. The measurements were not sensitive to uniformity of light collection.

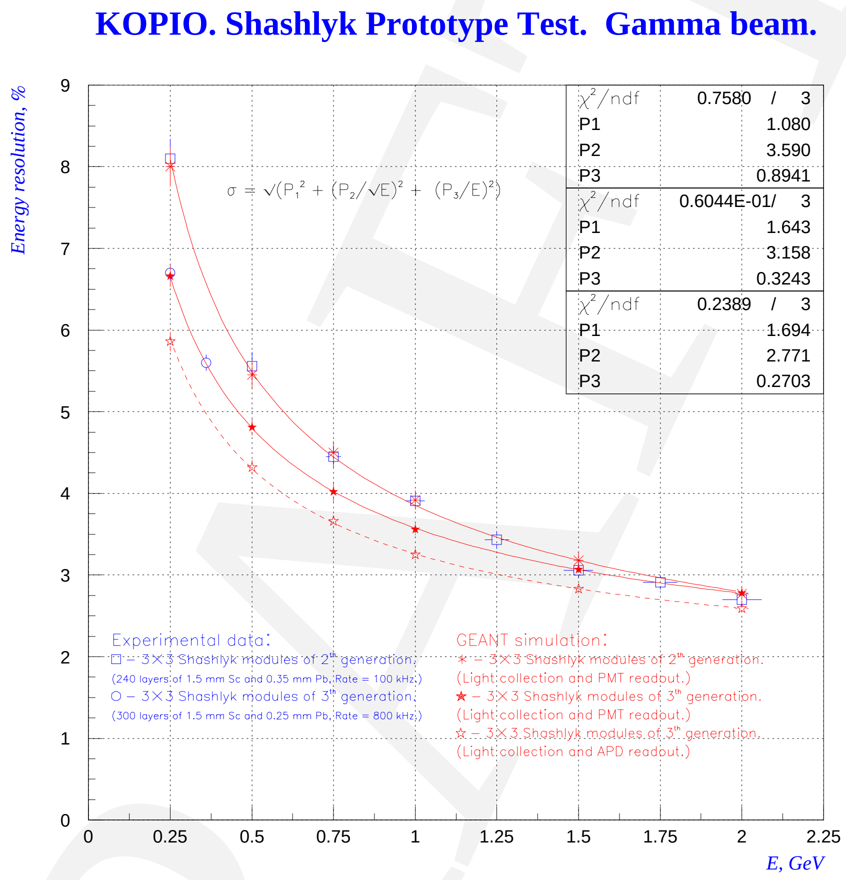

Fig. 42. The energy resolution of nonets of modules versus momentum of the electron beam for configurations indicated on the figure. Both experimental data and results of GEANT simulations are shown.

5.2.3 Improved photo detection

As seen above, the performance of Shashlyk calorimeter modules with PMT readout satisfies the requirements of the KOPIO experiment, and agrees with the simulation. It is also true, however, that our tests measurements were made in an optimum environment for PMT readout: short measuring runs, and continuous and stable photon beams. These conditions do not correctly simulate those that will be encountered in the KOPIO experimental environment. There the beam will cycle on and off every several seconds with a relatively unpredictable average and instantaneous intensity. Due to fractionally large gain variations with changing anode currents, and hysteresis effects when a light source (beam) is interrupted and then reapplied, a standard multi-dynode PMT with quantum efficiency of 18% and gain of 10^5 may not be the optimum choice.

For the above reasons we have been investigating avalanche photodiodes (APD) as photo detectors - specifically the EG&G C30703F with a 10 mm $\times$ 10 mm solid state photocathode, and quantum efficiency of close to 75%. We have tested this device on prototype Shashlyk modules using cosmic ray muons, and found its performance to be stable and reproducible without the drawbacks mentioned above. In these tests we also superimposed light from an LED at up to 5 MHz on the signals from cosmic ray muons and found less than 2% reduction in the signal amplitude. While it has greater noise than a phototube, the increased quantum efficiency more than compensates giving an effective improvement in light yield of about a factor of two. When one includes the ancillary cost of phototubes, *e.g.*, high voltage distribution, tube base, and magnetic shielding, the cost of this APD is comparable to that of a tube.

While we have not yet tested the APD in a beam, our calculations, which have predicted performance reliably thus far, predict that the effective energy resolution of the Shashlyk module will be $3.0\%/\sqrt{E\,(\mathrm{GeV})}$, with improved stability. The predicted performance of this configuration is shown in Fig. 42.

5.2.4 Time resolution

Detailed time resolution studies of Shashlyk modules were performed by the PHENIX collaboration [2]. The results of those studies show that, for 1 GeV electrons, the time resolution for their modules was 100 psec and the light yield was 1200 photoelectrons. The experimental light yield for the prototype module described above was 4200 photoelectrons at 1 GeV, and the anticipated improvement on this, using an APD, is a factor 2. Since time resolution is inversely proportional to the square root of the light yield, we can anticipate a resolution of ~ 50 ps/$\sqrt{\mathrm{E(GeV)}}$ for the improved modules. The calorimeter and preradiator scintillators combine to form the time resolution of the photon detection system, and we anticipate the time resolution of the preradiator to be comparable to that of the calorimeter. Thus we anticipate a resolution on the order of 100 ps for 250 MeV photons - well satisfying the requirements of the experiment.

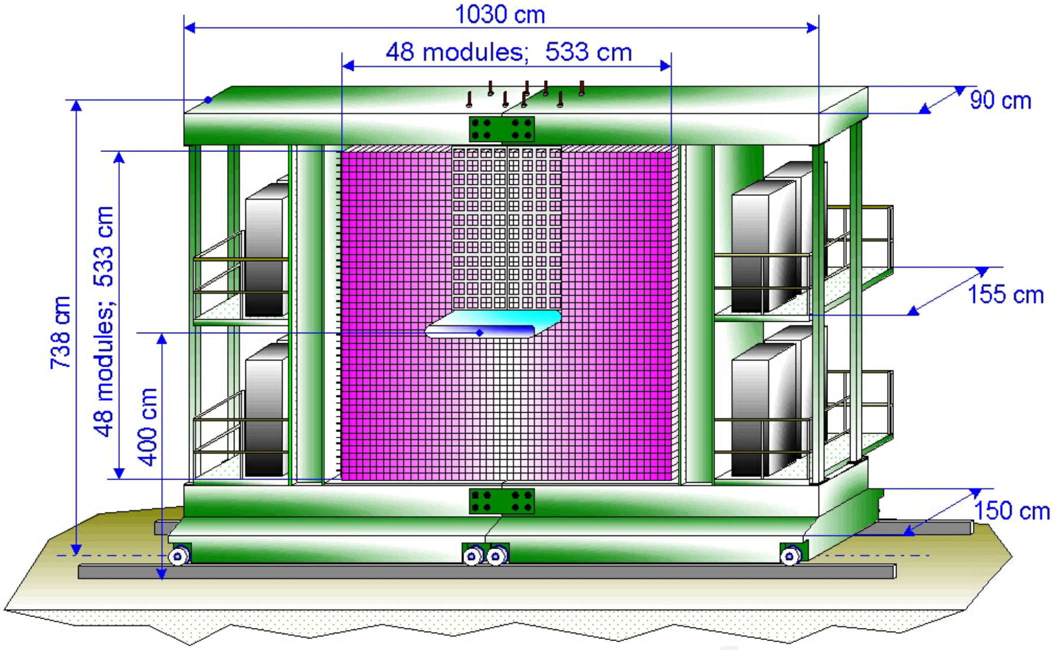

Fig. 43. Calorimeter structure in the closed position.

5.2.5 Calorimeter mounting

The calorimeter will be mounted in a support structure similar to that of the BNL E865 and HERA-B calorimeters (see Figure 43). Two requirements on the support structure beyond the simple necessity of structural strength and stability must be met. First, the rear of the calorimeter must be accessible for maintenance of the photodetectors. This requires that the halves of the calorimeter must be horizontally moveable to a point where the photodetectors are laterally displaced beyond the shield of the downstream sweeping magnet. Second, the modules directly over the beam pipe must be supported such that their weight is not on the pipe.

The calorimeter assembly is mounted on wheels which roll on railroad tracks. Figure 44 shows the calorimeter structure in its ‘open’ position. Two methods of holding the modules in place laterally are being considered. The first is to employ steel straps, about 100 μm thick, affixed to the vertical columns of the support structure and running around the modules in half a row, from the edge to the center of the calorimeter. This is the method used in HERA-B and thus is known to be viable.

The second method of supporting the modules laterally is to support the modules with Al plates, front and back, each of which cover half the calorimeter - from the edge to the center. Since the calorimeter is behind the preradiator, it is not expected to serve as a charged particle detector. Also, the thickness of the front Al plate can be less radiation lengths that a single Pb plate in a module. Thus this method of support does not compromise the performance of the calorimeter.

Supporting the modules over the beam pipe can be accomplished with steel straps from

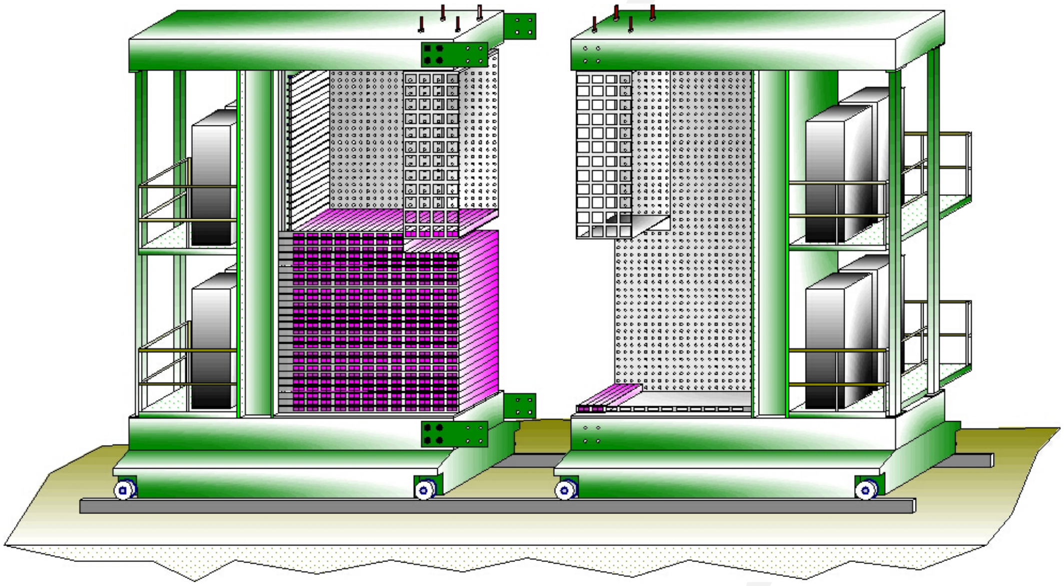

Fig. 44. Calorimeter structure in the open position.

above for the first (strap) method, and by the plates for the second.

5.2.6 Front-End Electronics

Introduction

Because of the pipelined nature of the preradiator chamber readout, the entire KOPIO readout system will be pipelined in a similar manner. This allows a simplicity and coordination of data flow that is economical both financially and in developmental resources. The calorimeter front end electronics (FEE) are schematically designed with this in mind and are described below. This design will be used for other photo-detector systems in KOPIO, *e.g.*, photon vetos and preradiator scintillators, thus the material below should serve as a description of the readout for those systems.

5.2.7 The calorimeter in the L0 trigger

The calorimeter will play an important role in the lowest level trigger, L0, by providing information such as the number of photon clusters, and the energies and times corresponding to these clusters. Monte-Carlo simulation shows that a photon (which already converted in preradiator) usually produces a clump which occupies 4×4 array of modules, and which often contains isolated hits. Thus, for trigger purposes only, the calorimeter will be divided by 4×4 logical units, and will effectively look like an array of 12×12 supermodules. As shown below, energies deposited in such supermodules and times associated with them can be digitized within a few micro-bunch cycles and be used in L0. This trigger scheme is similar to those in PHENIX and LHCb, and we plan to strongly rely on the knowledge gained in the development of those systems.

Table 4. Mechanical parameters of the calorimeter modules.

Item	***Dimension***
Lateral segmentation	110×110 mm^2
Polystyrene scintillator thickness	1.5 mm
Lead absorber thickness	0.275 mm
Reflective paper (TYVEK) thickness	0.05 mm $\times$ 2
Number of the absorber layers (paper/scintillator/paper/lead)	300
Number of WLS fibers	72
Length of WLS fiber/total length	1.5 m / 108 m
Fiber spacing	9.3 mm
Holes diameter in Scintillator/Lead	1.3 mm/1.4 mm
Diameter of WLS fiber (Y11-200-DC-S)	1.0 mm
Fiber bundle diameter	14.0 mm
Effective X_0	35.5 mm
Effective R_M	61.8 mm
Effective density	2.50 g/cm^3
Active depth	563 mm (15.9 X_0)
Total depth (without PMT)	670 mm
Total weight	18.0 kg

Table 5. Mechanical parameters of the full calorimeter.

Item	***Dimension***
Size of the active area	48×48 modules = 528×528 cm^2
Size of the beam hole	16×2 modules = 176×22 cm^2
Number of modules	2272
Number of modules above the beam pipe	184×2
Total height	738 cm
Total depth	155 cm
Depth of support frame	90 cm
Width of closed Calorimeter	$1,030$ cm
Width of open Calorimeter	$1,580$ cm
Distance between Calorimeter support rails	155 cm
Total weight of modules	18.0 kg $\times 2272$ = $40,896$ kg
Weight of modules above beam pipe	$(3,312 \times 2)$ kg
Total weight of support frame	$24,800$ kg
Total weight of Calorimeter	$65,696$ kg

5.2.8 Front End Electronics

The front-end electronics (FEE) of the calorimeter will process photodetector signals and provide energy, timing and trigger information to the experiment's data collection and trigger systems. For the calorimeter this electronics will be designed to measure energies with 12-bit dynamic range ($0.5 \div 2000$ MeV) and time of arrival with respect to the beam micro-bunch clock with a nominal resolution of 50 ps and an uncertainty less than 100 ps. Operation of the FEE will be completely pipelined with dead time no more than the duration of the input pulses. It will also be capable of forming and discriminating total energy signals and the total number of hits in the calorimeter.

Design requirements

Taking into account the performance requirements for energy and timing resolutions of the calorimeter and other detectors with PMT readout, we have chosen a single design with a 12-bit dynamic range for energy measurements and 10-bit dynamic range for time measurements.

The design of such a system should satisfy the following conditions:

- Shaping times of pulses less than 40 ns in order to avoid pile up between consecutive micro-bunches.
- Low-gain buffer amplifiers with adjustable gain (12 db) in order to compensate for gain variation of APDs operating with common HV.

- A fast integrator to limit the total tail noise after a 40 ns integration to less than one ADC count.
- A constant-fraction discriminator (CFD) and fast time-to-amplitude converter (TAC) for timing measurements with 50 ps time resolution.
- A fast flash ADC with a 12-bit dynamic range to cover an energy range of $0.5 \div 2000$ MeV.
- A fast flash ADC with 10-bit dynamic range has to cover a time range of $0. \div 50$ ns.
- Digitization of events at a 20 MHz rate, and storage in a 64-deep pipeline buffer, providing 3.2 μs latency.
- 8-bit energy and timing measurements for the L0 trigger logic.

Design of the FEE card

The design of our front-end electronics is based on the experience of the PHENIX[6] and LCHb projects[7,8]. A block diagram of the FEE is shown in Fig. 45.

Taking advantage of the fact that the Shashlyk APD (or PMT) calorimeter system is inherently fast, it has been decided to build a system capable of measurements every micro-bunch while avoiding pileup from signals associated with the preceding micro-bunch. The APD (or PMT) pulses therefore have to be shaped to eliminate pulse tails of more than 40 ns.

The APD pulse is shortened with a clipping line about two meters long (Fig. 45). The resistor-capacitor at the end of the line is adjusted to obtain a return to a zero-volt level after clipping, yielding a pulse about 20 ns (FWHM) in duration. The exact values of the parameters of this arrangement depend on the fall time of APD pulse and hence of WLS fiber used. The shaped pulses are then sent by coaxial cables to the front-end cards located in crates on the calorimeter stand. The front-end card contains 16 channels of amplitude and time conversion. This is a convenient number for the calorimeter since a calorimeter trigger element contains 16 modules (see above).

For analog conversion each FEE channel contains the following: a low-gain buffer amplifier; a fast integrator; a 12-bit 40 MHz ADC with adjustable strobe timing; a register to synchronize the ADC output; and a 1K 12-bit memory used as a look-up table for pedestal, gain and possible nonlinearity correction. A FPGA-2 (Field Programmable Gate Array) processor, in conjunction with a second 1K 8-bit memory will compute the 4×4-sum energy E_{sum} used in the L0 trigger. Since the high voltage will be applied in common, the gain of the low-gain buffer amplifier will be adjustible to compensate for photodetector channel-to-channel variations. The fast integrator will be discharged by subtraction of the input pulse in a buffer amplifier after a 40 ns delay[9].

For timing each FEE channel contains a CF discriminator with adjustable fraction threshold, a fast time-amplitude converter (TAC) with a 40 ns time window[10], a 10-bit 40 MHz ADC, register to synchronize the ADC output, a 1K 10-bit look-up memory for ‘zero’-time correction and possible nonlinearity in the time scale. A FPGA-2 processor with a 1K 8-bit memory will determine a mean time, T_{mean}, for shower clusters, to be used in the L0 trigger.

Digitized amplitude and time signals from the calorimeter will be transmitted to store in the L0 pipeline buffer during the L0 latency. Data belonging to an accepted L0 trigger will be extracted from the L0 pipeline and passed to the L0 derandomizer buffer awaiting transfer to the level 1, L1, trigger. The pipeline buffer and derandomizer will be implemented as one FPGA-3 for all 16 channels. The E_{sum} and T_{mean} data, participating in the L0 trigger will be sent to L0 the trigger FPGA via a ($400 \div 600$)MHz serial link.

Digitization of the calorimeter analog signals will occupy one to two micro-bunch cycles, correction of times and subtraction pedestals will take one cycle, transfering digitized data in the L0 pipeline and preparation of the E_{sum} and T_{mean} data for the L0 trigger will require additional cycles. Thus, the total set of E_{sum} and T_{mean} data from the entire calorimeter will be computed and sent to the FPGA module of the L0 trigger in $150 \div 200$ ns. It will be transmitted by 144 channels of fast serial link. In the L0 module the number of clusters, total cluster energy and average timing of each cluster will be computed. The mean position of clusters can then be compared with predicted positions from the preradiator scintillators. This information, along with data from veto detectors will then be used the as the basis of the L0 trigger. The expected time for data processing and decision making in the L0 FPGA module is three micro-bunch cycles or 150 ns.

The analog piece of the FEE - amplifier, the discriminator, the TAC and the integrator will be manufactured as a custom ASIC, as in LHCb. The remaining electronics will be constructed from commercial components: 12-bit and 10-bit 40 MHz ADCs (for example AD9042), 8-bit and 4-bit 40 MHz memories, and 472-input FPGAs. The latter will be used as processors, memories and for the organization of the pipeline buffers.

5.2.9 Calibration and Monitoring

Introduction.

To achieve the desired energy resolution of the KOPIO calorimeter, $\sim 3.0\%/\sqrt{E}$, an appropriate monitoring and calibration system must be developed. We describe below our current ideas about such a system.

Calibration, pre-calibration and monitoring

The ultimate calibration will be done *in situ* using π^0 decays from background and specially triggered events acquired during the experiment. The advantage of such calibration is that it is carried out under the same conditions, and using the same methods as those for the studied process. This also allows the preradiator and calorimeter to be calibrated both separately, and as a single entity using the same events. The drawback of such a process is that it requires a relatively long period of data accumulation to achieve a sufficient number of calibration events. Thus, two supplemental systems are required: one to pre-calibrate the calorimeter with accuracy a few percent, and another to monitor its performance and restrict the variation of the photo-detector gains to the order of 0.4%.

We will use cosmic ray muons for pre-calibration, as was done in experiment E865[11]. This pre-calibration is based on the assumption that the mean value of signals from cosmic ray muons vertically transversing Shashlyk modules is approximately the same for all modules. E865 was able to pre-calibrate its 600 modules with accuracy 4% in one hour, even from a “cold start”. Cosmic ray muon calibration also provided long term monitoring of the photodetector gains with accuracy $1 \div 2\%$.

This technique simply requires a special trigger that recognises cosmic muons vertically penetrating the entire calorimeter. Such a trigger can be formed from a coincidence between the top and bottom horizontal layers of modules, gated between AGS pulses.

The monitoring system described below will also serve as a pre-calibration of the module readout chain at the 10% level.

Design of the monitoring system

The monitoring system employs light flashers, and must satisfy a number of specific requirements:

- High long-term and short-term temperature stability - better than 0.1%;
- Short light pulse duration - less than 50 nsec;
- Small variation in the flash amplitude - less than 0.2 %;
- A large number of photons in the light pulse - more than 10,000 photons/channel;
- Variable pulse repetition rate and intensity.

These equirements can be met with Light Emitting Diodes with a brightness of 5 - 10 standard candels that have recently been developed (*‘ultra bright LED lamps’*),(see Table 6).

LED	Photons/pulse ($\times 10^6$) (8ns driving pulse)	Photons/pulse ($\times 10^6$) (60ns driving pulse)
STANLEY ESBR 5501 RED	55	700
STANLEY SUPERBRIGHT RED	250	4,000
HP HLMT-CL00 YELLOW	120	2,000
HP HLMP 8505 GREEN	2.8	28
NICHIA NLPB-500 BLUE	45	500

Table 6. Light intensity parameters of some commercial LED lamps.

The monitoring system is based on an electronic method of stabilization of the LED light output by means of optical feedback provided by a PIN photodiode[12,13]. The PIN diode monitors the LED light output, and a feedback loop employs this signal to adjust the driving pulse amplitude of the LED. As it is shown in references[12] and[13] the PIN diode has a temperature coefficient $\sim 4 \times 10^{-4}/^oC$, with a long-term stability of better than 10^{-4}. As result, the monitoring system described in[12] shows a long-term stability better than 0.1%.

The block-diagram of the LED monitoring system is shown in Fig. 46. The input “start” pulse triggers a stable pulse generator based on the ECL elements and an external passive delay line (for stabilization of the pulse duration). The signal of specified duration is amplified in a linear mode and applied to a power transistor (pulse current $\sim 2A$), loaded on the LED. Part of the light ($20 \div 30\%$) from the LED is split off by a special optical beamsplitter and sent through an optical collector to the input of the thermo-stabilized unit for providing an optical feedback. A Hamamatsu S3590-03 PIN diode will be use as the photoreseiver of the feedback channel. The signal from this diode will be amplified by a charge-sensitive amplifier and sent to a comparator for comparison with the reference U_{REF} level. The output signal from the comparator, which is proportional to the difference of the tested and reference level, including sign, is sent to *”LED current control block”*. This block will correct the amplitude of the LED drive pulse to stabilize the PIN diode signals, *i.e.* the light signals on Shashlyk modules.

The signal from Pin diode is also sent to QDC for control measurements.

The design of such driving and quenching units is well known[12,13]. We have tested the first prototypes of these units, and test measurements of the first 32 - channel prototype of the monitoring system are planned for late 2001.

The monitoring system will service 64 Shashlyk modules. The light monitoring signals will be delivered via 1.0 mm diameter clear optical fibers to the front of each calorimeter module. The light will then be transmitted from the transport fiber to another clear fiber that penetrates each module at the cell center.

Thirty six units are required to service the entire calorimeter. They will be located on each side of the calorimeter support structure close to their respective modules.

From analysis of existing monitoring systems and our preliminary test measurements of small prototypes, we conclude that this type of monitoring system will have long-term and short-term stability that meets our 0.1% requirement.

5.2.10 Summary

Modules for a Shashlyk calorimeter with energy resolution about $3.3\%/\sqrt{E}$ have been constructed and experimentally tested. Monte-Carlo simulation based on this experimental data indicates that this resolution can be improved to about $3.0\%/\sqrt{E}$ with a time resolution better than 100 ps/$\sqrt{E}$. These realizable parameters meet the design goals of the experiment.

The readout has been modeled on existing systems and fits well in the overall KOPIO readout scheme. The readout technique used for the calorimeter will be used for other photodetector systems in the apparatus. Monitoring and calibration systems have also been designed based on existing technology. It will meet the required precision and stability necessary to maintain the energy resolution of the calorimeter,

The mechanical issues in mounting a large calorimeter have been addressed and solved in existing detectors. This also gives us confidence in our cost and manpower requirement estimates.

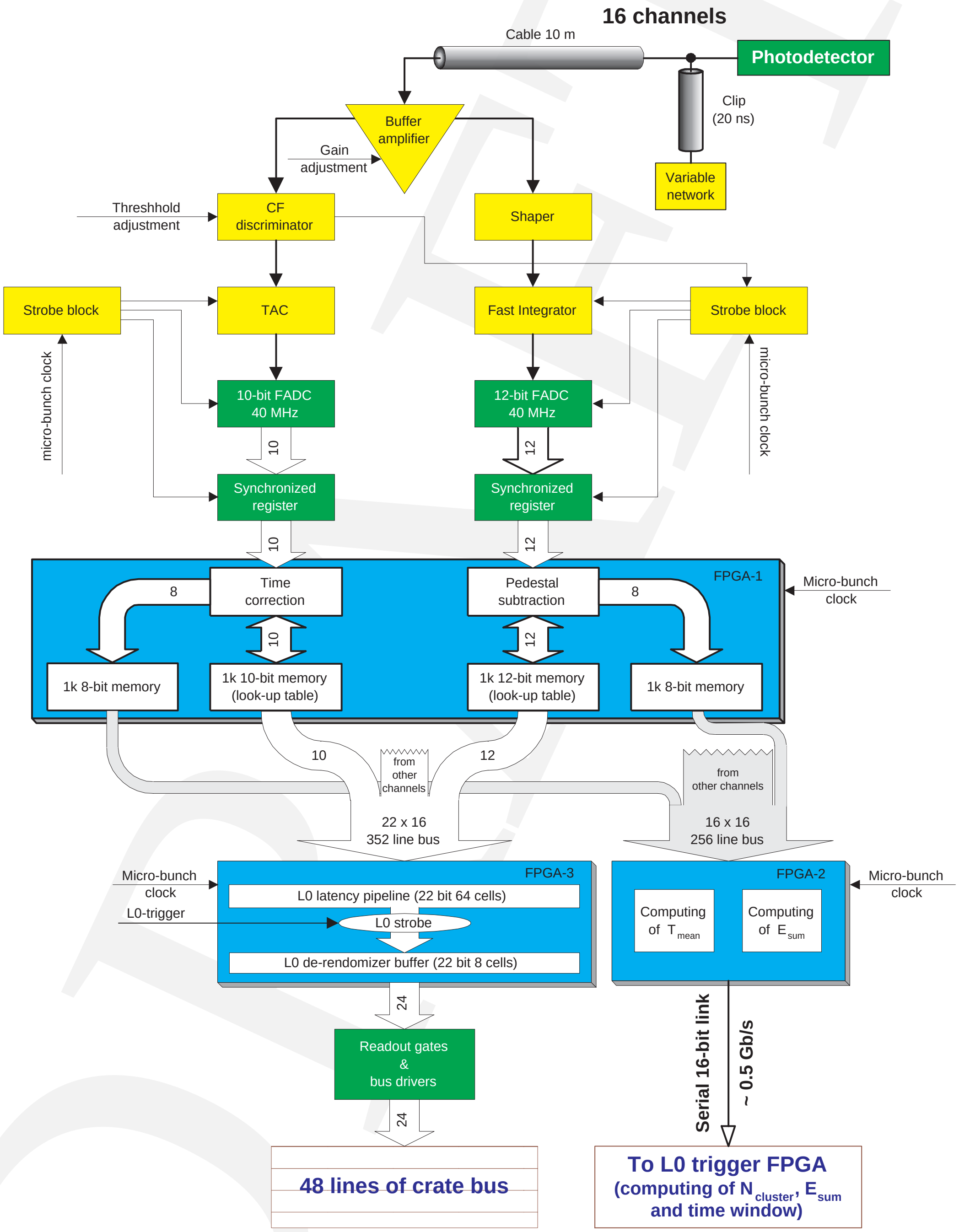

Fig. 45. Schematics of custom designed Calorimeter Front-End Electronics card.

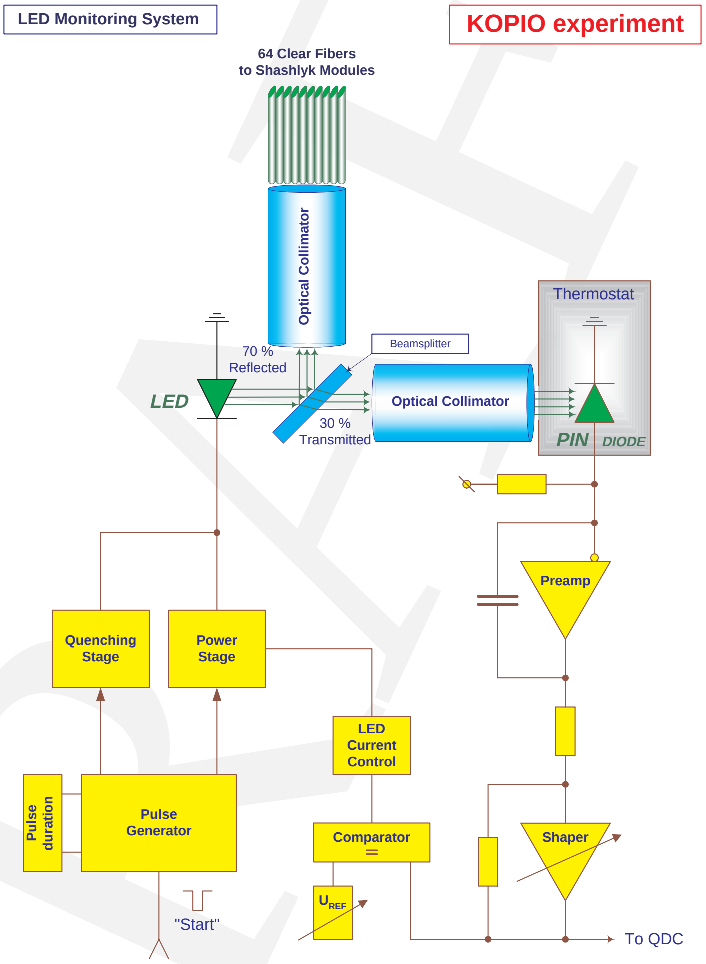

Fig. 46. LED Monitoring System of the Calorimeter.

5.3 Charged Particle Veto

Requirements and strategy

The purpose of the charge-particle veto system is the efficient identification of background processes in which an apparent $\pi^0 \to 2\gamma$ decay inside the decay volume is accompanied by charged particle emission. Examples of such background processes are:

- $K_L \to \pi^+\pi^-\pi^0 \;\; (K_{\pi 3})$
- $K_L \to e^+\pi^-\nu\gamma \;\; (K_{e3\gamma})$
  $\hookrightarrow \gamma$
  in which the positron creates a second photon through Bremsstrahlung or annihilation in flight.
- $K_L \to e^+\pi^-\nu \;\; (K_{e3})$
  $| \quad \hookrightarrow \pi^0$
  $\hookrightarrow \gamma$
  again followed by $e^+ \to \gamma$ whereas the π^- creates a photon through $\pi^- p \to \pi^0 n$.

In all of the above cases two particles with opposite electrical charge emerge, and the corresponding $\gamma\gamma$ kinematic distribution differs significantly from the $K_L \to \pi^0\nu\overline{\nu}$ distribution. In all cases the events may also produce signals in other detector elements, such as the photon veto or the preradiator/calorimeter systems. Still, detection efficiencies of 99.99% or better are required to keep these backgrounds below a few events in the final sample.

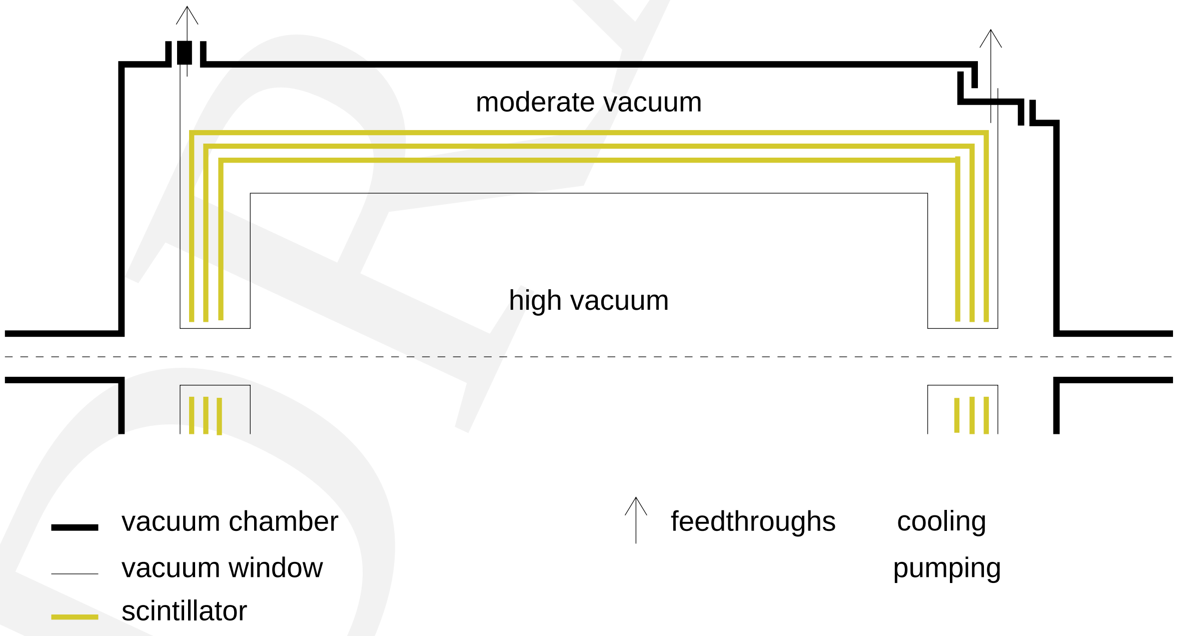

Fig. 47. Schematic view of the charged particle veto system.

Figure 47 illustrates the proposed scheme for the charged particle veto system in the region of the decay volume. We plan three layers of plastic scintillator each with an intrinsic detection efficiency better than 99%. The scintillators, 1.5 mm thick for the inner two layers and 5mm thick for the outer, are read out by embedded 1mm diameter wavelength shifting fibers spaced about 5 mm apart. In figure 48 we show the light output of this type of configuration as a function of fiber spacing, for different configurations. These curves are from an optical Monte Carlo simulation developed for Shashlyk simulation calculations using known properties of all components as the only inputs. Also shown in the figure is a data point from a measurement made at the BNL AGS. Seeing the agreement between the measurements and calculation gives us confidence in our extrapolations. For our calculations of veto efficiencies we use 10 photoelectrons for minimum ionizing particles in the thin counters and 60 photoelectrons in the thick.

The detectors will be separated from the high-quality beam vacuum by a thin metallic foil. The whole assembly including vacuum foil will be mounted inside the central part of the vacuum chamber. This geometry allows the entire veto system to be checked out and installed (or removed) as a single unit. All connections to the outside world (fibers and vacuum pumpouts) will be through two flanges situated at either side of the central tube. The vacuum in the detector region will be maintained at $\sim 10^{-3}$ Torr.

This configuration is made with several factors in mind:

- *Maximum practicable solid angle for charged particles from K decays* - The design covers the entire solid angle with the exception of the areas where the beam enters and leaves the decay volume. These latter regions will be covered by other detectors.

- *Sensitivity to low energy negative pions and positrons* - Losses of these particles at the low energy end of the decay spectrum are proportional to the amount of material that must be penetrated before sufficient scintillation light has been created. The first material is the thin foil separating the two vacuum regions. It is planned that this foil is made of 5 μm of Ti ($< 0.02\%$ of a radiation length, $< 2 \times 10^{-5}$ of an interaction length).

  The next material in which the charged particles can interact and disappear is the scintillator itself. For instance, π^- mesons have a significant cross sections for reactions such as $\pi^- p \rightarrow \pi^0 n$, $\pi^- p \rightarrow \gamma n$ and $A(\pi^-, 2n)A^*$. In the energy range 50-300 MeV the charge exchange cross-section on CH varies between 30 and 230 mb[1], corresponding to an interaction probability between 0.015 % and 0.111 % per mm of scintillator. The quasi-deuteron cross-section for π^- absorption on carbon varies between 20 and 60 mb[2], equivalent to 0.01-0.03 % interaction probability per mm. Thus it is the quasi-deuteron process which will ultimately limit the detection inefficiency of π^- to about 10^{-4}.

  For those interactions where there is a secondary photon emitted, the roughly 4π coverage by the surrounding photon veto will multiply the charged particle veto inefficiency by the photon detection inefficiency - conservatively a factor of 0.1.

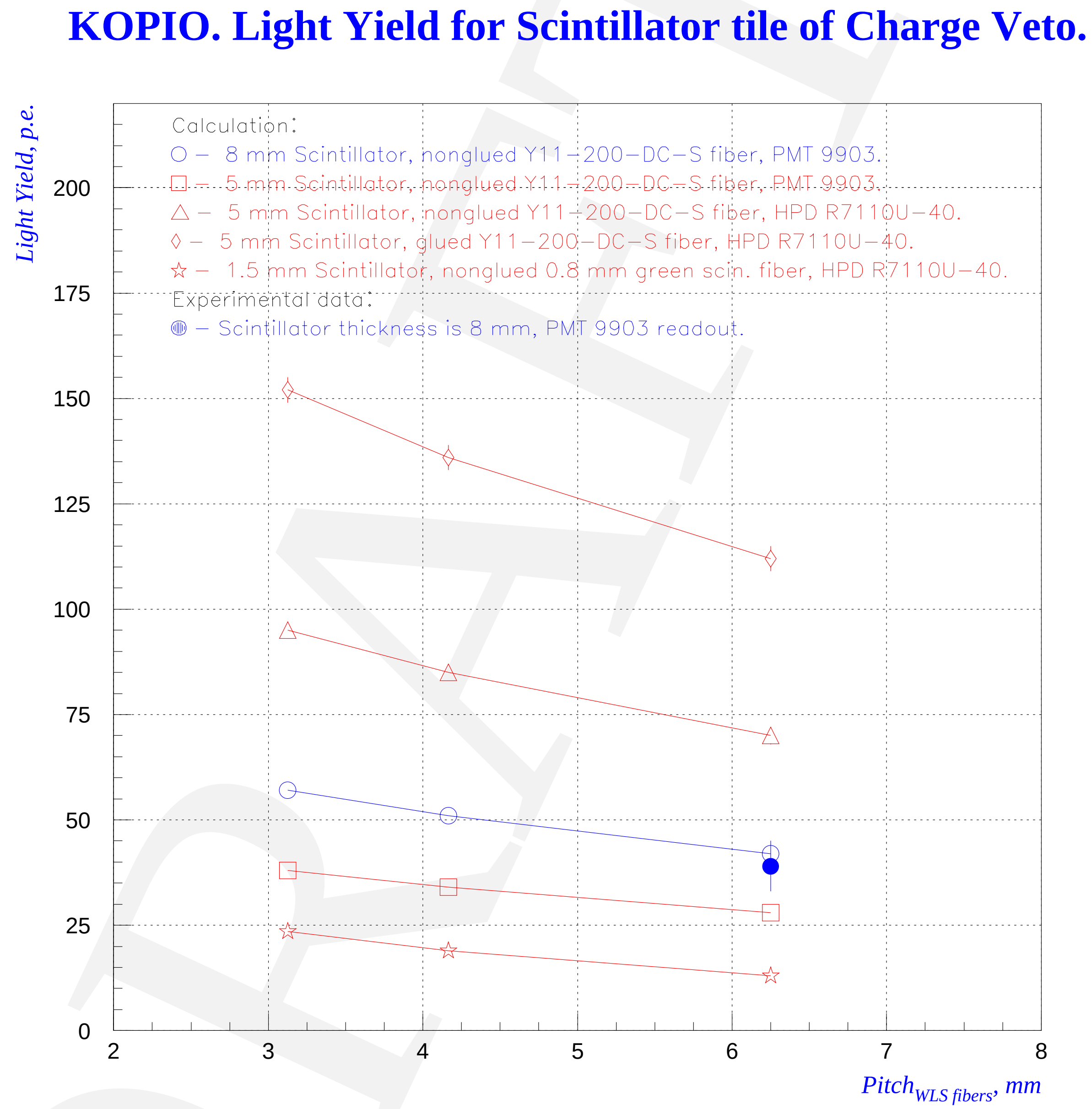

Fig. 48. Light output from several configurations of fiber embedded scintillator.

Positrons may annihilate in flight through interactions with the electrons in the scintillator material ($e^+e^- \to 2\gamma$). This cross is proportional to $1/E_{e+}$. In calculating our inefficiencies for this process we have relied on measurements of Inagaki[3] taken at $E_{e+} = 1$ GeV - adjusting for counter thickness and threshold we characterize the inefficiency as $0.05/$E(MeV).

In order to achieve our quoted efficiency all particles should be detectable having passed through less than 3 mm of scintillator.

- *Small dead time effects in the readout chain due to multiple hits.* - One source of such losses result from double-pulse resolution of the system. The vast majority of counts in the charged particle veto result from K decays - roughly 10 MHZ. Since we accept only one decay per micro-pulse, and 98% of the decays in the preceding pulse occur more than 10 ns before the decays in the micro-pulse of interest, the inefficiency due to this double pulse blinding is roughly 2×10^{-5} per detector element, or a few times 10^{-3} for the charged particle veto system. This too can be eliminated since we will waveform digitize the charged particle veto and know if there was a pulse in the region of interest in the preceding 10 ns. If we reject all events where this occurs we will negate this inefficiency at a cost of about 2% of our events - an “accidental” loss.

- *Insensitivity to random pulses from ambient background.*

  Sources of such background are random neutrons and photons interacting in the counters and producing sufficient light. To calculate rates of these we use E787’s experience. That experiment sat at roughly the same angle to the production target as KOPIO and had roughly the same depth of shielding material between the target and the detector (although the material was half steel and was not designed to suppress neutrons). The experiment had a barrel veto counter of scintillator and lead which had across sectional area of 3.7×10^4 cm^2 for its upstream surface. Its total count rate was about 2.5 MHz for 10^{13} Hz of protons on a one interaction length target with a threshold of about 200 keV. If we take that rate to be totally due to neutrons, the rate of neutrons was about 10^{-11} neutrons/proton/cm^2.

  The KOPIO upstream wall of the charged particle detector is 4×10^4 cm^2. For 3×10^{13} Hz of protons on our target we expect about 10^7 Hz of neutrons incident on the upstream wall.

The scheme we propose is to employ the three layers in a ‘2 out of 3, plus 500 keV in the thick counter’ mode ($2 \div 3$). By this we mean a coincidence between two out of three counters, or a single count in the thick counter corresponding to more than 500 keV of energy deposited. From Fig. 48 we expect more than 10 photoelectrons for a minimum ionizing particle passing through the thin (1.5 mm) inner layers. We will set a threshold of 3 photoelectrons on these layers, resulting in an efficiency of $\sim 99\%$ for minimum ionizing particles. The probability of particles not penetrating the entire 3 mm of the two layers is on the order of a few times 10^{-4}. In the $2 \div 3$ mode the low energy pions and positrons which only penetrate three mm of scintillator will have a 98% efficiency for detection. Penetrating less results in a lower efficiency, but the joint probability of these low energy particles from K decays and a lack of detection remains at the 10^{-4} level. For particles that penetrate into the thick counter, the $2 \div 3$ yields an efficiency of $\sim 10^{-4}$ since the thick counter with a 3 photoelectron threshold is expected to be $> 99.99\%$ efficient. We add to that the efficiency of observing more than 500 keV of energy in the thick counter. Since this counter has a nominal 1 MeV of energy deposited and has a light yield of 60 photoelectrons, a 500 keV threshold is 30 photoelectrons, or four standard deviations. This should give a veto inefficiency of less than 10^{-5} without being overly sensitive to ambient background. The high threshold determination will be done off-line.

The issue of accidental vetoes from K decays has been discussed above. Those from 'wrap around' decays, where a K decay occurs in the micro-pulse after the micro-pulse in which it was produced due to the low momentum of the kaon, are accounted for in our sensitivity calculations.

The very low energy neutrons, $\mathrm{E_n} <$ a few MeV, will not produce a coincidence. The probability of interacting in the thick counter and producing sufficient light to exceed the 500 keV threshold is at a few % level according to GEANT+GCALOR calculation, or a rate of $\sim 3 \times 10^5$ Hz. Taking a 10 ns time window for accidental coincidences says that we will have a few times 10^{-3} accidental veto probability due to neutrons in the front wall of the charged particle veto system - or a few percent for the entire detector.

The charged veto counters may produce background themselves. Of major concern, for example, would be π^0's produced by high energy neutrons interacting in the counters. For this reason the veto counters are placed well away from the beam region. Should a π^0 be produced in this way, our ability to locate the vertex of the photons from the π^0 would allow us to recognize that the event did not originate from the decay region.

In summary, in our Monte Carlo calculations we have used a detection inefficiency of 0.05/E(Mev) for positrons, $1.5 \times (10^{-4} + 10^{-2}/\max(200., P))$ for π^- (where P is the pion momentum), and 10^{-5} for π^+, and 10^{-4} for e^-. These inefficiencies are achievable with this scheme, and comparable to published measurements [3].

Conceptual design

The present design (see Fig. 49) has mirror symmetry in all three space coordinates. The barrel part of the detector is composed of 3 layers of 12 panels, 47 cm wide, running parallel to the cylinder axis, with their fibers running in the direction along the circumference of the detector - the ϕ direction. The length of fiber embedded in scintillator, ı.e., the active length, is 47 cm long. These fibers are read out from one end. The 47 cm length results in a time jitter of $\approx \pm 1.5$ ns. The end caps consist of three layers of scintillator with their fibers running horizontally and read out from each end. Table 7 summarizes these parameters.

The fibers are read out by Hybrid Photo Diodes (HPDs DEP model PP0380AJ) located on the circumference of the flanges at the ends of the barrel. These are very fast devices with good photon counting capability. They are segmented cathode devices with 73 pixels (2mm hexagon) they will be subdivided into 7 with 50 fibers per seventh (350 fibers/tube).

The thin scintillators will be made from a Bicron plastic scintillator casting resin (BC-

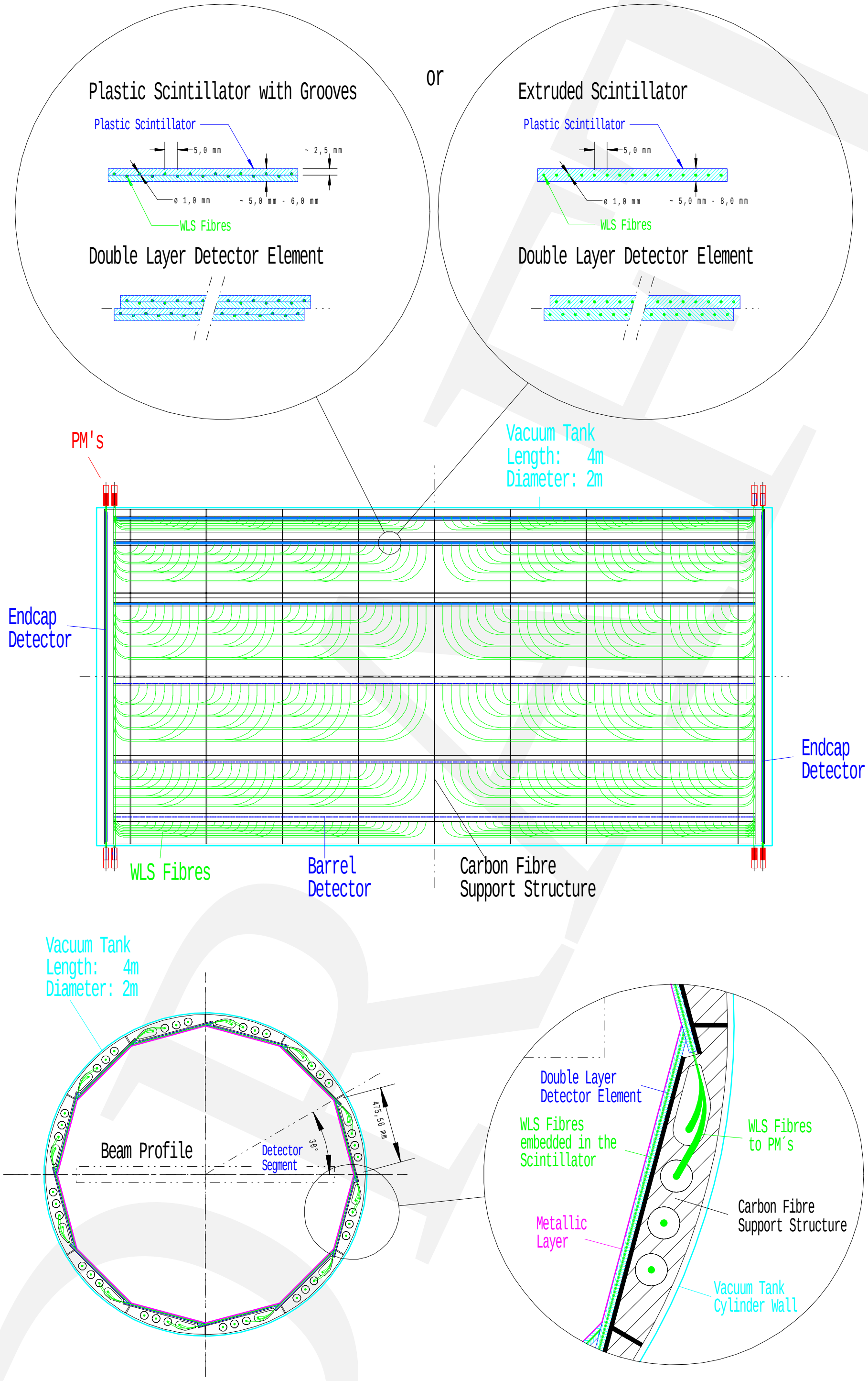

Fig. 49. Conceptual design of the charged particle veto system.

490) This is a partially polymerized plastic scintillator that is cured to full hardness by the user. The scintillator thus formed is clear with scintillation and mechanical properties similar to those of Bicron's general purpose plastic scintillators. It is most frequently used in applications which require other materials (fibers) to be embedded in the scintillator and which require the casting of unique shapes.

The wave shifting fibers will be similar to BCF-20, a fast green scintillator fiber with a light absorption spectrum in the blue. The absorption and emission spectra for BCF-20, and the emission spectrum for polystyrene scintillator are shown in Fig. 50. A fiber such as this acts as a wavelength shifter for the blue light emitted in the surrounding scintillator, and scintillates when ionizing particles pass through the fiber. BCF-20 has an emission peak at 492 nm with a decay time of 2.7 ns, and emits ~ 8000 photons per MeV of ionizing energy deposited.

Our R&D program includes optimization of the mixture of fluorescent dopants in this scintillator/fiber system to yield the maximum light output.

Table 7. main parameters of the charged particle veto system with WLS readout.

	barrel	endcaps
Number of segments	12 (ϕ)	2×2
Orientation of WLS grooves	$\perp$ z-axis	horizontal
Active WLS fiber length	47 cm	43-195 cm
Number of fibers	~ 28800	1600
Light extraction	single end	both ends
Number of detector channels	~ 600	80
Number of HPDs	85	16

R&D program

We have constructed a detector system at PSI to evaluate scintillator configurations in a test beam at PSI. This R&D program is proceeding in two steps. First we will study the detection efficiency of generic scintillators for e^+, e^-, π^+ and π^- at various momenta. Preliminary tests have already been performed (see[4]). It is our intention not only to measure the efficiency of the plastic scintillator system, but to identify the main sources of inefficiency for the various particle species as well. This way it should be possible to reproduce the results by simulation, and improve detection efficiencies.

In a second step various prototype modules will be compared. We intend to study the following options:

- light readout through WLS fibers as shown in Fig. 49,
- light readout through short light guides inside the vacuum chamber, and

- planes with bent scintillating fibers which fit the shape of the vacuum chamber.

We will also study the susceptibility of these counters to neutrons, and the reliability of our trigger concept.

Installation

Installation of the system is shown in Fig. 51. The photodetectors are located on the circumferences of the feed through flanges. Thus, there are no active elements inside the vessel itself, and it is not anticipated that access to the scintillators would be necessary. Disassembly, should it be necessary, would be the reverse of the process shown.

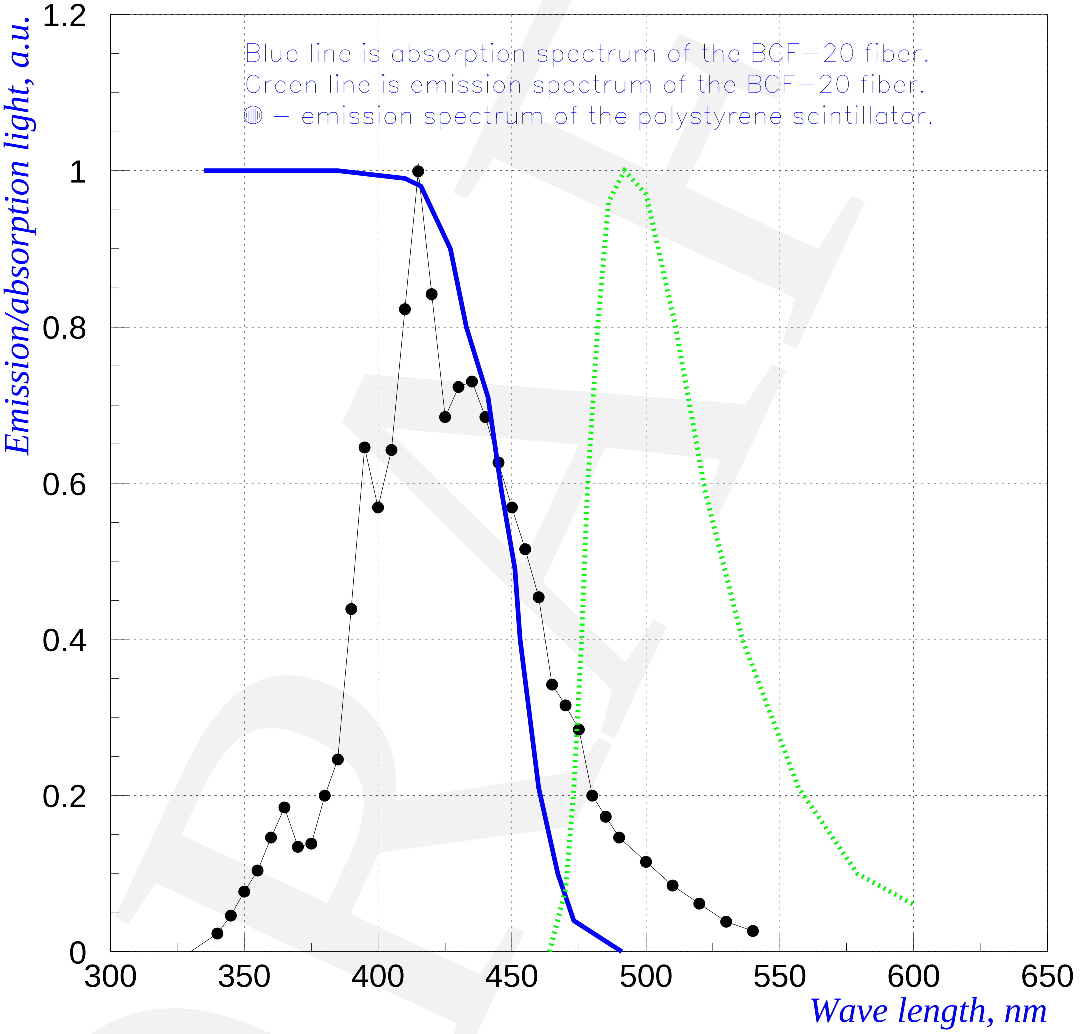

Fig. 50. Absorption spectrum of BCF-20 (blue, solid line), and emission spectra of BCF-20 (green, dashed line) and polystyrene scintillator (dots).

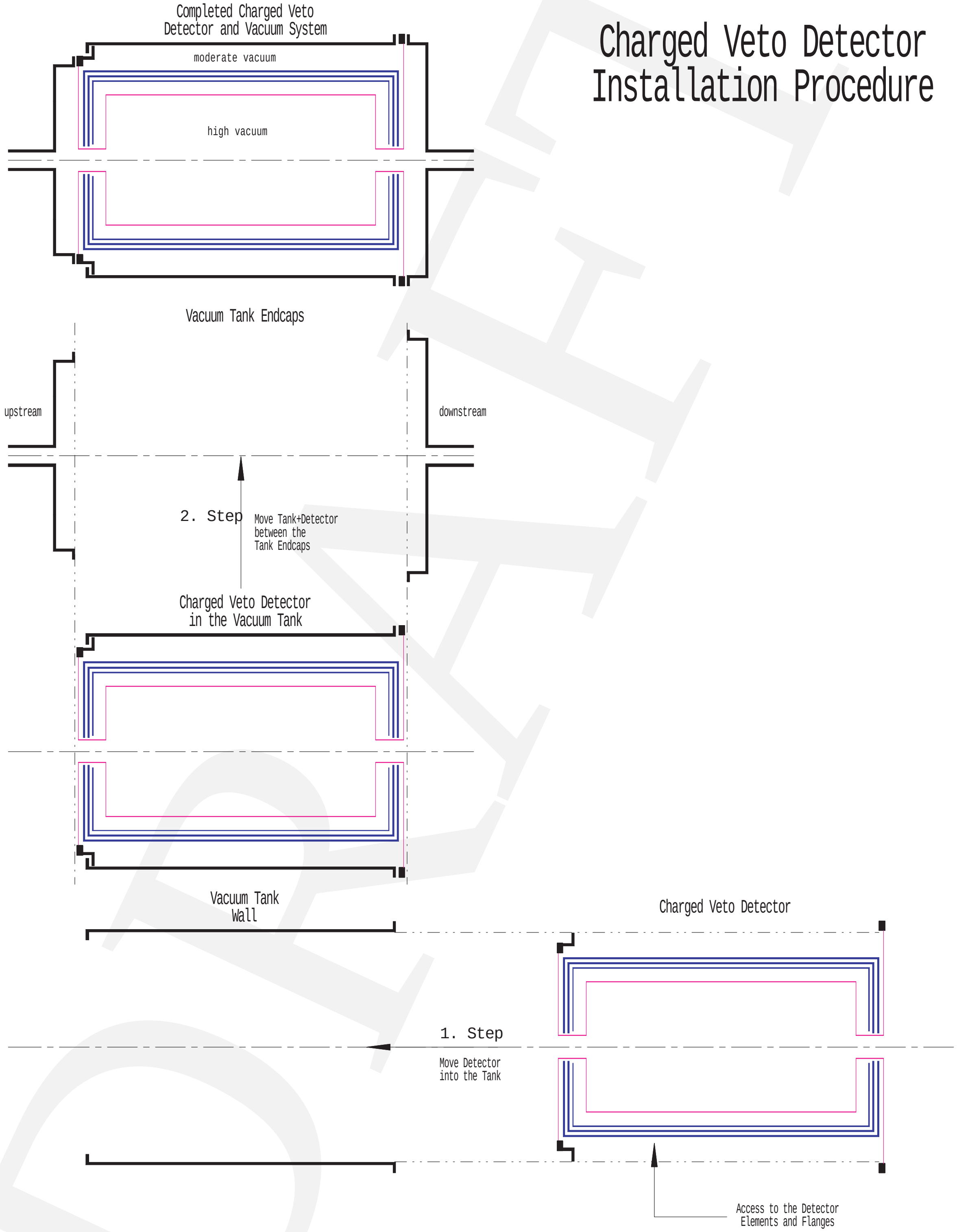

Fig. 51. Installation procedure.

5.4 Barrel Photon Veto

Introduction

A principal concern in the measurement of $K_L \rightarrow \pi^0\nu\bar{\nu}$ is rejection of background. One of the most important backgrounds can appear when two photons from $K_{\pi 2}$ decay are missed. Full kinematic reconstruction of the π^0 allows suppression of background but a high degree of photon detection efficiency, better than 0.9998 per photon is required. A veto system must have good space and time resolutions while covering a large solid angle around the 4 m long kaon decay region.[‡]

Lead/plastic scintillator sandwich veto counters have been chosen for the barrel veto detector which will have thickness of about 18 X_0 (radiation lengths). The barrel veto features high light output and radial readout segmentation. To read light from the scintillators, an embedded wavelength shifting fiber readout technique will be used. Wavelength shifting (WLS) optical fibers are placed in the grooves which run along 4 m plastic scintillator slabs with spacing of 6–10 mm. The large volume of plastic scintillator ($\sim$50 t), required for coverage of a very large solid angle will be made of polystyrene based extruded scintillator.

Design of the barrel veto detector

*

Sandwich design issues

The barrel veto detector in KOPIO will consist of layers of 7 mm plastic scintillator slabs of 4-5 m length interleaved by lead foil of 0.5-1 mm thickness. Figure 52 shows features of the energy response in such an arrangement. A schematic view of a sandwich element (module) is shown in Fig. 53. The whole barrel veto detector (see Fig. 54) will be built of modules consisting of 13–17 scintillator slabs and lead layers, which are bound together by a thin stainless steel container. The WLS fiber readout technique provides uniform light collection over the area of the scintillator since the light attenuation length of the WLS fibers is longer than that of a scintillator. Fiber flexibility eliminates the need for a complicated system of lightguides that could pose a serious problem for the veto coverage. One PMT views a bundle of up to 210 WLS fibers from each end of a module.

The total number of lead–plastic layers depends on the thickness of the lead foil. 100 layers of 1 mm foil provides 18 radiation lengths. Using 0.5 mm thick lead will increase the number of layers. The energy resolution is determined primarily by fluctuations in the fraction of the shower energy absorbed in the active layers (sampling fluctuations). A fine sampling structure (large number of layers, thin converter) would provide a higher light yield and better energy, time and space resolutions. However, the cost of the system will be also higher.

A lead thickness of 0.5–1.5 mm has been used in several experiments[2–4]. For most of the barrel veto detector the absorber will be 1 mm lead foil as a compromise between acceptable veto resolution and reasonable segmentation.

[‡] Moreover, the barrel veto detector is considered for possible use as a calorimeter to allow an increase in the acceptance. See Appendix A.

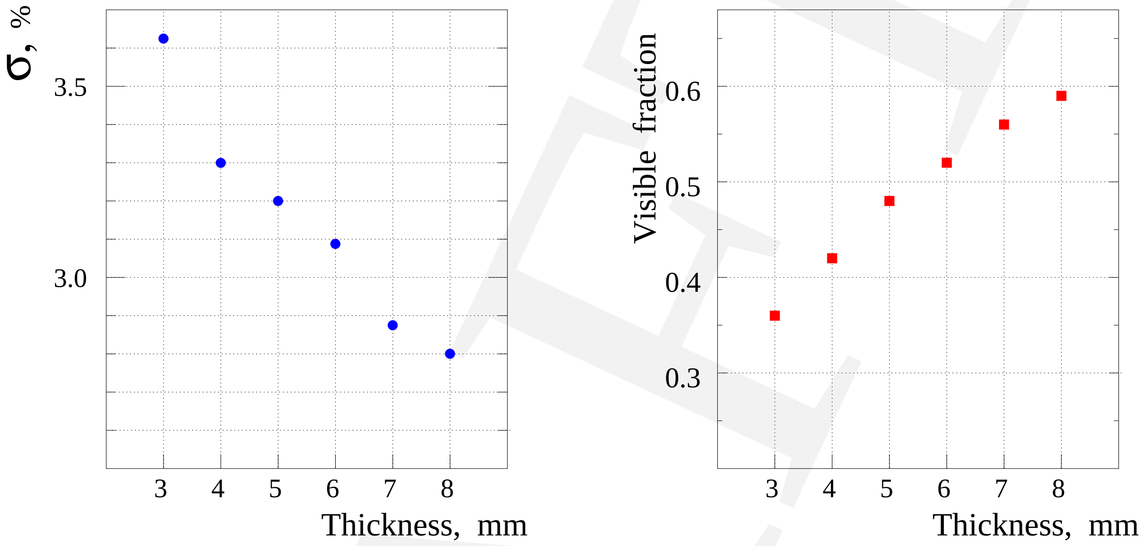

Fig. 52. The energy resolution ($\sigma/\sqrt{E}$) and visible fraction versus the thickness of a scintillator layer in the case of 0.5 mm lead. The resolution is determined by sampling and leakage fluctuations. The number of layers is 180.

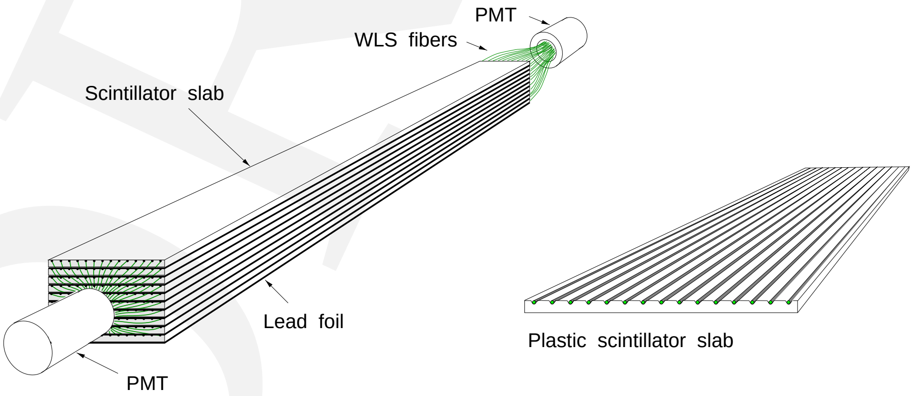

Fig. 53. Schematic view of a veto sandwich module.

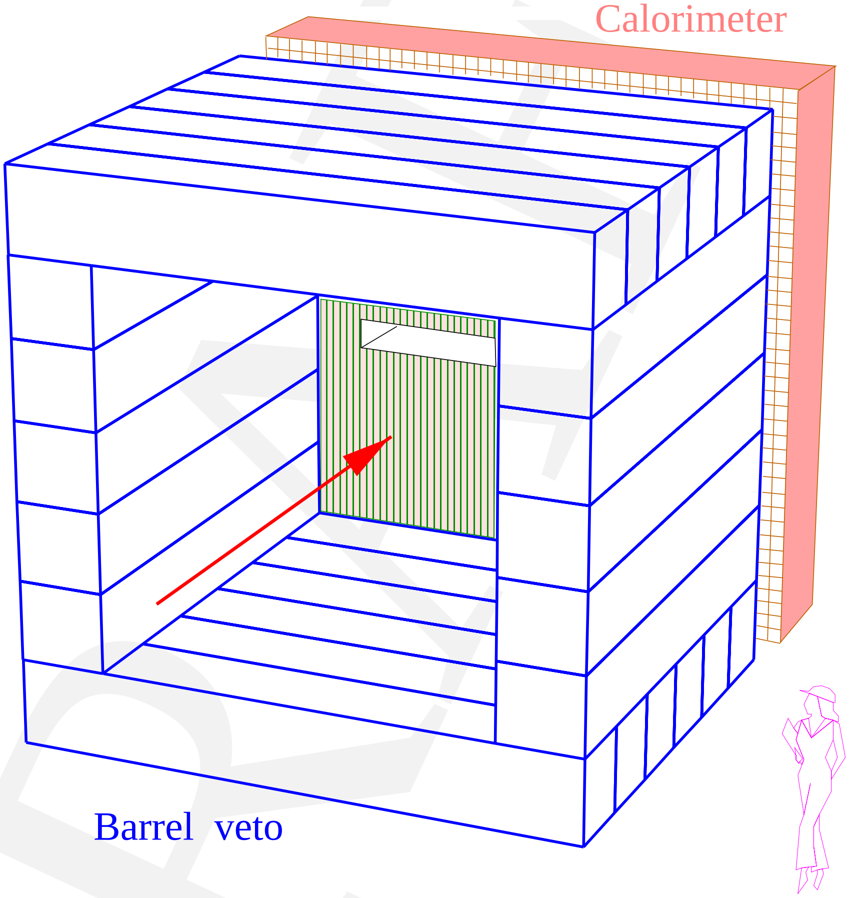

Fig. 54. View of the veto barrel assembled with about 750 modules. The inner size of the veto is $3.5 \times 3.5\ \mathrm{m}^2$, and its length is 4.2 m.

An approximate formula for the resolution of a typical scintillator–Pb sampling calorimeter was published in Ref.[5]:

$$\sigma[\%] = \frac{14.5}{\sqrt{E_\gamma[GeV]}} \sqrt{\frac{t}{X_0}} \cdot \sqrt{1 + 0.57/n}, \tag{5}$$

where **t** is the thickness of the lead plates, X_0 is the radiation length of lead and **n** is the number of photoelectrons per minimum ionizing particle in a single scintillator sample. Therefore, for $\mathbf{n} > 5$ the photostatistics do not degrade the energy resolution, which is dominated by sampling fluctuations. It is interesting to note the σ does not depend on the scintillator thickness, (from empirical approximations of data obtained with operating sampling calorimeters). Actually the thicker scintillator increases the visible fraction that improves the energy resolution.

With 1 mm lead foil we expect (from the formula) to obtain resolution not worse than $\sigma = 6.1\%/\sqrt{E}$, although the pure sampling fluctuations simulated by GEANT contribute only $\sigma = 4.3\%$. The sampling depends on the lead/scintillator segmentation as well as the angle at which the photon hits the sandwich. In this sense the angular resolution is vital to obtain the good energy resolution.

While the light yield of a single active layer (a scintillator slab) does not affect the energy resolution above some minimum photostatistics, the light output is very critical for detection of low–energy photons with the required efficiency. To increase the visible fraction of shower energy we will make the first $3X_0$ of the veto detector with thin lead foil of 0.5 mm providing higher light output for low energy photons.

Another important consideration for achieving high light output is the requirement of time resolution better than 70 ps/$\sqrt{E_\gamma[\mathrm{GeV}]}$. Precise timing allows us to suppress the accidental hits and background events. The WLS fiber readout gives better time resolution compared with a readout by light guides for the same number of detected photoelectrons (p.e.) because of the smaller photon path length dispersion along a fiber compared to the photon transmission in bulk scintillators. Good timing is even more important for veto calorimetry.

In the proposed experiment the main challenge for the veto detectors is a requirement of an extremely low inefficiency for photons, at least 2×10^{-4}, in the range of 10–500 MeV with an average energy of around 120 MeV. Figure 55 shows the energy spectra of photons, which hit the barrel veto.

Inefficiency comes from the following sources:

1. Escape of photons before conversion (gaps and “punch–through”).
2. Sampling fluctuations (no visible energy detected in the active material).
3. Photonuclear interactions (no electromagnetic shower).

The first factor has mainly a geometrical nature and can be minimized by careful design, i.e. sufficient thickness of the detector in all possible directions. The sandwich design has an advantage in minimizing the “dead material” directions. Sampling fluctuations dominate the

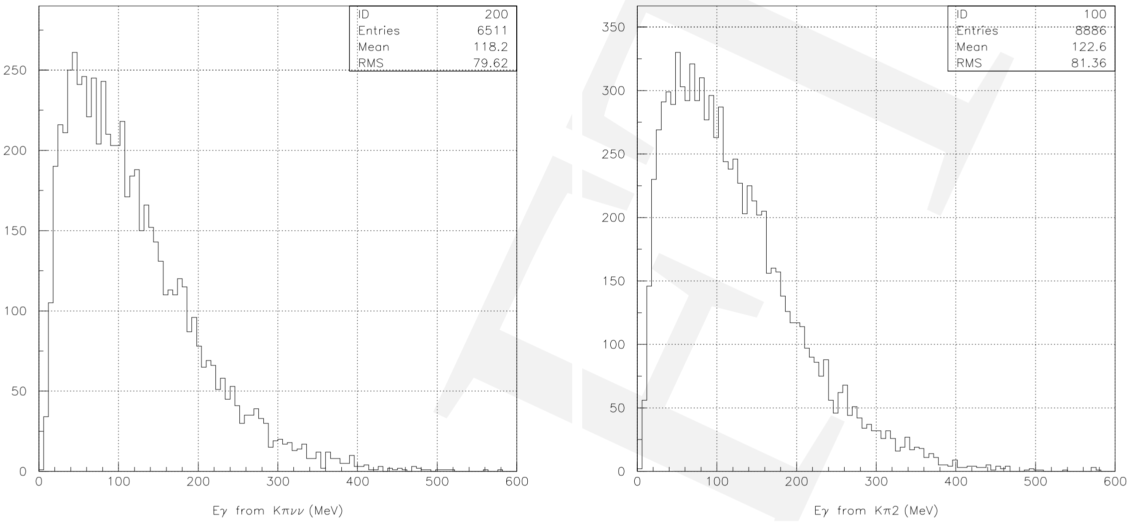

Fig. 55. The energy spectrum of photons detected in the barrel veto from kaon decays $K_L^0 \to \pi^0\nu\bar{\nu}$ (left) and $K_{\pi 2}$ (right).

inefficiency for low energy photons. The large inefficiency for low–energy photons comes from absorption of the photon charge product in a non–active material (lead). Reducing the lead thickness to 0.5 mm in the first layers will reduce the sampling inefficiency. At higher energies photonuclear interactions dominate the loss of photons and set the upper limit of the detection efficiency.

The AGS experiment E787 measured photon detection inefficiencies using the $K^+ \to \pi^+\pi^0$ decay mode. The inefficiency was 4×10^{-4} for energies of around 100 MeV for a sandwich detector made with 1 mm thick lead and 5 mm plastic. The inefficiency goes down to 10^{-4} for the energies above 200 MeV. The photo-yield of the E787 veto detector was 10 p.e. per MeV of visible energy. In KOPIO we aim to reach a photoelectron yield of 12 p.e. per MeV of visible energy with a larger visible fraction.

Overview of the WLS fiber readout technique

In general, a standard fiber consists of a polystyrene core with refraction index n_1=1.60 coated with a thin transparent PMMA cladding with smaller n_2=1.49. Multi–clad fibers have an outer fluorinated PMMA cladding (n_3=1.42) over the inner one, as shown in Fig. 56. The core contains a fluorescent dopant selected to absorb the light from a scintillator detector and to re–emit isotropically at longer wavelengths (see Fig. 57). The two layers of cladding provide a highly efficient reflective surface for transporting the re–emitted light within the total reflection cones. It should be noted that the 70% larger trapping efficiency of the multi-clad fibers compared to the single-clad ones is offset partially by higher reflection of the incident scintillating light. As a result, multi-clad WLS fibers produce 35–45% more light than single-clad fibers of the same type. To increase the geometrical acceptance of the incident scintillation light, the fibers are placed in grooves carved in the bulk scintillator. The optimum groove depth slightly exceeds the fiber diameter. Light output is increased with increasing number of grooves (fibers) up to some level of saturation. The optimum depth and number of embedded fibers must be determined for a particular application and geometry. WLS fiber readout technique is described in detail in Ref.[6,7].

Fabrication of grooved plastics and test results

The extrusion technique of long grooved scintillators was developed at the Technoplast Factory, Vladimir, Russia. In the first stage, an investigation was done to determine the optimum dopant compositions for a polystyrene based scintillator. The optimization was directed at reaching the highest light yield. The light yield of small tiles ($20 \times 100 \times 6$ mm^3) was measured with a ^{90}Sr β–source triggered by a reference counter. The scintillation light was absorbed by a multi–clad BCF99–29AA (Bicron) fiber ([8]). A paraterphenyl (PTP) concentration of 1.5% and a concentration of POPOP 0.01% were chosen, since the light yield was nearly constant at concentrations of 1.5–2.0% and 0.01–0.05% of PTP and POPOP, respectively, which is in good agreement with the more detailed results obtained in Ref.[9]. The standard composition of 1.5%PTP + 0.01%POPOP provides a light yield of about 80% of the light yield of Bicron BC408 scintillator for the configuration tested.

The samples were manufactured using an extrusion technique which allows us to produce very long ($>$4 m) grooved plastic slabs with a good reflective surface. A scintillator is extruded through a spinneret and a triple roll calendar equipped with an additional gear to form the grooves. The extrusion line provides a homogeneous thermal mixing of polystyrene pellets and fluorescent dopants at a temperature of 160–240°C. During squeezing–out a scintillator polymerizes isotropically over a volume. The extrusion velocity depends on the plastic thickness and varies from 0.15 to 0.6 m/min. Simple tests with small scintillators and direct plastic–PMT contact showed that an extruded polystyrene gives the same light yield as a molded one. Transparency of the extruded scintillator is homogeneous in all directions, and the light attenuation length was measured to be about 30 cm in a 5 mm thick extruded strip[10]. The extrusion technique does not provide high precision control of dimensions. The slab width tolerance is required to be 0.1 mm to avoid gaps between counters, which adversely affect the detection efficiency. A laser cutter trimmed the width to 150±0.1 mm. For technical convenience, the tested 7 mm thick samples were produced in lengths of 0.5–2 m, with widths of 150 mm. The profile of the 1.1 mm deep grooves deviated from an ideal U–shape during plastic hardening.

Instead of using a wrapping material for the reflector we applied a novel technique: the scintillator is etched by a chemical agent that results in the formation of a micropore deposit over the plastic surface, following which the diffuse film is fixed in a settling tank. The deposit thickness depends on the etching time. An advantage of this approach over the commonly used white diffuse papers is the almost ideal contact of the reflector with the scintillator. Moreover, it provides the option of gluing a lead sheet to the plastic which facilitates assembling a sandwich unit. It was found impractical to shield the grooves during

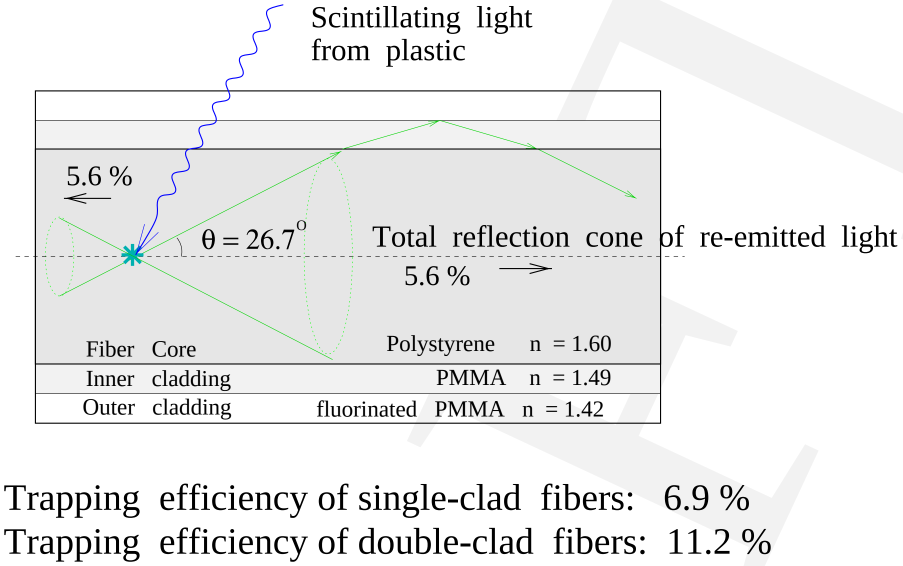

Fig. 56. Light propagation in a multi–clad fiber .

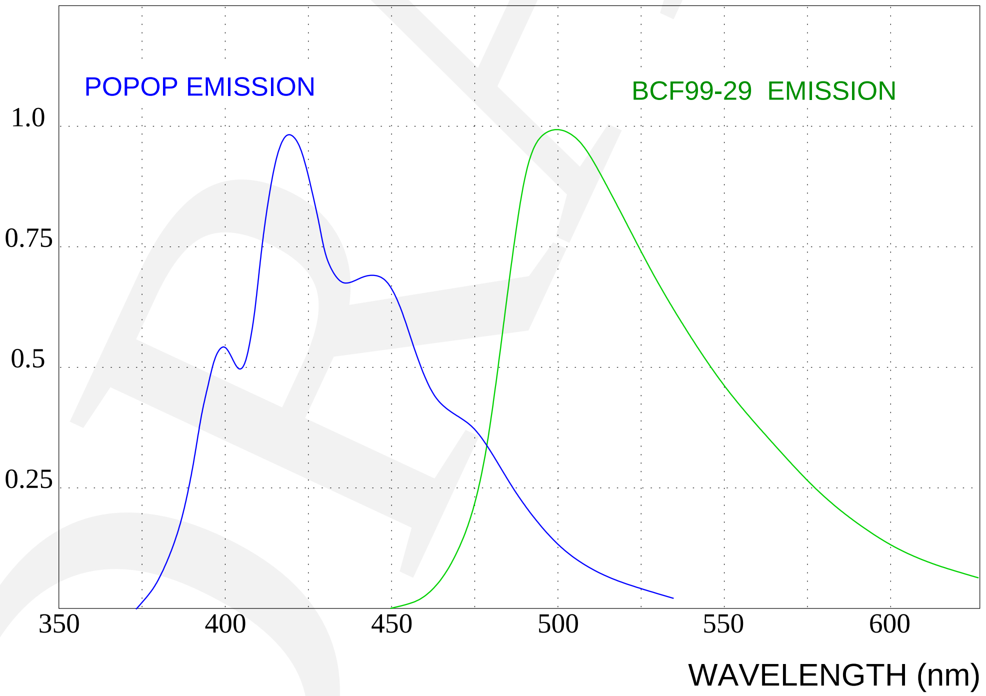

Fig. 57. The emission spectra of a scintillator with POPOP dopant (blue) and BCF99-29 WLS fiber (green). The WLS fiber absorbs the scintillation light and re–emits it at longer wavelengths.

etching. After etching a scintillator, including the grooved surface, the white deposit inside the grooves is removed by scraping along the groove profile. The scraping die also forms the groove to an optimum U–shape cross–section. Then the groove surface is rubbed with a solvent to obtain a polished transparent surface suitable for accommodating fibers. A colorless silicone grease was used as an optical coupling between the fibers and scintillator in the tests of single slabs.

The light yield of the counters was measured with cosmic rays. Fibers of 1–mm diameter are read out on both ends via FEU–115M photomultipliers[11], which have a photocathode sensitivity extended in the green light region, appropriate to detect the WLS fiber light. The fibers used in all tests have a length of 4.3 m. We tested single–clad BCF–92 and multi–clad BCF99–29AA fibers. Their decay time is about 3.3 ns, and the attenuation length is about 4 m at distances of more than 1 m.

The first sample tested was a 2 meter long slab with a 19 mm spacing between grooves. The scintillator with embedded multi–clad BCF99–29AA fibers was wrapped in one layer of Tyvek white paper. The total light yield from both ends was about 11.2±0.5 photoelectrons (p.e.) per minimum ionizing particle (MIP) within a range of 1.5 m within the scintillator length, i.e. it did not depend significantly on the position along the counter. The light propagation velocity was measured to be 5.8 ns/m.

Then, the extruder spinneret was modified to produce scintillators with 10 mm spacing between the grooves. The samples tested were 1 m long. 14 multi–clad WLS fibers were embedded in the grooves, and a single layer of Tyvek paper was used as a reflector. The total light yield from both ends was measured to be 17 p.e., or about 12 p.e./MeV.

The next step was to apply the new etched reflector instead of the Tyvek paper. Prepared in this way a 1 m long counter produced a light yield of 19.6 p.e. per MIP, i.e. about 14 p.e./MeV. The ADC spectra obtained in the center of the plastic are shown in Fig. 58. Embedding single–clad BCF–92 fibers reduced the light output of the chemically etched sample by 24%, to 14.9 p.e. per MIP. Further reduction of the spacing between the grooves also increases the light yield. For a spacing of 7 mm, light yields of about 26 p.e./MIP and 20.8 p.e./MIP were measured with multi–clad and single–clad fiber readout, respectively.

A 7 mm thick counter made of BC404 scintillator was also tested. It was chemically etched and the grooves were cut with 7 mm spacing by a scraper. The light yield was measured to be 32 p.e./MIP, i.e. 23% more light output than for the polystyrene extruded plastic with the same multi–clad fiber readout.

Constant–fraction discriminators with a threshold set at a level of about 1 p.e. were used to obtain the timing performance of the counters. The start signal was triggered by a fast plastic while the stop signals were produced by the FEU–115M. The timing was derived from $(t_1 + t_2)/2$, where t_1 and t_2 are the stop signals from both ends. A time resolution of 0.85 ns (rms) for cosmic particles was obtained for a chemically etched sample with 10 mm spacing for multi–clad BCF99–29AA readout (Fig. 59). For single–clad BCF–92 readout the resolution was 0.87 ns. The time resolution for the sample with 7 mm spacing was 0.71 ns (rms) with multi–clad readout, and 0.76 ns with single–clad fibers. It is interesting to note that single–clad fibers with spacing of 7 mm provide a comparable light yield to multi–clad ones with spacing of 10 mm with improved timing.

A 1 m long thin extruded slab of 3 mm thickness manufactured with the chemically etched reflector was also tested. 14 multi–clad BCF99–29AA fibers were embedded in the 1 mm deep grooves, which run with 10 mm spacing. We obtained a light yield of 8.5 p.e. per MIP and time resolution of 0.92 ns (rms). As expected, the measured light output is strictly proportional to the plastic thickness. The results of measurements of the extruded counters ([12]) are summarized in Table 8.

Table 8. Parameters of extruded polystyrene counters with 4.3 m long WLS fiber readout. The counter made of BC404 scintillator is also shown for comparison.

Counter thickness mm	Spacing mm	Fiber type	Light yield p.e./MIP	σ_t ns
7	19	multi–clad	11.2	
7	10	multi–clad	19.6	0.85
7	10	single–clad	14.4	0.87
7	7	multi–clad	26.2	0.71
7	7	single–clad	20.8	0.76
3	10	multi–clad	8.5	0.92
7 (BC404)	7	multi–clad	32	0.65

Veto performance

Prototype sandwich module

The sandwich prototype module was made with a length of 1 m while the length of the WLS fibers was 4.5 m, i.e. about the length of fibers in the KOPIO detector. 10 layers of 7 mm thick extruded plastic slabs and 1 mm lead plates were fixed together in a monolithic block by an elastic polyurethane glue. The module was protected by a 100 μm stainless steel container. Single–clad BCF–92 fibers were glued in the grooves with 10 mm spacing. Taking into account the large quantity of fibers required for the KOPIO we plan to use multi–clad fibers only for the most sensitive parts of the veto system, where maximum light yield is crucial to reach a high efficiency. A chemical composition based on a polystyrene solution was used as a glue. 140 fibers were compressed in the collets on both ends of a fiber bundle and coupled to FEU-115M phototubes.

The light yield was measured to be 12.2 p.e. per MIP, i.e. 12.2 p.e. for a single layer. This result is 18% smaller than we obtained in the tests of a single plastic counter with the same single–clad fiber readout. This light yield drop is attributed to the glue, which showed aging effects of a chemical nature. The timing was measured with the same method as for the single counters. The overall time resolution was obtained to be 440 ps (rms). Taking into account the time spread contribution from the trigger counter (250 ps) the time resolution contribution of the sandwich module is deduced to be 360 ps. Light yield nonuniformity

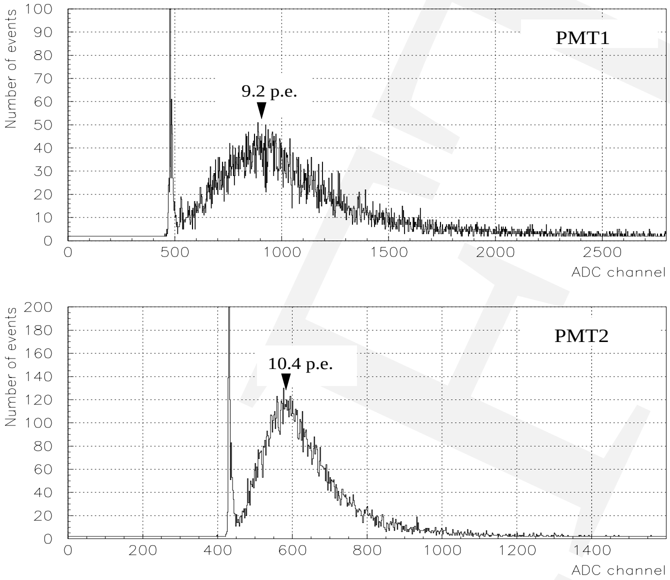

Fig. 58. ADC spectra for both ends of the 7 mm thick counter with 10 mm spacing between the multi–clad BCF99–29AA fibers.

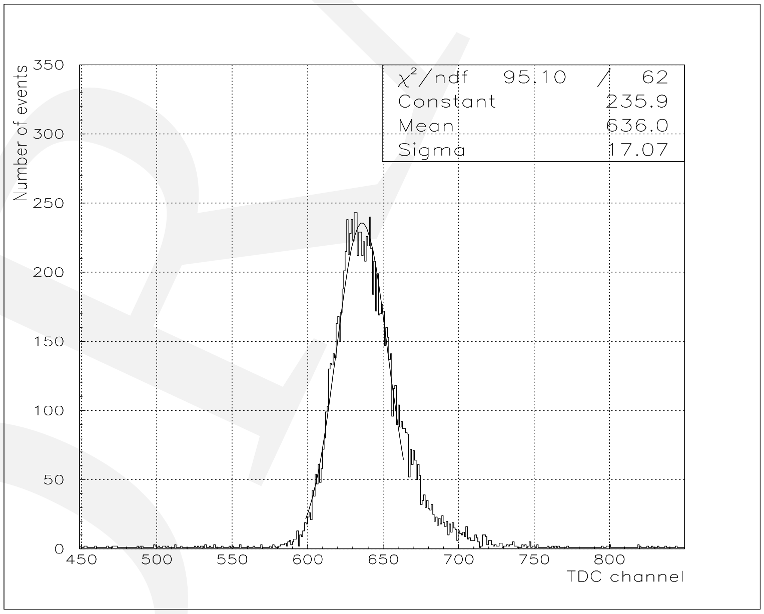

Fig. 59. Time spectrum of the counter with 10 mm spacing between the grooves. Time is measured as average between TDC stops of both PMTs. Scale: 50 ps/ch.

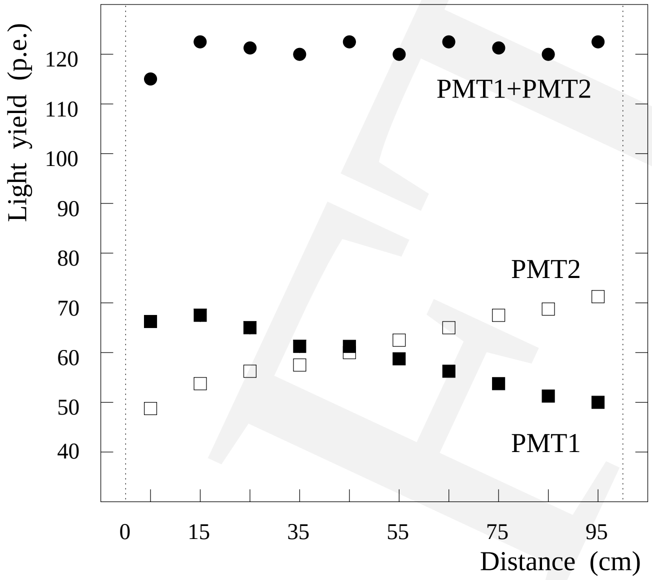

Fig. 60. Light yield uniformity along the prototype sandwich module of 1 m length. The distance is measured from the left module edge.

along the module was measured in 10 cm steps. As shown in Fig. 60, the light yield was stable with deviation ±1% from the average over the 90 cm length. The attenuation length was evaluated to be around 2.4 m.

Segmentation of veto

The thicknesses of lead and scintillator in a sandwich determines the main detector parameters such as sampling fluctuations, localization of an electromagnetic shower, energy resolution, timing and inefficiency. Taking into account both the cost and the physics objectives the proposed veto segmentation is shown in Fig. 61 and the detailed layout is listed in Table 9. The veto thickness is $18X_0$. The veto barrel is built of 22 supermodules (SM), each enclosing 33 modules of 3 different types. The supermodules for side walls are shorter than the ones for the roof or floor, 4.2 m versus 4.9 m. The first two levels of SM are lined with modules (M1 and M2 types) with the fine sampling structure provided by a 0.5 mm thick lead foil. 95% of photons will interact there, and therefore this is the most sensitive part of the veto detector. Thin lead and high light yield in the scintillator achieved by densely spaced fiber readout reduces the detection threshold. Different widths of M1, M2 and M3 modules allow us to pack them in a SM without long inactive gaps. The 10 cm width of M1 facilitates shower separation as well as event reconstruction. The 14 cm width of M3–M6 modules was chosen to reduce the random vetoing due to the background environment.

There are two main methods to increase the light output for an active layer: enhanced fiber readout and scintillator thickness. Moreover, a thicker active layer increases the visible part of the deposited energy improving the energy resolution and efficiency. Thus, we decided to keep constant the scintillator layer thickness and make the fiber spacing 6 mm in M1 modules, widening it to 10 mm for M3–M6 modules.

Evaluation of veto performance

The expected performance of the veto barrel is summarized in Table 10. The energy resolution was estimated in a GEANT simulation of the veto structure described in the previous section.

The visible energy fraction is about 0.5. Using scintillator test results we evaluate the photo-yield to be 5 p.e. per MeV of the energy deposited in both active (scintillator) and passive (lead) layers. We will collect 500-600 p.e. for a typical 100 MeV photon.

Extrapolating the parameters obtained for the prototype module, the time resolution of the veto detector is estimated to be 180 ps (rms) for a 100 MeV photon, or 56 ps/$\sqrt{E_\gamma[\mathrm{GeV}]}$. The KLOE calorimeter assembled by gluing 1 mm scintillation fibers of 4.3 m length between 0.5 mm lead foil reached the time resolution of 72 ps/$\sqrt{E_\gamma}$ at the light output of 1660 p.e./GeV in a beam test[3]. Tests with cosmic rays of KLOE modules produced even better resolution of 58 ps/$\sqrt{E_\gamma}$, which supports our timing expectations for the KOPIO veto detectors.

Since the light propagation velocity in the fibers was measured to be 17 cm/ns, the accuracy in the localization of an electromagnetic shower could be about 3.1 cm (rms) for a 100 MeV photon. However, electromagnetic shower spread degrades the space resolution along the fibers. The resolution in the other direction is defined by the width of the modules as well as the shower spread. We are able to recover the shower direction measuring the center-of-gravity at each level (M1–M6) and drawing the line through these centers by χ^2 method. We used the simplest algorithm to obtain the position:

$$x = \frac{\Sigma\, x_i E_i^{0.7}}{\Sigma\, E_i^{0.7}} \ ,$$

where E_i is the energy visible in a module. This method gives a systematic shift which was corrected. The angular resolution of the veto barrel for 100 MeV photons is shown in Fig. 62. We simulated the photons irradiated from the center of the veto barrel at angles uniformly distributed between 45 and 135°. The Fig. 62 shows the difference between the recovered angle and simulated one. An angular resolution of 244 mrad for a typical angle of 70° leads to the decay position accuracy of σ_z=48 cm, that is 2.3 times worse than for a photon which hits the preradiator. Figure 63 presents the angular resolution versus photon energy. Thus, the barrel veto system will provide useful information on extra photons which may allow a selective veto process.

Mechanics

The orientation of the supermodules around the decay volume is depicted in Fig. 61. The veto barrel is divided into 3 main parts: roof, floor and side walls, each of them has its own mechanical support. The total weight of the barrel veto is about 120 t. Floor and side walls are fixed after assembly. The roof is required to be able to be moved by 40 t crane. The total

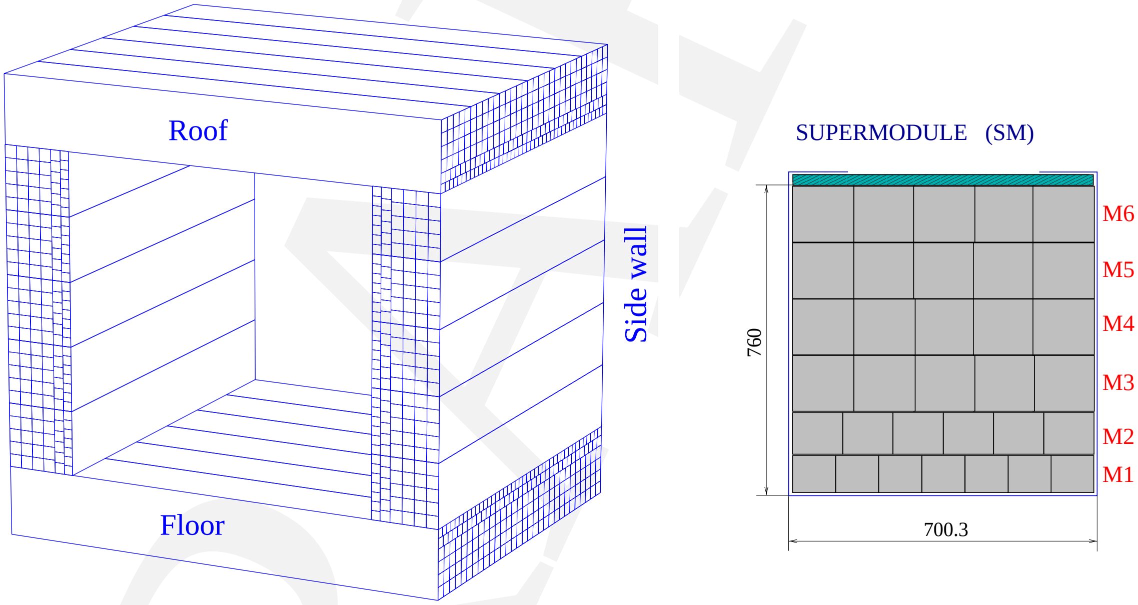

Roof&floor SM size: 70x76x490 cm
Side wall SM size : 70x76x420 cm

Fig. 61. The segmentation of the barrel veto. The supermodule consists of 33 modules. The barrel veto is built of 22 supermodules.

Table 9. Segmentation and layer layout over the veto thickness. (CH is a plastic scintillator).

Module type	M1	M2	M3–M6
Number of layers	14	16	19
Pb thickness, mm	0.5	0.5	1.0
CH thickness, mm	7.0	7.0	7.0
Length, m	4.9	4.9	4.9
Cross-section, mm^2	100 x 105	116.5 x 121	140 x 152
Radiation thickness, X_0	1.5	1.7	3.7
Fiber spacing, mm	6	8	10
Number of fibers	224	224	266
Weight, kg	90	120	244

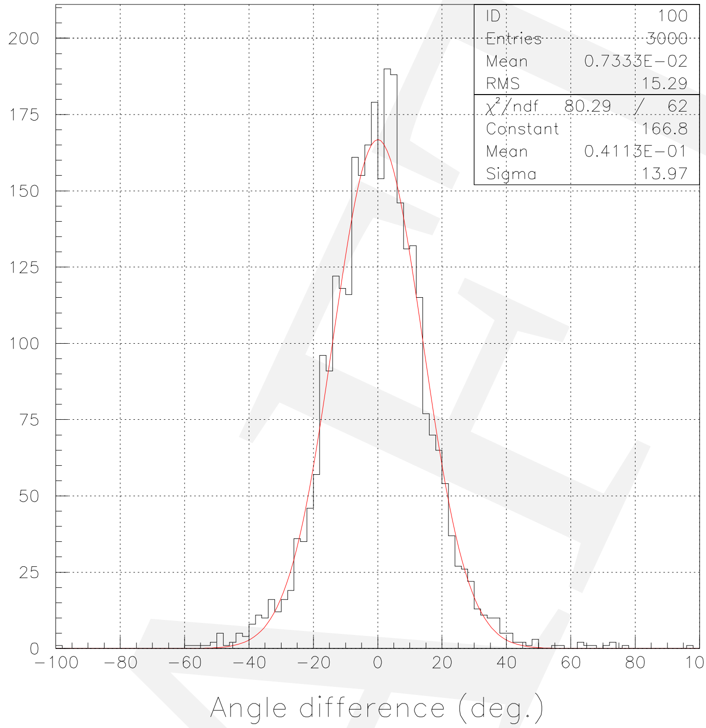

Fig. 62. The angular resolution of the barrel veto for 100 MeV photons. The histogram shows the difference between the recovered angle and simulated one.

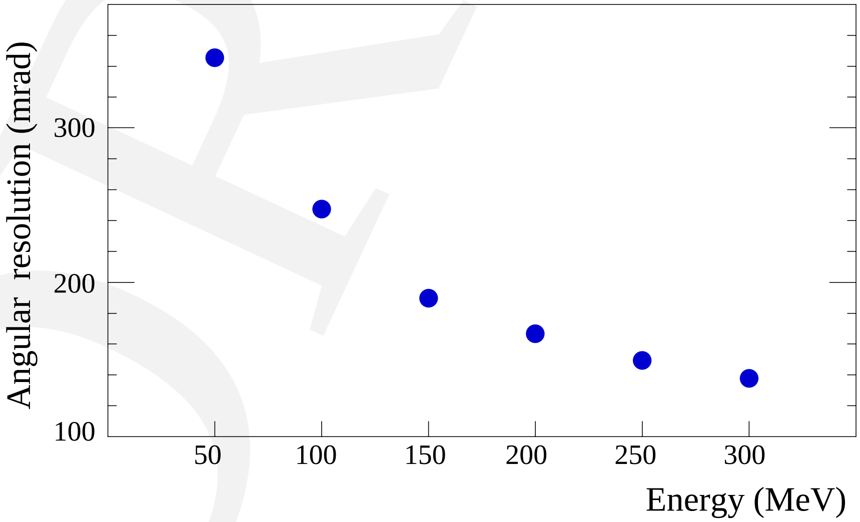

Fig. 63. The angular resolution (σ) versus photon energy.

Table 10. The expected veto performance.

Parameter	Value	Note
Photon inefficiency	1.5×10^{-4}	E787 results, simulation
π^0 inefficiency	$\sim 10^{-8}$	E787 results, simulation
$\sigma_E/\sqrt{E(GeV)}$, %	3.2	Sampling fluctuations only
$\sigma_E/\sqrt{E(GeV)}$, %	5.0	Total energy resolution
$\sigma_t/\sqrt{E(GeV)}$, ps	60	Prototype test
Position resolution, cm	3–4	Segmentation and timing
Angular resolution, mrad	250	GEANT at E_γ=100 MeV

roof weight is about 35 t, and can be made as a whole structure or split in 2 parts. In order to respect the physics requirements the mechanical design must have the minimum amount of inactive material before the first scintillator layers. Also, the supports have to ensure high rigidity for the roof.

While the floor modules can be stacked without any mechanical structure, the roof SM is supported by stainless steel containers which enclose 33 modules. Their weight is 5.7 t, and the container wall thickness is 500 μm. Taking into account the sandwich structure and glued fibers the main concern is to prevent the modules from deflecting. As it can be seen from Fig. 61 the backbone of a roof SM is a thick metal plate, to which the external support mounted. Roof SM are suspended from girders which rest on the vertical reinforced support outside of the veto. The specified gap between the neighboring SMs is 1.5 mm, where the container walls are included. Monte–Carlo simulation predicted that negligible additional inefficiency is introduced by the gaps.

The gaps in the veto side walls do not introduce inefficiency as the kaon beam profile is not coplanar with the gap planes. Thus, there are no photon trajectories extending to the beam region which go through the gaps between SMs.

Instead of using containers the side wall SMs are enclosed by thin straps extending from the outside construction. Since the side SMs are supported by their weight at shelves the straps serve mainly as safety belts.

For the roof and floor veto modules the phototubes are placed at the module ends inside light tight cases which are attached to a module container. In such a configuration the fibers extend out of the sandwich for 15 cm. Roof and floor SMs can be installed with the phototubes as complete packages. The veto side walls are oriented in such a way that there is no space available to mount the phototubes directly at the module ends. The fibers are bent and brought out of the detector, where the PMT support is installed. The gap needed to route out the fibers is 10 cm. Special heating technique is applied to make the fiber curve with a radius of 5-7 cm. Using this technique the single-clad fibers were bent with a radius of 1.5 cm for the PHENIX calorimeter prototype. After 7 years no crazing or aging effects are observed in the bent fibers. Vertically mounted modules are considered to close the gaps between the side walls and preradiator and completely seal the barrel volume.

Upstream photon veto

The upstream veto is made of the sandwich modules which have basically the same design as described above. The main difference is readout segmentation. The upstream veto modules are enlarged to allow the phototubes to view more layers. Also the central modules beside the vacuum veto have single-ended readout as shown in Fig. 64. The upstream veto can be a source of background γ's produced in halo neutron capture. However optimization of the beam collimator suppresses the number of these neutrons, and the active detector medium allows us to detect such events.

The upper half of the detector must be vertically moveable to provide easy access for the vacuum vessel. The separation is below the beam plane.

Readout and electronics

Readout of veto modules is implemented with the photomultipliers FEU–115M, which are extensively used in the PHENIX calorimeter. Their main advantages are low cost and the photocathode extended in the green light region, approapriate to detect the WLS fiber light. FEU–115M were tested for their relative sensitivity to green light. The green LED generated a pulse that was measured by the phototubes. The response of the FEU–115M was n_{LED}=110 p.e. The two tested Hamamatsu tubes R1398 with bialkali photocathodes of similar diameter produced about 85 p.e. The FEU–115M is produced at the MELS Factory (Moscow, Russia). Its parameters are given in Table 11. Voltage divider circuits can be produced in a hybrid design at the same factory.

The electronics for the veto detectors is similar to that described in the calorimeter section. Custom designed FEE cards pipeline the energy and time information with small dead time. For trigger purposes the card produces digital signals.

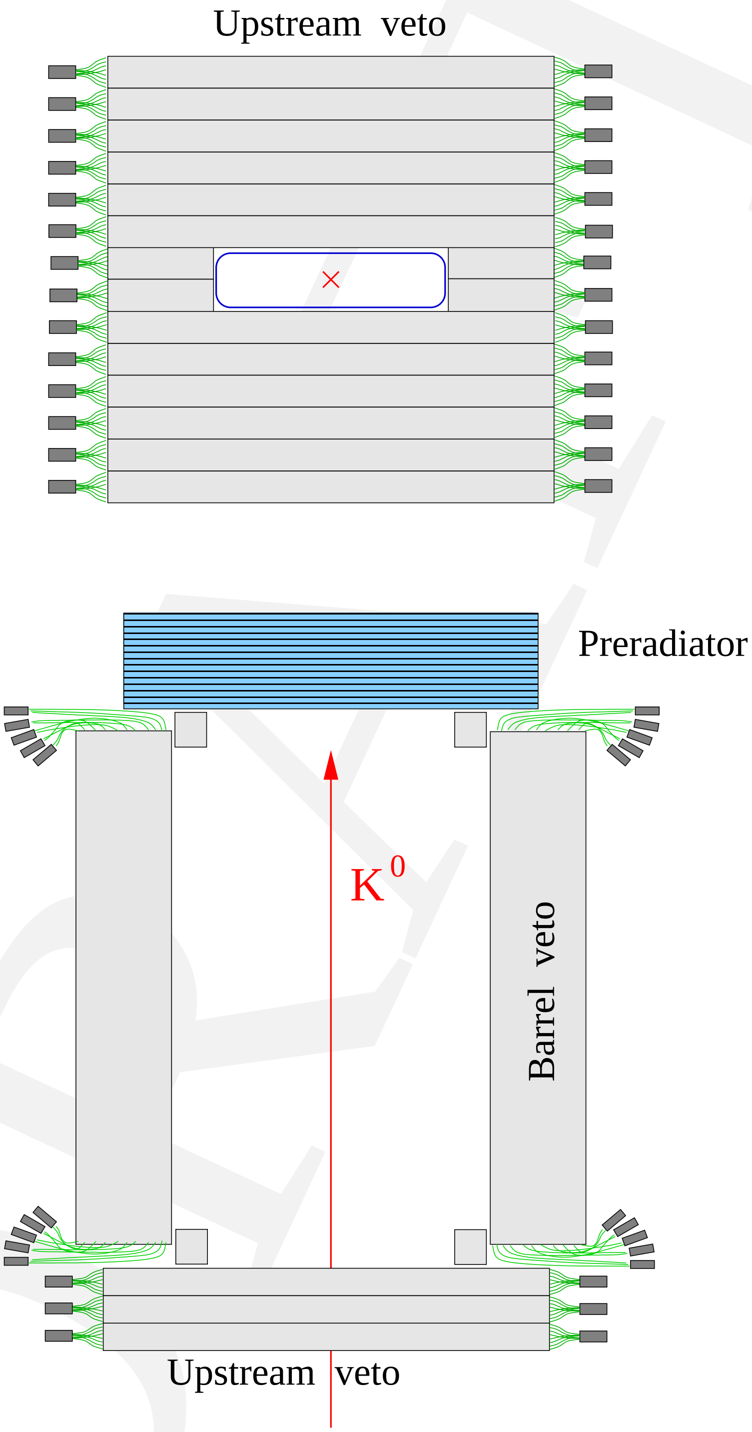

Fig. 64. Schematic view of the upstream veto.

Table 11. Specification for FEU–115M phototubes.

Photocathode diameter	25 mm
Number of stages	12
Quantum efficiency at 500 nm	15%
Gain at 2000 V	2×10^6
Rise time	<4 ns
Nonlinearity up to 80 mA peak current	<2%
Rate at 3 p.e. threshold	10 Hz

Downstream Veto System

In order to eliminate background events with charged particles and/or additional photons the veto scheme must extend downstream of the decay region, including the beam region itself which is discussed in the section on the beam catcher.

These downstream veto detectors can be subdivided into three groups covering the decay tank to the high vacuum window (DSV1), the high vacuum window through the sweeping magnet (DSV2), and the downstream vacuum tank (DSV3). The same technologies used for the barrel and decay regions will be applied here. That is, charged particles will be detected by scintillator liners in DSV1 and DSV2 where they are deflected out of the beam plane by the sweeping magnet into a wall of scintillators at the entrance of DSV3. Photons will be detected in shower counters made up of unit layers of 7 mm thick scintillator and 1 mm lead. The shower counters will be 80 layers thick or about 15.5 radiation lengths. The scintillators will be read out by WLS fibers imbedded in grooves which will carry the light to the PMTs. Further details on each downstream veto region are described below.

DSV1

Charged particles will be vetoed by a scintillator system similar to that described in the main decay region. It will consist of scintillator plates read out by WLS fibers. The scintillator will be separated from the high vacuum by a thin membrane. Readout will be via the fibers taken through vacuum feedthroughs to 8 PMTs outside the vacuum system.

Photons will be vetoed by lead-scintillator arrays placed above and below the beam pipe at the entrance to the magnet, just upstream of the magnetic shield plate. These two arrays will each be 30-cm high by 250 cm long and 64 cm (i.e., 80 layers) thick and will be viewed by 6 PMTs on each end, for a total of 24 PMTs.

DSV2

The high-vacuum region ends at a window just upstream of the sweeping magnet. This window is physically part of a vacuum box which is supported inside the modified 48D48 magnet. This magnet sweeps charged particles from the decay region (and from downstream decays) vertically out of the beam.

Charged particles are detected by scintillator plates inside the vacuum box which cover four sides and a downstream aperture above and below the beam. These plates are read out by WLS fibers which are brought out of the vacuum to 12 PMTs.

Behind the scintillator are four photon veto arrays which line the sides of the vacuum box and the downstream beam aperture intercepting all possible photon trajectories from the decay region. Because of the limited space in the magnet gap the two arrays here will be only 60 layers thick, but most photon trajectories will strike these areas at oblique angles. Each of the 4 arrays is 50 cm high by 250 cm long and are also read out by WLS fibers, which are brought out of the vacuum to a total of 48 PMTs outside.

DSV3

The downstream vacuum is contained in a commercially fabricated 4.2 m diameter tank of either steel, or steel-lined concrete. It is joined to the magnet vacuum box at its upstream end, and has a removable access plate with vacuum window in the beam region at its downstream end. Multiple ports are provided on both sides for support and insertion of the four photon vetoes on each side which are arranged in a “chevron” configuration. This arrangement maximizes the coverage for photons originating upstream in the decay region and limits the rate from photons produced by beam interactions with the low vacuum in the downstream region. Each of these eight veto modules are 70 cm high by 90 cm long and are read out with fibers brought out by feedthroughs to eight PMTs (total 64 PMTs).

At the downstream end of the large tank are an additional two veto arrays, 50 cm high by 300 cm long, which define the vertical beam aperture and are read out by another 24 PMTs. All photons from the decay region must intersect one of the side or vertical modules, or exit the tank into the beam catcher.

5.5 Beam Catcher

Overview

The main purpose of the beam catcher is to detect photons escaped through the beam hole. It is located at about 15 m downstream of the detector, and covers an aperture of 4 m (width) by 20 cm (height). The challenge in designing the catcher is to reduce the sensitivity to unwanted particles, such as neutrons and K_Ls, while keeping high enough sensitivity to photons. If the catcher were sensitive to these particles and its counts were dominated by them, it would have a high probability of vetoing genuine signals.

Figure 65 shows the energy spectrum of photons that the catcher must detect, namely those photons that originate from the $K_L \rightarrow \pi^0\pi^0$ backgrounds after various kinematical cuts.

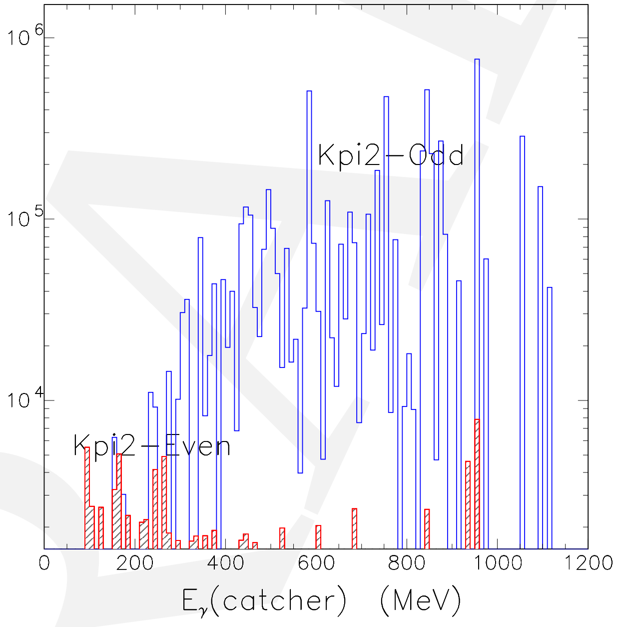

Fig. 65. Energy distribution of photons in the beam hole for $K_{\pi 2}$ even (hatched) and $K_{\pi 2}$ odd type events.

As can be seen, the background photons are mostly the odd-pairing photons with energy greater than 300 MeV. Thus, the most important requirements of the catcher is good efficiency for photons greater than about 99%. At the same time, we demand that it must be insensitive to neutrons; roughly speaking, its sensitivity should be less than 0.3% for neutrons with kinetic energy of 0.8 GeV, which will be the main contributor to the false veto probability (see below for detailed discussions of the veto probability).

Originally, we considered two possible catcher designs, one based on a lead-acrylic sandwich calorimeter and the other on an aerogel distributed Čerenkov counter. We performed further studies by Monte Carlo simulation, and came to the conclusion that only the latter design satisfies the requirements, because it has sufficient insensitivity to neutrons at a fixed photon sensitivity.

Catcher Design

The catcher consists of 512 modules of the design shown in Fig. 66. Each module is composed of 2 mm thick lead, 50 mm thick Aerogel radiator $(n = 1.03)$, a light-collection system of a mirror and funnel, and a 5 in. photomultiplier tube. The Aerogel cross section is 20 cm in height and 20 cm in width. The modules are arrayed in 25 rows (transverse to the beam) of 20 (or 21) modules, with the rows separated by 35 cm. The modules in a row are staggered laterally by a half module from those in the following and preceding rows. There are 25 modules along the beam direction for a total of 8.3 radiation lengths over a distance of 8.8 m.

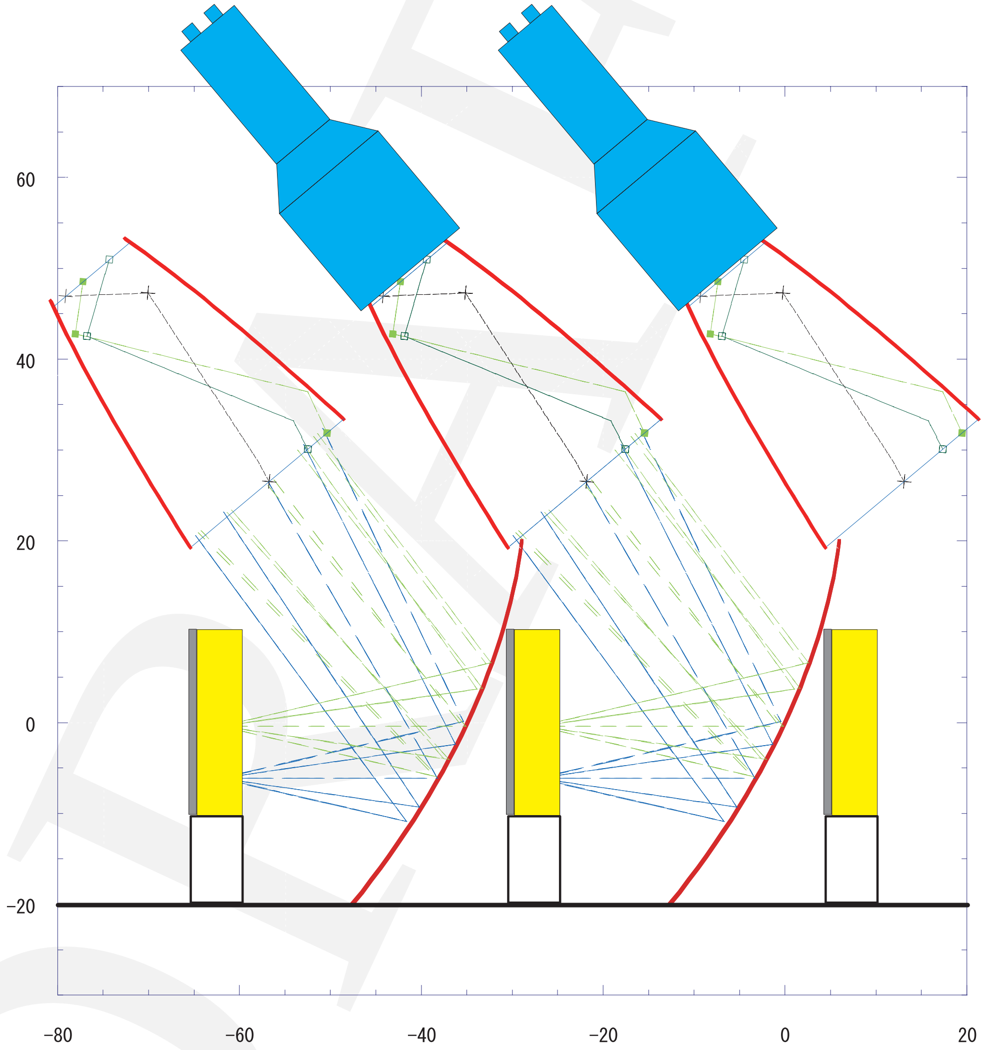

Fig. 66. The design of the catcher module.

Expected Performance

In order to study the catcher's performance, Monte Carlo simulations were performed. We used the GEANT3 simulation with the GCALOR package for hadronic showers. The number of photons produced by the 5 cm thick aerogel was assumed to be given by the formula established experimentally by the HERMES group[1], and only unscattered photons were assumed to exit the radiator. As will be explained below, the light collection system from the aerogel to its photomultiplier can collect about 70% of the emitted light. However, we assumed conservatively only 50% light collection efficiency in these simulations. Figure 67 shows the resultant photon detection efficiency as a function of its incident energy. To be identified as a photon signal, the catcher must have two consecutive "hits" in coincidence. Specifically, a "hit" means that one module must yield 8 photoelectrons, equivalent to passage of two tracks (e^+ and e^-), and there must be another "hit" in one of the modules right behind it. As can be seen from the figure, this gives 98.5% efficiency for 300 MeV photons. Figure 68 shows the efficiency for neutrons. The coincidence condition gives less than 0.2% efficiency for 0.8 GeV neutrons (which are the main contributor to the false veto probability as described in the next section), satisfying our requirement for the catcher. Figure 69 shows the energy resolution of this detector; here signals (photoelectrons) from a shower band, defined as those within ± 3 transverse modules along the shower axis, are summed up. Finally, we checked the efficiency of the detector for K_Ls. Figure 70 shows the results; the efficiency is only 7% at 1 GeV/c, most of which is due to K_L decay in the catcher.

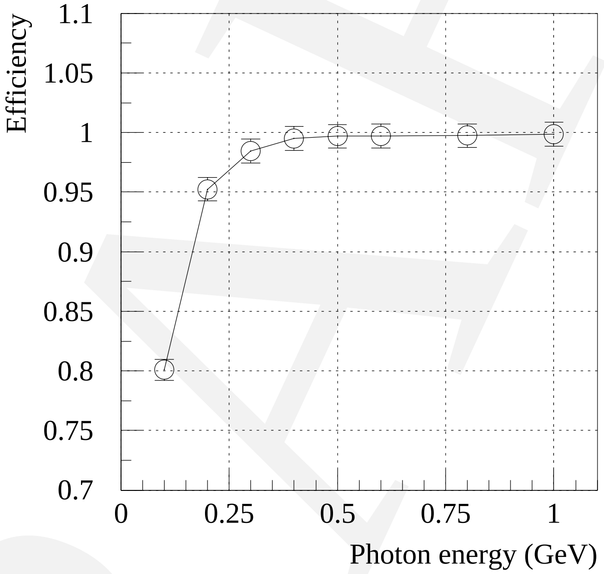

Fig. 67. Efficiency for photons as a function of incident energy.

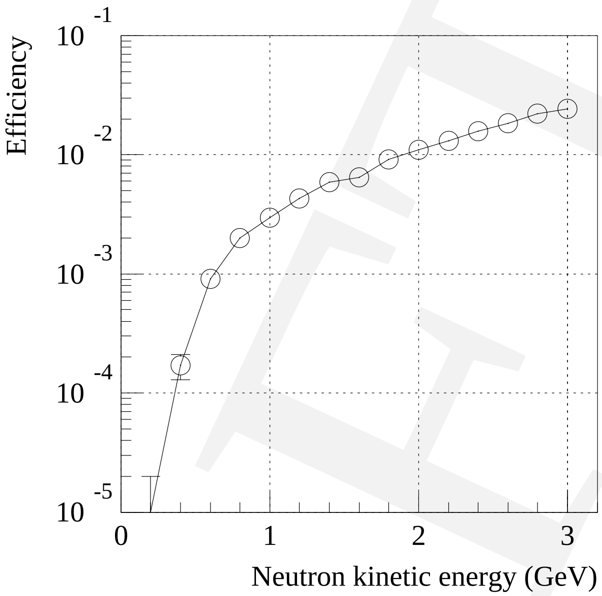

Fig. 68. Efficiency for neutrons as a function of kinetic energy.

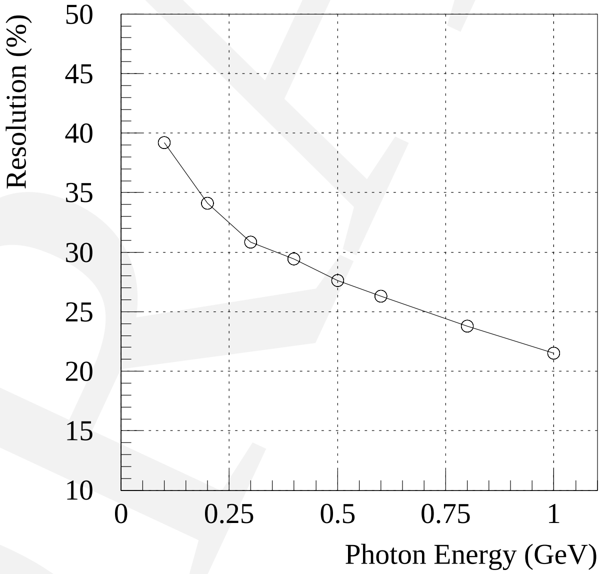

Fig. 69. Energy resolution for photons.

False veto probability and single counts

We chose the coincidence condition (8, 8) to be our standard one, and calculated the false veto probability. Figures 71 and 72 show the differential coincidence rate per microbunch of neutron and K_L, as a function of neutron kinetic energy and K_L momentum, respectively.

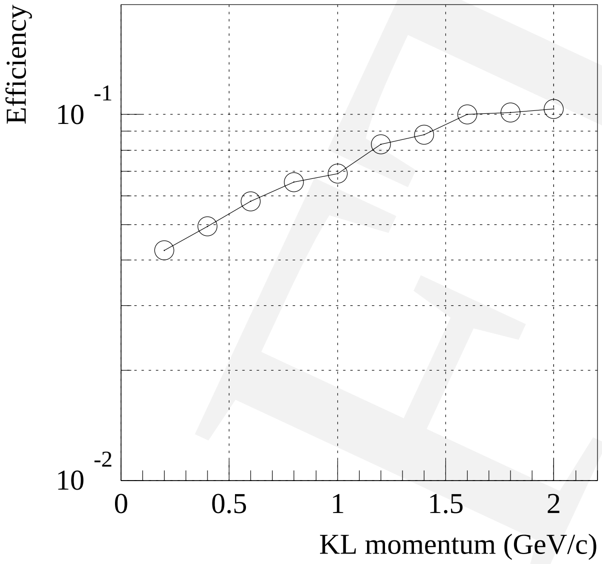

Fig. 70. Efficiency for K_L as a function of momentum.

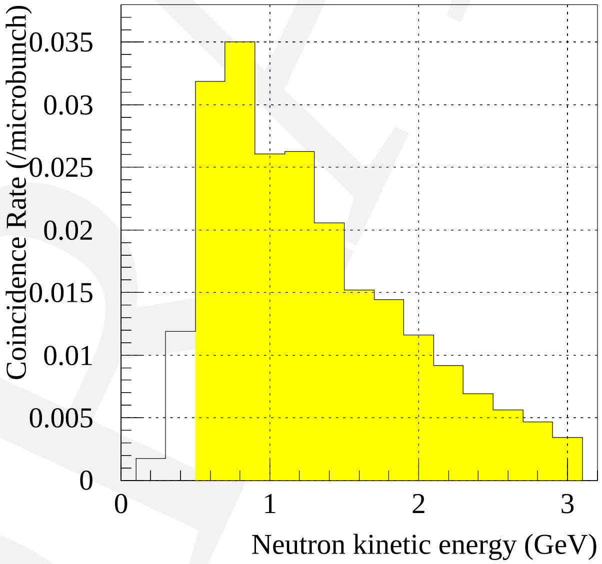

Fig. 71. Differential coincidence rate due to neutrons.

As can be seen, the main contribution comes from neutrons around 0.8 GeV. Integrating the contribution above 0.6 GeV where neutrons come into the singal time window, the shaded area in Fig. 71, we obtained about 0.21 counts per microbunch. Similarly, the integrated counts per microbunch due to K_L was found to be 0.14. Assuming the timing resolution to

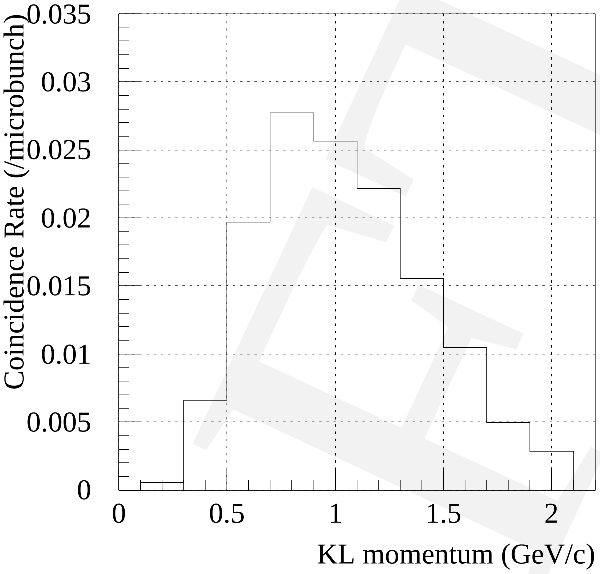

Fig. 72. Differential coincidence rate due to K_Ls.

be 2 nsec and a signal time window of 24 nsec[§], our final false veto probability is expected to be 1.8% and 1.2%, for neutrons and K_Ls, respectively. As for the beam photons, the coincidence count was obtained to be 0.06 per microbunch, but there is no harm because they always arrive at the catcher out of the signal time window; 2 ns faster than the fastest signal. Even in case of worse timing resolution, say 5 ns, the false veto probability can be safely neglected ($<$0.1%).

We also checked the singles rate for each photomultiplier. Here we assumed the threshold level was set to 1 photo-electron equivalent. The counting rates are 210k, 90k, and 90k Hz, respectively, due to neutrons, K_Ls and beam photons. The overall single rate, about 400 kHz, is small enough so that there should be no problem in operating the photomultipliers.

The real photon signal, which we want to catch and veto, might be hidden by these unwanted particles. In particular when they proceed right before the real signal, it will cause efficiency loss. We estimated this loss by the simulation assuming the double pulse resolution to be 10 ns using waveform digitizers. The efficiency loss by accidentals, defined as the probability of destroying all the (8,8) coincidences, was found to be 0.3% due to neutrons and/or K_Ls, and $<$0.1% due to the beam photons, respectively.

Optics

The catcher light collecting system consists of a parabolic mirror and a funnel. The parabolic mirror focuses Čerenkov light to the funnel input, and the funnel guides the light onto the photomultiplier's cathode. Each module is optically separated from adjacent ones

---

[§] The time window was calculated with the K_L momentum range of 0.4$<P_K<$1.3 GeV/c and the full decay region length. It was defined as the arrival time difference at the upstream face of the catcher.

by a very thin light reflecting wall made with an aluminized mylar sheet.

Figure 73 shows the light collection efficiency versus electron transverse track position in an aerogel slab. In this simulation, electrons were assumed to be at normal incidence to

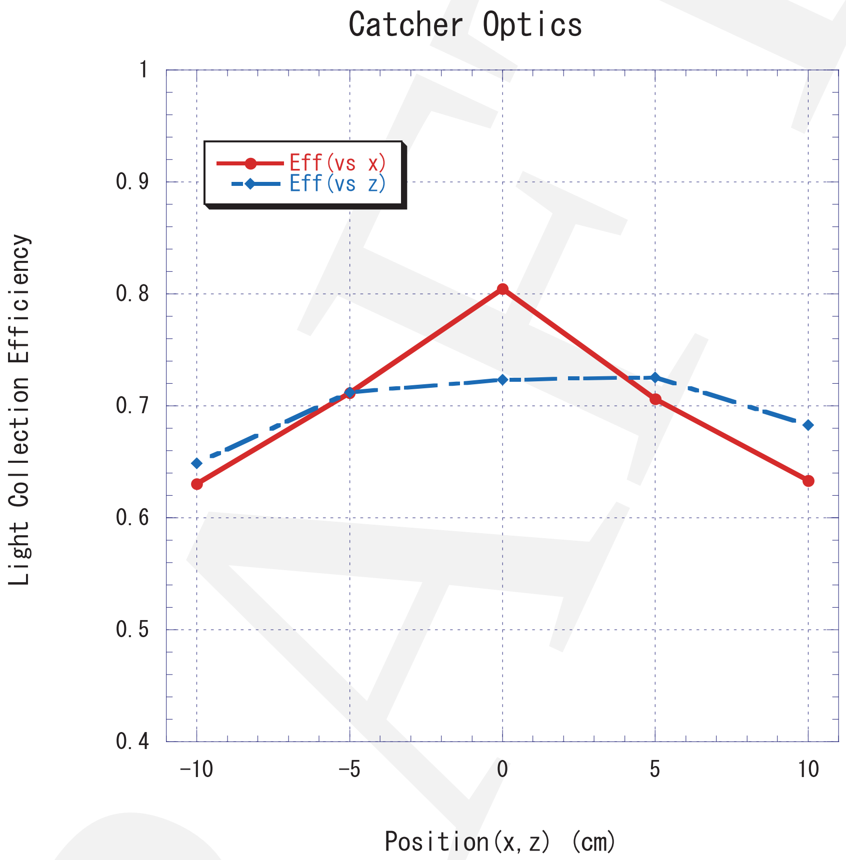

Fig. 73. Light collection efficiency as a function of incident position.

the aerogel, and the Čerenkov light produced uniformly along the path. Again, the expected number of photons from the aerogel was obtained from the result of the HERMES group. As to the reflectivity of the wall, parabolic mirrors, and the funnel surfaces, we used the measurement data taken for similar gas Čerenkov mirrors. The reflectivity is expected to be about 90% for the relevant wavelength. The overall light collection efficiency was found to be about 70%, giving about 13 photoelectrons for bialkali photocathodes for an electron.

We plan to make the mirrors with a 2 mm thick acrylic sheet shaped into a parabola by heat-pressing onto a mold. Its surface is coated with Al and MgF_2 by a vacuum evaporation method. The funnel will be made with a thin Al sheet pressed into a shape against a mold. Again its inner surface will be coated with Al and MgF_2.

We are currently building a full Monte Carlo simulation code, which combines the optics simulation package with GEANT3. Also under consideration is use of 3 in. tubes instead of 5 in. At present, the disadvantage of 3 in. tubes is light collection efficiency. If a better optics arrangement is found, we can reduce the costs without sacrificing efficiency.

$K_L \to \pi^0\pi^0$ Backgrounds in the Beam Catcher

As mentioned above, the main $K_L \to \pi^0\pi^0$ background that the catcher will detect comes from the odd-pairing photons. This fact can be utilized to establish the reliability of our experiment, i.e. understanding the $K_L \to \pi^0\pi^0$ backgrounds. Suppose we were to analyze the data without the catcher information. Then we would be left with 2-photon events contaminated with $K_L \to \pi^0\pi^0$ background even after all the kinematical cuts. For those events, we can predict the position and energy of the missing photon by interpreting the events as due to $K_L \to \pi^0\pi^0$ and by using kinematics for the odd-pairing. This can be done on an event-by-event basis, and can be compared with the actual data in the catcher. Fortunately, if the events are the genuine signal then the missing photon will not be directed toward the catcher. Figure 74 shows the reconstructed x-y distribution at the catcher position; the dots are the $K_L \to \pi^0\pi^0$ photons escaping through the beam hole and the boxes are the $K_L \to \pi^0\nu\bar{\nu}$ signals events interpreted as $K_L \to \pi^0\pi^0$ decays. As can be seen from the figure, the signal and background are well separated. If the predicted position is inside the catcher, we should find a photon near that position with the predicted energy. Thus, this check will provide a powerful way to test the overall performance of the experiment, and enhance its reliability greatly.

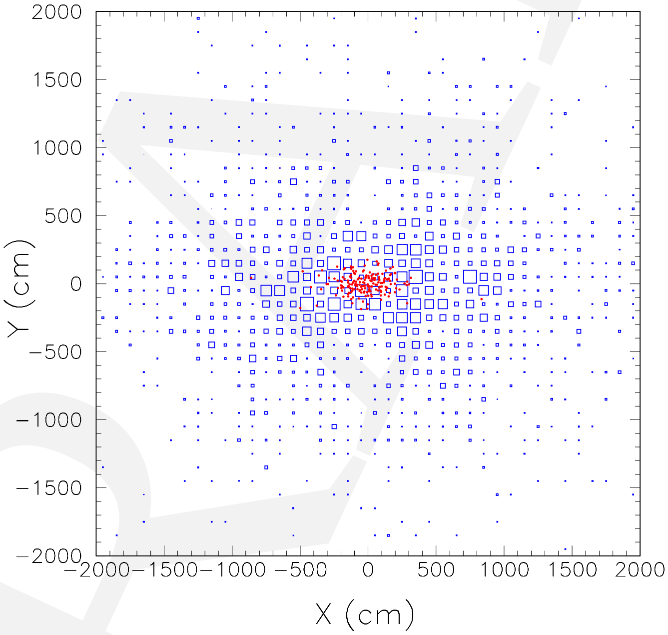

Fig. 74. Reconstructed x-y position at the catcher assuming $K_L \to \pi^0\pi^0$ odd pairing.

Summary

The design of the beam catcher based on an aerogel distributed Čerenkov counter has been well studied by Monte Carlo simulation and is found to meet the requirements for our experiment. It gives 98.5% efficiency for 300 MeV photons, while 0.2% efficiency for 0.8 GeV neutrons. In conclusion, we summarize the resultant parameters which are important to the experiment in Table 5.5.

Table 12. The summary of the resultant parameters.

photon efficiency	98.5%	at 300 MeV
	$\geq$ 99.5%	above 400 MeV
neutron efficiency	0.2%	at 0.8 GeV
false veto probability	1.8%	due to neutrons
	1.2%	due to K_Ls
	$<$0.1%	due to beam photons
singles rate	210 kHz	due to neutrons
	90 kHz	due to K_Ls
	90 kHz	due to beam photons
efficiency loss by accidentals	0.3%	due to neutrons and K_Ls
	$<$ 0.1%	due to beam photons

6 Trigger

To facilitate the accumulation of events needed for background studies, the KOPIO trigger will be kept reasonably loose. To keep pace with data pipelines, the Level 0 decision must be made in about 2 μs. The primary Level 0 trigger consists of four requirements:

1. Two and only two neutral clusters with $E > 50\,$MeV in the preradiator and calorimeter within $5\,$ns of each other. Fig. 75 shows the distribution of this time difference for all K_L^0 with two photons impinging on the preradiator.
2. No photon veto hits with energy $> 5\,$MeV within $\pm 5\,$ns of the average time of the candidate γ's. This includes only the photon vetoes surrounding the decay region
3. No hits within $\pm 5\,$ns of the average time of the candidate γ's in the main part of the charged particle veto system.
4. No hits with energy $> 5\,$MeV in the beam region of the upstream photon veto in a $\pm 3\,$ns window around a time $15\,$ns earlier than the average time of the γ candidates. This condition removes events originating upstream of the decay region.

These conditions are sufficient to reduce the Level 0 trigger rate to 7.3 kHz (*i.e.* 20k triggers over the 2.4 second spill). Fig. 76 shows the dependence of this rate on the time window imposed in conditions 2 and 3 above. Table 13 shows the dependence of the significant individual components of the trigger rate on this time window. Triggers from other kaon decays and from neutron or K_L interactions are much less important than the ones listed.

Table 13. Trigger rates (in KHz) due to K_L^0 decay modes as a function of the veto window width. The main components of the trigger rate are shown individually.

Component	3ns	5ns	7.5 ns	10ns	15 ns
$K_L^0 \to \pi^0\pi^0$	0.41	0.16	0.03	0.01	0.01
$K_L^0 \to \gamma\gamma$	0.77	0.65	0.60	0.60	0.56
$K_L^0 \to \pi^0\pi^0\pi^0$	25.46	4.65	0.72	0.59	0.56
$K_L^0 \to \pi^+\pi^-\pi^0$	9.59	1.83	0.95	0.70	0.62
All	36.27	7.31	2.31	1.90	1.77

The scheme for implementing this trigger in a pipelined manner is currently under development. The aim is to achieve a trigger efficiency of better than 95%. The details depend on the configuration of scintillators in the preradiator. The common requirement of the schemes under consideration is that there be at least one x and one y determination per preradiator module. A module includes 8 scintillator planes. The following option is based on 20 cm strips in x and y only (yielding 12 strips in each plane of each quadrant). There would be four successive scintillator planes with the same orientation. The strips would be grouped longitudinally into phototubes for readout (*i.e.* twelve phototubes read out four successive

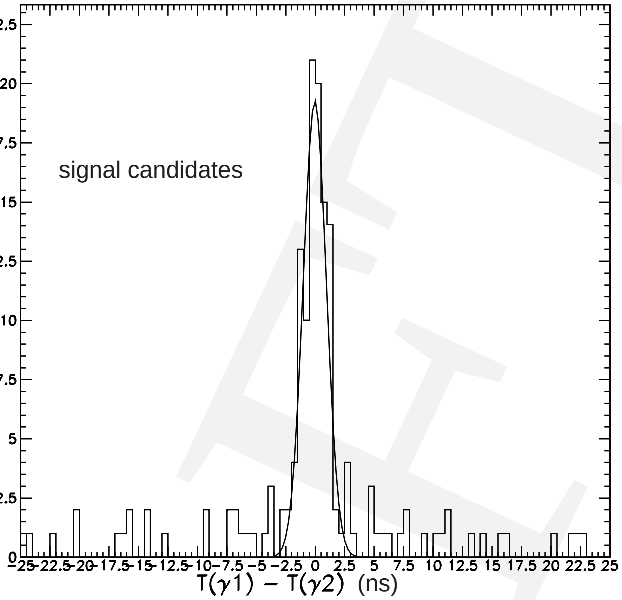

Fig. 75. Time difference between two photons in the preradiator. All decays which result in two photons in the preradiator and which pass the veto requirement are included.

planes of scintillator in one quadrant). The four successive x-planes would alternate with four y-planes (xxxxyyyyxxxxyyyy...). For initial Level 0 purposes the pulse height of all x planes and all y planes would be summed longitudinally. There are a total of 64 scintillator planes, so that in this scheme the number of separately read out layers is 16. Calorimeter elements would be summed to approximately match the preradiator projections and added to the longitudinal sums as appropriate. Strip sums are digitized by pipelined FADCs. GEANT simulation indicates that requiring that the projection with the higher number of clusters has 2 or 3 clusters and the other projection has no more than 2 clusters is $> 98\%$ efficient for reconstructible $K_L \to \pi^0\nu\bar{\nu}$ events. These conditions will be imposed via an FPGA with access to the FADC memories.

For events passing the above criteria, in each quadrant the strip sums are discriminated and all possible x and y coincidences are made (*i.e.* 144 for each quadrant in this scheme). The inputs to these coincidences are delayed so as to compensate for light propagation in the strips. This assures that all valid x-y coincidences from a given event will be mutually coincident. Nearest neighbor vetoing will result in one time per valid cluster, which can then be used for establishing coincidences between clusters. The clustering will be extended across quadrant boundaries. Two and three clusters will be allowed at this point. We are presently assuming a coincidence window of 5 ns, although relaxing this does not incur much of an increase in the rate as can be seen from Fig. 75. The coincidence and clustering logic will be done in FPGAs. These will also determine the members of each cluster so that the appropriate energies can be interrogated, summed and the cluster energy threshold imposed. At this point events with three clusters are prescaled and the Level 0 two-cluster

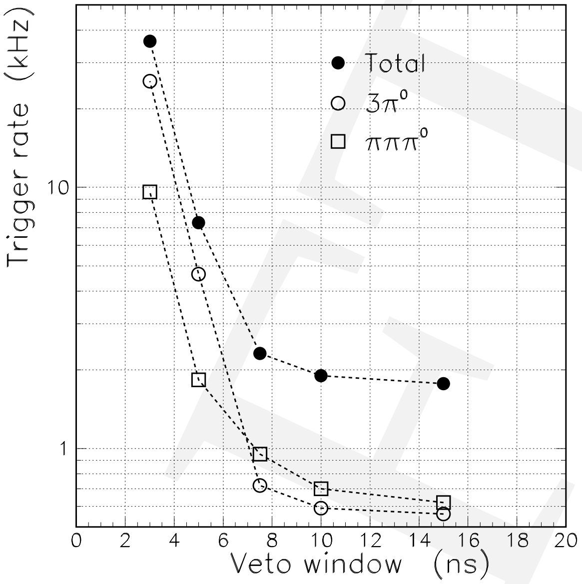

Fig. 76. Trigger rate versus veto window width. Window center is defined as the average time of the two candidate signal gammas. Window width is half the veto overlap interval. Major components of the trigger rate are shown as well as the total.

requirement imposed.

Veto signals which have been discriminated, meantimed and summed with appropriate delays are put in anticoincidence with the coincident cluster output. As seen in Fig. 76, the resultant rate can be tuned by adjusting the veto window. In the region of 10 ns total overlap width where we are planning to work, the trigger efficiency is reduced by only about 1% for each 1 ns increase in the veto overlap width.

In parallel, sums of all strips in each layer of each quadrant are formed and discriminated. These are put in loose coincidence with the cluster coincidence output of L0 accepted events to determine the upstream-most excited layer in each quadrant. This information plays no part in rejecting events but is used to reduce the data load from the preradiator chambers.

The DAQ is designed to accept a Level 0 rate of 25 kHz. The trigger described above should result in a rate of approximately 10 kHz. The residual will be used to accept calibration and triggers for collecting decays other than $K_L^0 \to \pi^0\nu\bar{\nu}$.

Provision will be made for a Level 1 trigger with a latency of 50 μs which will be developed if further study shows it to be necessary.

The Level 2 trigger will be resident in a farm of commodity processors. The algorithms are not yet fully developed, but the goal is to reduce the data written on tape by an order of magnitude. The information available to do this includes the two-photon effective mass, the photon energy asymmetry, the reconstructed vertex, the K_L time of flight, the downstream and catcher veto times and pulse heights, etc. Fig. 77 shows the z vs $m_{\gamma\gamma}$ distribution for events passing the Level 0 trigger. Loose cuts on the these quantities alone reject about 2/3 of the Level 0 events. A good idea of the rejection factor achievable by correcting for photon

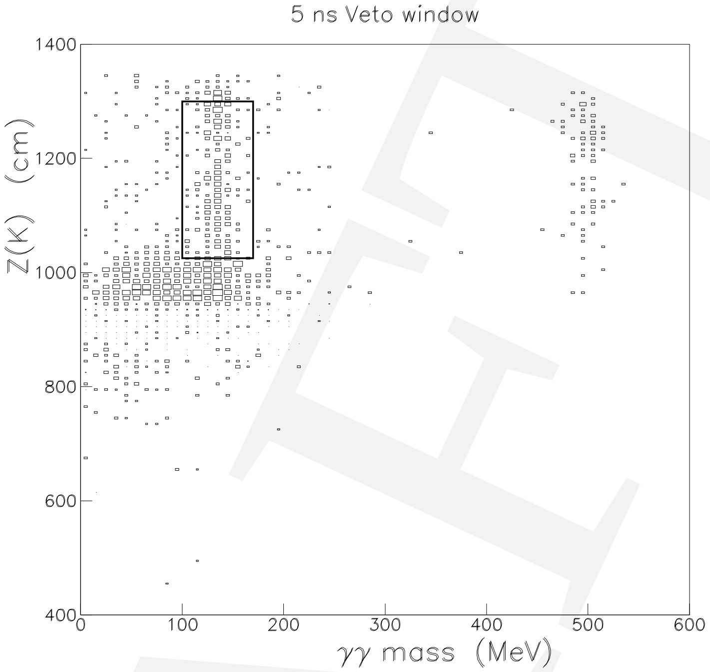

Fig. 77. Z-vertex distribution vs $m_{\gamma\gamma}$ for two-photon events accepted by Level 0. Box shows approximate region to be accepted by Level 2.

flight path can be obtained from Fig. 76 or Table 13. Correcting for the photon time-of-flight and reimposing the veto overlap will be very similar to the effect of widening the uncorrected veto window. *i.e.*, the rejection ratio will be $\sim 2/7$. Imposing approximate vertex matching between the two photons rejects $\sim 25\%$ of the residual events. The product of these factors yields the required order of magnitude suppression of two-photon triggers.

7 Data Acquisition

Overview

To cope with uncertainties in the trigger rate and the data size, the DAQ system has been designed to be able to handle a data throughput such that anything larger would likely be too costly to analyze offline. A functional block diagram of the DAQ system is shown in Fig. 78.

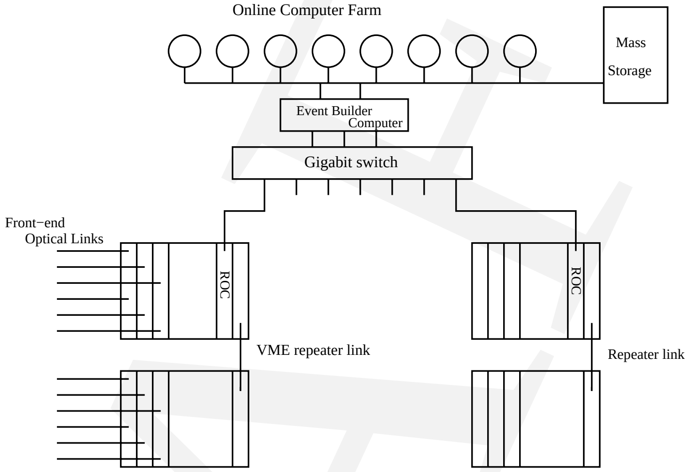

Fig. 78. Block diagram of the DAQ system.

The front-end electronics consists of the following:

- ∼80,000 channels of TDC information from the anode wires of the preradiator chambers. These are located on ~ 800 boards (96 channels per board) attached to the chambers.
- ∼65,000 channels of ADC information from the cathode strips of the preradiator chambers. Similar to the anodes, these are located on ~ 600 boards attached to the chambers.
- ∼5000 channels from phototubes. How these will be digitized is under development(see Sec. 5.2.7), but it is anticipated that they will present the same interface to the higher-level readout electronics as the preradiator front-end.

Data from the preradiator, the calorimeter and the charged particle veto are sent via a separate path to the trigger system. Upon a level-0 accept from the trigger, the digitized data from the front-end are transferred via optical links (96 channels per link) to VME memory modules. These memory modules hold the events from one given spill, where each spill is expected to be about 2.4 sec long. In the inter-spill (2.3 sec), the memories are read out by commercial processors and the spill fragments are passed via gigabit ethernet through an unmanaged switch into a computer which builds the events and distributes them to consumers (e.g. data logger, monitoring tasks and so on). The possibility is left open for data reduction by an offline computer farm before the events are logged to tape.

The data rate was estimated based on the number of photons in each event passing the trigger. Table 14 summarizes the average data produced by a single photon in each detector subsystem, obtained from a GEANT simulation. Each preradiator chamber hit consists of one anode wire and 5 cathode strips, generating 24 bytes of data. For the preradiator scintillator phototubes, it was assumed that the pulses would be transient digitized at 500 MHz for 50 ns[¶], leading to 25 8-bit samples, or 30 bytes per phototube including overhead. The remaining phototube systems are expected to be digitized by electronics similar to that for the preradiator chambers, generating 8 bytes of data per phototube (4 bytes each for time and energy). Veto counters are expected to contribute ~ 50 hits (400 bytes) per event.

Table 14. Average data produced by a single photon.

Subdetector	No. hits/γ	Data/hit (bytes)	Data/γ (bytes)
Prerad chambers	50	24	1200
Prerad scint	3	30	90
Calorimeter	9	8	72
All			1362

Simulations of the trigger rate indicate a maximum rate of around 75000 triggers per 3 sec spill (nominal value 2.3 sec) with the majority of triggers coming from K_L decays. To estimate the data load, we assume the worst case where all the decays produce 6 photons in the detector; this leads to a data size of ~ 8.6 kbytes per event. The data load for each detector subsystem is shown in Table 15.

Table 15. Expected data load for each detector sub-system, assuming 6 photons per trigger. The exact breakdown by sub-system of the number of optional links for the PMT-based systems is not known; the total number of such links is expected to be around 50.

Subsystem	No. of links	Data per spill (Mbyte)
Prerad cathode	800	450
Prerad anode	600	90
Prerad scint		41
Calorimeter		32
Veto systems		30
Total		643

[¶] This is a worse case assumption for design purposes. The nominal system is as described in sec. 5.2.7.

Front-end electronics

The front-end electronics for the preradiator chambers are mounted on the chambers. The digitization of the analog signals has been discussed in the preradiator section. From the point of view of the higher-level readout electronics, the front-end appears as a large number of optical links, with each link providing the data (serially) from 96 front-end channels. There will be approximately 600 optical links from the preradiator cathodes and 800 links from the anodes. The data load per link is estimated to be 750kB/link/spill (120kB/link/spill) for the cathodes (anodes). This is far below the capacity of existing optical links; in fact, the main motivation for using optical links here is not so much for their speed as for their low power consumption.

For our purposes here, we assume a multiplexing for the phototube-based systems similar to the preradiator chamber electronics of ~ 100 front-end channels into optical links. Anticipating about 5000 phototube channels, this comes out to 50 links and a data load per link of 2.1MB/link/spill.

Intermediate buffer

Approximately 10 VME 9U crates will be used to house the buffer memory modules which hold the data from a given spill.

Memory modules

The memory modules receive the optical signals from the front-end electronics, de-serialize them, and put the data into on-board dual-ported memory which can then be accessed (simultaneously) via the VME backplane. Several examples of such boards already exist in the community[1] and we do not expect problems building boards suited to our needs. Current candidates for the on-board hardware include the Finisar FRM-1311-2 fiber optic receiver, the HP HDMP-1024 de-serializer, and the IDT 70V7xxx series of dual-ported memory. 10 optical receivers should fit on a 9U front panel, implying approximately 60 (80) boards for the preradiator cathode (anode) systems. To accommodate an average data load of 750kB/channel/spill (120kB/channel/spill) for the preradiator cathodes (anodes), the memory depth per channel should be about 1.5MB/channel (240kB/channel) for the cathodes (anodes). The phototube systems would require about 4MB/channel.

VME crate controller

The main function of the VME crate controller will be to read out the buffer memories in the crate and send the data to the event builder switch via an ethernet link. In addition, there would be an opportunity to reduce the data size. In the preradiator, for example, one might need to keep only the data in the immediate vicinity of where the shower starts. Commercial VME controllers will serve these purposes. In E787/E949 we have extensive experience with Motorola MVME2300 and 2600 series of controllers running vxWorks; presumably even faster versions of these controllers will be available by the time KOPIO starts. Each controller will be equipped with a gigabit ethernet interface, which already is available commercially. The 140 preradiator chamber modules would be distributed in 9 crates; the data load per crate is expected to be around 60MB/spill/crate. The remaining systems would fill another crate and hold about 100 MB/spill. Given the speed of gigabit ethernet interfaces, it might be cost effective to multiplex the preradiator anode and cathode crates with commercially available VME repeater links. Thus, for the 9 preradiator crates, 5 controllers and 4 repeaters will be needed; an additional controller will be used for the phototube-based systems.

Event builder

The event builder will consist of an unmanaged switch with 12 ports. The inputs to the switch will be the ethernet links from the VME controllers in the buffer crates. The output of the switch will go to the event building computer where the event fragments will be combined via software. Gigabit switches are available today at reasonable cost. Similarly we expect a suitable event building computer to be available at reasonable cost.

Online computer farm

It is likely that we will not want to write 650MB/spill to permanent storage,[‖] although it is not unthinkable given the data sizes being discussed for the LHC and RHIC experiments. Thus, some kind of data reduction will be desired before going to tape. Farms of low-cost processors connected via a gigabit ethernet link are common in the community. Assuming a processing time of 1ms/event/CPU, a modest farm of 15 CPU's would suffice to process 75000 events every 5 seconds.

Online software

We will need software for event distribution, data logging, overall run control and data monitoring. There is no overall design at present, but we do not anticipate any problems to have a system ready in time for the start of KOPIO.

Slow control

Most of the equipment part of the detector will require constant control and monitoring in order to guarantee proper functionality over the experiment period. The monitoring aspect will include, temperatures, gas flow, gas mixture, voltages, currents, calibration parameters, threshold settings, mechanical position of objects, warnings, and alarms. The control aspect of the system will include the configuration of the devices such as trigger algorithms, test pulse configuration, gas flow settings, power distribution, safety alarms settings, etc. This system (SC) will run independently of the main data acquisition system with its own data bus and data collector. The Slow Control Board (SCB) will be flexible enough to accommodate the diversity of hardware implemented in the KOPIO setup. In order to address this requirement, we have opted to use a commercial micro-controller as the core processor of the slow control system. This processor will carry the dedicated software for servicing the particular client board functionalities. The communication protocol for linking these SCBs is based on a multi-drop serial bus, which links several SCB nodes to a SCB supervisor independent of the main DAQ. This SCB supervisor will be able to exchange information to the

---

[‖] For a 10^7 sec year, this would give 1300 TB.

main DAQ in order to incorporate information status to the main data logger as well as take orders from the data analyzer monitoring the incoming physics event. The current candidates for the micro-controller are based on the MCS-51 instruction set, which is a well-established standard in industry. Hardware from Cygnal: C8051Fxxxx, and Analog Device: ADuC812. (Fig C8051Fxx.png, Aduc812.png) are being considered. The SCB will be composed of the micro-controller, memory expansions and bus interface chip. All the Input/Output lines will be programmed by software.

8 Background and Sensitivity

8.1 Background Rejection

Photon veto

High detection efficiencies for additional photons and charged particles are the primary defenses against backgrounds in the $K_L^0 \to \pi^0\nu\bar{\nu}$ measurement. However, there are barriers to achieving unlimited efficiency such as photo-nuclear interactions in which the photon energy is transferred entirely to neutrons to which we are mostly blind. In the following we deal with the limits of photon detection efficiency, the KOPIO kinematic method of suppressing the most dangerous background with extra photons due to $K_L^0 \to \pi^0\pi^0$, and the problems of photons escaping detection in beam holes and within the showers of other photons.

Charged particle detection efficiencies are relevant to the suppression of backgrounds like $K_{e3\gamma}$ and $K_L^0 \to \pi^+\pi^-\pi^0$. The detection efficiency for pions and electrons will be discussed in the context of the background estimates for these modes presented in the next section.

Photon Detection Efficiency

E787 has achieved a π^0 detection inefficiency of $< 10^{-6}$ for 200 MeV/c π^0 decays which yield photons between 20 and 225 MeV. The detector employs lead/scintillator calorimetry similar to that proposed for KOPIO. The central E787 photon detector consisted of about 1 radiation length (X_0) of plastic scintillator (range stack) followed by multiple layers of 1 mm thick lead and 5 mm thick scintillator (barrel veto) for a total of about 15 X_0. The greatest inefficiency, 1%, occurs for photon energies ≤ 20 MeV due to sampling fluctuations. The inefficiency for higher energy photons was 10^{-4} and appeared to be limited by sampling fluctuations, shower escape and photo-nuclear reactions which may be contributing at comparable levels.

Progress on the limits of photon detection has been made in a beam test at INS (Japan)[1] where the efficiency for detection of photon-induced events with photo-nuclear interactions (i.e. those in which soft neutrons were also detected) was made in the energy range from 185 MeV to 1 GeV. Single photon inefficiencies as low as 10^{-6} for 1 GeV photons could be inferred from these measurements under the assumption that no events occur in which high energy neutrons carry off all the missing energy. If this assumption were valid, the efficiencies quoted below for higher energy photons would be considerably improved with the consequences of much reduced backgrounds and higher acceptance for KOPIO. However, in order to determine the true photon veto inefficiency at higher energies than covered by E787, construction of a full 4π spectrometer like that needed for a $K \to \pi\nu\bar{\nu}$ experiment will be required. Thus, due to the uncertainties in the validity of the inefficiencies inferred in Ref.[1], we will use the levels already demonstrated by E787 in our estimates below. Uncertainties in the level of photon detection efficiency achievable are actually largest for the region $E_\gamma \leq 20$ MeV which is preferentially populated by higher energy π^0 decays due to Lorentz boosting. For these photons, the detection efficiency is minimal at best and additional measures must be taken.

Suppression of photons in $K_L^0 \to \pi^0\pi^0$ decays

In order to fully suppress $K_L^0 \to \pi^0\pi^0$ backgrounds, a π^0 detection inefficiency of 10^{-8} is required. This is a realistic goal in KOPIO where both "missing" photons from $K_L^0 \to \pi^0\pi^0$ decay can be required to be in the higher energy range of the E787 measurements because we have kinematic handles available to suppress those configurations with low energy missing photons.

Some improvements in the photon detection inefficiency for lower energy photons may also be possible (until the photo-nuclear limit is reached) by using a finer sampling calorimeter, especially at the front of the barrel veto. The photon detection efficiency for higher energy photons may also be improved by a small factor by implementing more radiation lengths to block remaining shower escape. In the KOPIO experiment, we will increase the average thickness to 18 X_0. Figure 79 shows the photon detection inefficiency assumed in KOPIO background estimates.

Due to the requirement of a single K_L^0 decay per micro-bunch in the KOPIO decay volume, accidental losses associated with photon vetoing are expected to be small.[**]

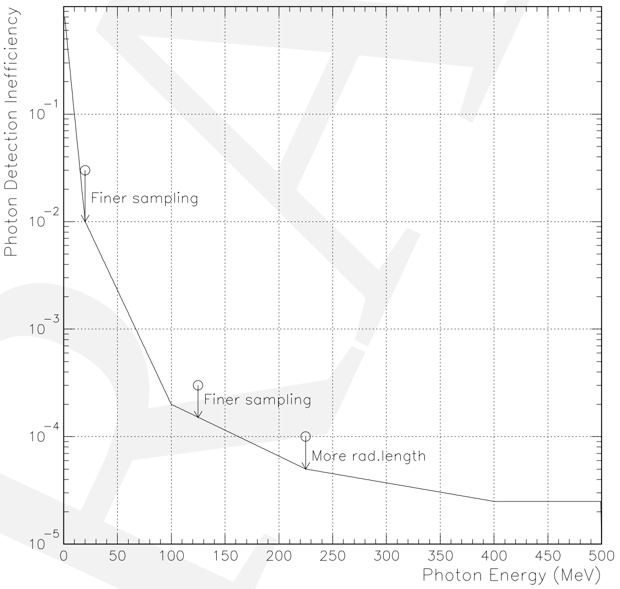

Fig. 79. Photon detection inefficiency used in this proposal(solid line). The open circles are the E787 results.

Photon loss in beam holes and within overlapping showers.

One hundred million events were generated to study the effect of the beam holes. Backgrounds due to photons escaping towards the upstream beam hole were found to be negligi-

---

[**] The single decay per micro-bunch provides a quieter environment than found in E787 where the photon veto accidental losses were in the neighborhood of 20%.

ble. However, the photons exiting towards the downstream beam hole were found to cause significant backgrounds if not dealt with. The primary defense against this effect is the system of downstream photon detectors, in particular, the catcher described above.

Figure 65 shows the energy distribution of $K_L^0 \to \pi^0\pi^0$ photons hitting the catcher. The $K_L^0 \to \pi^0\pi^0$ background is dominated by the odd pairing case with energies above 300 MeV. Having a detector which is 99% efficient for photon energies above 300 MeV is sufficient to bring events exiting through the beam hole under control. At a 300 MeV threshold, we expect accidental losses due to the catcher to be $\sim 3\%$ as described above.

Although the detection of decay photons traveling out the beam hole seems feasible with the present catcher design, the KOPIO experiment could even proceed without such a detector. As indicated above, we use kinematics to reconstruct the direction and energy of missing $K_L^0 \to \pi^0\pi^0$ photons in order to eliminate potential background events.

Photons can also hide in the showers of other detected photons but we expect that the consequent inefficiency will be smaller than the effects described above. These overlapping photons occur a few per cent of the time in $K_L^0 \to \pi^0\pi^0$ events for distances between the two photons at the calorimeter less than 50 cm (about 6 Moliere radii). For separation distances ≤ 20 cm, the probability is $< 1\%$ for $K_L^0 \to \pi^0\pi^0$ decays. When the distance between two photons is between 20 and 50 cm, we identify the overlapping photons by comparing the shower center of gravity in the calorimeter (position resolution $\sigma \sim 3$ cm) to the expected position from the preradiator. With an estimated inefficiency of 10^{-3} for the center of gravity method and including the probability of the conversion of the extra photon in the preradiator, the inefficiency due to overlapping photons is 10^{-5}. When the separation is less than 20 cm and the overlapping photons merge, the invariant mass of the photons becomes much larger than the π^0 mass and the missing energy and mass are small. The inefficiency of this invariant mass cut is limited by the photonuclear reaction probability (a few times 10^{-3}) of the overlapped photon. Again, taking into account the photon non-conversion probability, the photon detection inefficiency due to overlap in the region of separation < 20 cm is also estimated to be 10^{-5}. We have also found that the loss of acceptance due to cuts aimed at eliminating overlapping photons is only a few percent.

Background Estimates

Methodology

The energy and direction measurements of photons by the KOPIO preradiator/calorimeter arrangement along with momentum tagging of the K_L^0 by time-of-flight provide powerful kinematic constraints for suppressing backgrounds. Among the most effective constraints are the mass of the two photons ($m_{\gamma\gamma}$), and energy of the π^0 in the K_L^0 rest frame ($E^*_{\pi^0}$). Vertex restrictions from photon tracking help in rejecting accidentals and particles produced near the surface of the detector by the beam halo. The tight vertical collimation of the beam reduces the beam halo and provides an extra vertex constraint. In the horizontal direction, we apply tighter cuts on the photon reconstruction algorithms to suppress backgrounds. In addition, we construct constraints to avoid backgrounds coming from earlier timing micro-bunches and require that there was only one K_L^0 decay in the micro-bunch of interest for $K_L^0 \to \pi^0\nu\bar{\nu}$ candidates. The 4π coverage of the photon veto ($\overline{\gamma}$) and charged particle veto

($\overline{charge}$) is effective in suppressing other K_L^0 decays. The entire decay volume is evacuated to suppress production of particles in the decay region. Since the KOPIO technique provides extensive information on each decay mode, we expect to be able to use data to accurately measure the levels of backgrounds.

In addition to $K_L^0 \to \pi^0\pi^0$ decays, potential sources of background include neutron production of π^0's in the fiducial region vacuum, other K_L^0 decays like $K_{\pi 3}$, K_{e3}, $K_{e3\gamma}$ and $K_L^0 \to \gamma\gamma$ and $\Lambda \to n\pi^0$ decays. Suppression of most backgrounds is accomplished by the high efficiency hermetic photon detector along with kinematic constraints. In the following, we discuss the nominal background levels anticipated for each of the potential sources for the entire proposed exposure.

$\boldsymbol{K_L^0 \to \pi^0\pi^0}$

The dominant background $K_L^0 \to \pi^0\pi^0$ has a branching ratio of 9×10^{-4}. In the $K_L^0 \to \pi^0\pi^0$ background studies, each Monte Carlo event was weighted with an energy dependent veto efficiency and a photon direction reconstruction efficiency in order to study the rejection and acceptance. The kinematic information was primarily used to suppress $K_L^0 \to \pi^0\pi^0$ background through the use of a cut on the pion c.m. energy $E^*_{\pi^0}$ for the even pairing background events, and a cut on the reconstructed pion mass $m_{\gamma\gamma}$ for odd pairing background events. The full kinematic information was found to allow a range of $K_L^0 \to \pi^0\pi^0$ rejections and treatment of rare pathologies such as bucket-to-bucket wrap-around events and events in which photons escape through the beam hole. These constraints were also found to be effective in the simulations for suppressing other decay modes such as $K_{\pi 3}$ and K_{e3} decay modes discussed below.

Dealing with low energy $K_L^0 \to \pi^0\pi^0$ photons (where the inefficiency is greatest) is particularly important. The energy of the missing photons in $K_L^0 \to \pi^0\pi^0$ events can be obtained by subtracting the measured energies of the two observed photons from the K_L^0 energy. Requiring significant total missing energy (i.e. ($E_K - E_{\gamma 1} - E_{\gamma 2}$)) as is generally the case for $K_L^0 \to \pi^0\nu\bar{\nu}$ events suppresses most potential background events that contain lower energy missing photons. However, in unusual cases when one of the missing photons has very high energy and one has very low energy an additional cut on missing mass (i.e. $\sqrt{(E_K - E_{\gamma 1} - E_{\gamma 2})^2 - (\mathbf{P_K} - \mathbf{P}_{\gamma 1} - \mathbf{P}_{\gamma 2})^2}$) is effective. Because the missing mass in $K_L^0 \to \pi^0\pi^0$ events is proportional to $\sqrt{E_{miss1} * E_{miss2}}$, where E_{miss} is the energy of a missing photon, the missing mass also becomes small for the case of asymmetric energy sharing. Figure 80 shows the missing mass vs. missing energy distribution of photons for $K_L^0 \to \pi^0\pi^0$ and $K_L^0 \to \pi^0\nu\bar{\nu}$ events. After removing the low missing mass and low missing energy region, we can suppress the low energy photons to achieve 10^{-8} overall detection inefficiency for the two missing photons in $K^0_{\pi 2}$ events.

The effect of eliminating events with small missing mass can be seen more directly by comparing $E^*_{\pi^0}$ distributions before and after the photon veto cut for the $K_L^0 \to \pi^0\pi^0$ odd background events where one photon from each π^0 is missed (Figure 81). The peak above $E^*_{\pi^0}$=230 MeV after the photon veto cut corresponds to the small missing mass region [††].

[††] $E^*_{\pi^0}$ is related to missing mass: $E^*_{\pi^0} = \frac{m_K^2 + m_{\pi^0}^2 - m_{miss}^2}{2m_K}$. For small missing mass, $E^*_{\pi^0}$ is large.

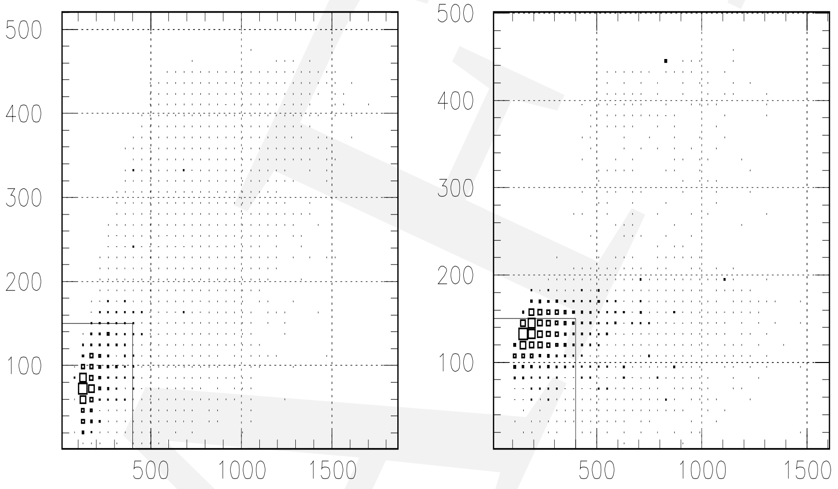

Miss−Mass vs. Miss−E (Kpi2−odd)

Miss−Mass vs. Miss−E (Kpi2−even)

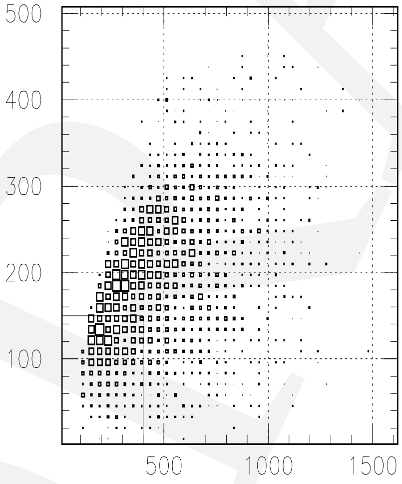

Miss−Mass vs. Miss−E (pinn)

Fig. 80. Missing mass vs. missing energy distribution of photons for $K_L^0 \to \pi^0\pi^0$ odd, $K_L^0 \to \pi^0\pi^0$ even and $K_L^0 \to \pi^0\nu\bar{\nu}$ events.

This is one of the main reasons why the phase space below the $K_L^0 \to \pi^0\pi^0$ peak, $E^*_{\pi^0} < 249$ MeV, is used for the KOPIO measurement.

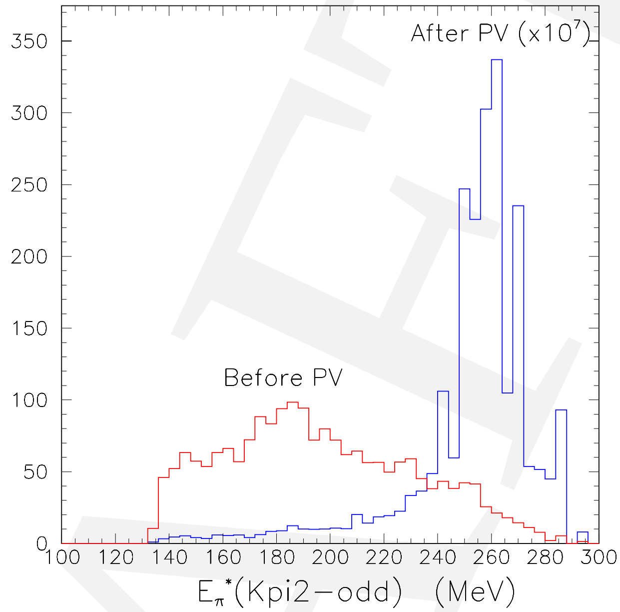

Fig. 81. π^0 energy distribution in the K_L^0 center of mass system ($E^*_{\pi^0}$) for $K_L^0 \to \pi^0\pi^0$ odd events before and after photon veto cuts.

The $K_L^0 \to \pi^0\pi^0$ even background arising from the previous timing micro-bunch ("wrap-around" events) can cause a serious problem because the E^*_π cut as well as the missing energy cut to suppress low energy missing photons may fail. Figure 82 shows E^*_π assuming that the particle is coming from the previous bunch versus the longitudinal π^0 momentum of the signal and the wrap-around $K_L^0 \to \pi^0\pi^0$ background. This background is suppressed by cutting on these quantities as indicated in the figure.

Table 16 gives the estimated acceptance factors for the $K_L^0 \to \pi^0\pi^0$ backgrounds, including all combinations of 2 missing photons out of the 4 photons when both observed photons convert in the preradiator. Multiplying the total $K_L^0 \to \pi^0\pi^0$ acceptance by the branching ratio and the number of K_L^0 decays, we expect 10.7 events from this source split evenly the between the odd and even pairing types. When we include those cases where one photon converts in the preradiator and one in the calorimeter, and account for accidental losses (see below) the total $K_L^0 \to \pi^0\pi^0$ background expected is 12.8 events.

$K_L^0 \to \pi^+\pi^-\pi^0$

Since the $K_{\pi3}$ decay contains a π^0 in the lower momentum range of $K_L^0 \to \pi^0\nu\bar{\nu}$, this mode is suppressed by a combination of charged particle vetoes and additional c.m. energy cuts (E^*_π). Charged pions can disappear by detector inefficiency (e.g. insufficient light output from the charged veto scintillators) or via nuclear interactions.

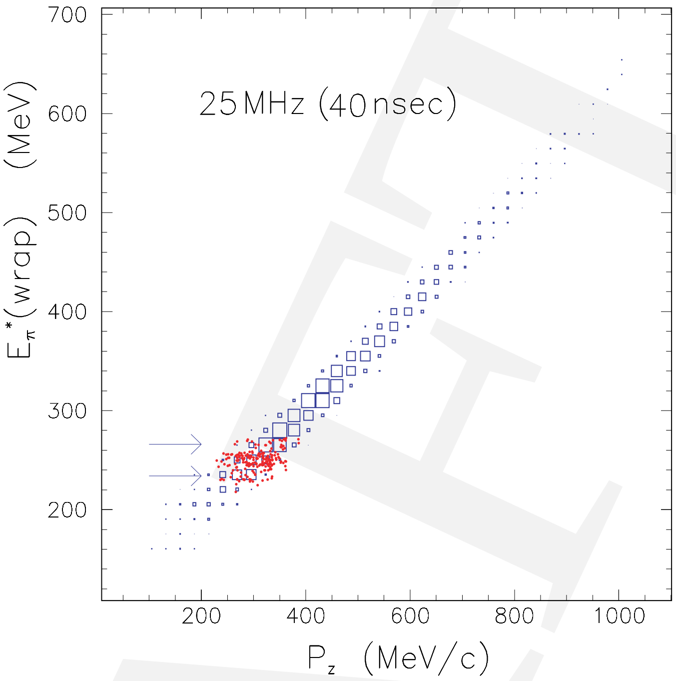

Fig. 82. E^*_π assuming that the particle is coming from the previous bunch versus longitudinal π^0 momentum for the signal (boxes) and background events from wrap-around $K^0_L \rightarrow \pi^0\pi^0$ (even) decays (dots). The arrows indicate the cut values use to suppress the background.

Using 1 cm thick plastic scintillation counters and a threshold of 1 MeV, Inagaki et al.[2] found inefficiencies for 1 GeV/c particles to be 3.2×10^{-4} for e^+, 6×10^{-4} for π^-, $< 1.6 \times 10^{-5}$ for π^+ and $< 1.3 \times 10^{-4}$ for e^-. In KOPIO, when the π^- reacts via charge exchange $\pi^- p \rightarrow \pi^0 n$ or $\pi^- p \rightarrow \gamma n$ before being detected by the charged particle veto system, photon energy will be present elsewhere to reduce the overall inefficiency. However, the influence of the $\Delta(1232)$ resonance causes the interaction cross sections for pions to be large at KOPIO energies. Ultimately, pion reactions producing only neutrons will represent an irreducible level of efficiency. In order to make estimates for such processes, we have employed cross section measurements[3] on reactions of the type $\pi^+ + C \rightarrow p + p$ in the energy region appropriate for KOPIO and, assuming isospin symmetry, obtain values for $\pi^- + C \rightarrow n + n$ reactions (including those with larger numbers of neutrons). Then, taking into account the measurements of Inagaki et al. mentioned above, we estimated the overall charged pion inefficiencies for the $K_{\pi 3}$ background to be $\leq 10^{-4}$ for π^- and $\leq 10^{-5}$ for π^+ resulting in a suppression factor of $\leq 10^{-9}$.

The unusual case where a π^+ gets a very small energy and stops in a veto counter without depositing much energy is potentially problematic because the charged veto rejection for π^+ is not available. However, these events are concentrated in a particular phase space region in $E^*_{\pi^0}$ vs. missing energy as shown in Fig. 83 and can easily be rejected with little acceptance loss.

Figure 84 shows a plot of $E^*_{\pi^0}$ vs. $|E^*_{\gamma 1} - E^*_{\gamma 2}|$ for the $K_{\pi 3}$ background. A cut in $E^*_{\pi^0} <$

Table 16. Acceptance factors for the $K_L^0 \to \pi^0\pi^0$ even and odd pairing backgrounds (two photons converting in the preradiator).

Requirement	Even Pairing	Odd Pairing
No. γ Combinations	2	4
Z fiducial region and P_K	0.46	0.47
Solid angle	0.29	0.23
Preradiator Conversion Probability	0.50	0.51
$m_{\gamma\gamma} = m_\pi$	0.71	0.08
E_π^*	0.009	0.22
Wrap-$K_{\pi 3}$ low energy	0.76	0.83
Photon veto	1.0×10^{-7}	2.6×10^{-8}
E_π^* vs. $\lvert E_{\gamma 1}^* - E_{\gamma 2}^* \rvert$	0.73	0.41
Acceptance	4.6×10^{-11}	3.4×10^{-11}
Total $K_L^0 \to \pi^0\pi^0$ Acceptance	8.0×10^{-11}	

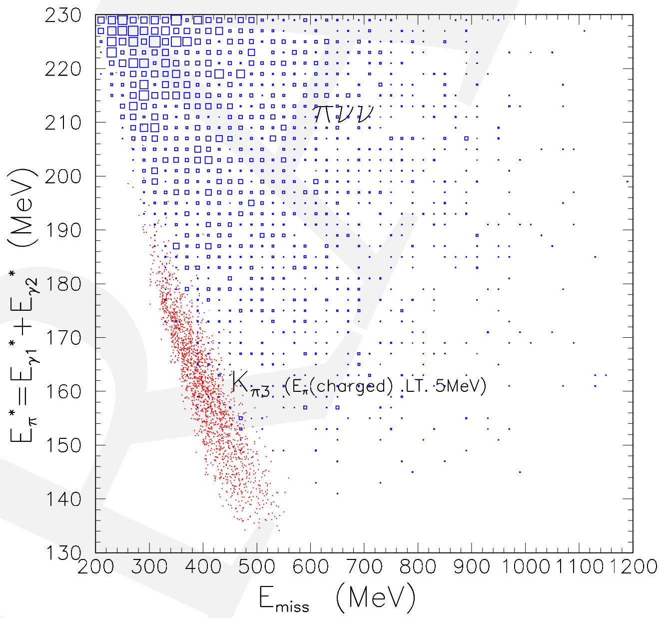

Fig. 83. $E_{\pi^0}^*$ versus missing energy for the $K_{\pi 3}$ background when π^+ kinetic energy is less than 5MeV.

190 MeV is very effective, and is compatible with the odd pairing cuts. Putting all the cuts together gives an estimated 0.65 events from $K_{\pi 3}$.

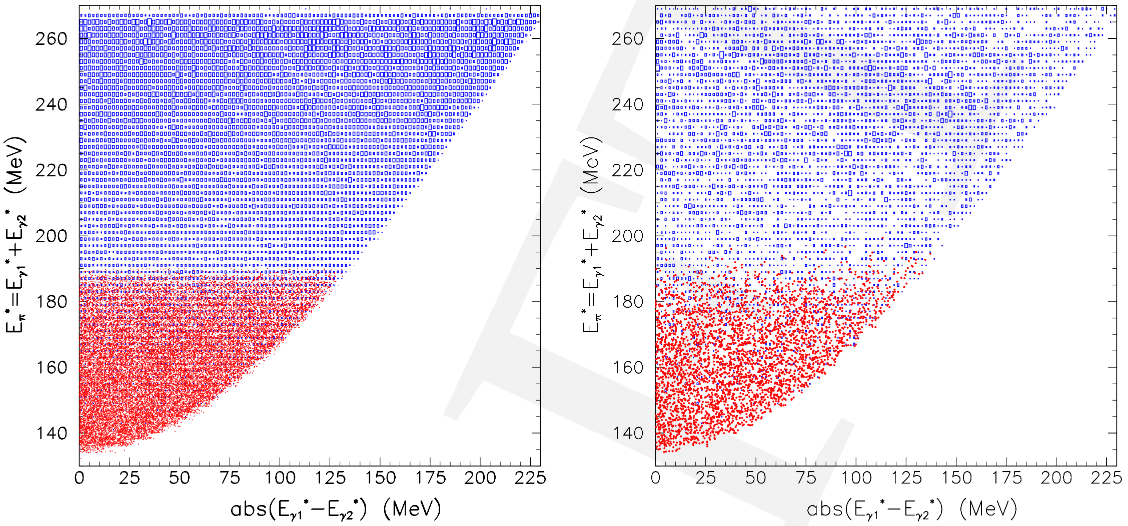

Fig. 84. $E^*_{\pi^0}$ versus $|E^*_{\gamma 1} - E^*_{\gamma 2}|$ plot for $K_{\pi 3}$ background (red dots)and signal (blue squares). Left plot shows the case of perfect resolution and right that of expected resolution.

$K_L^0 \to \pi^- e^+ \nu$ (K_{e3})

The K_{e3} background can arise when the π^- and e^+ react via charge exchange before they are detected and two photon clusters (each with one or two photons) remain. In making background estimates for KOPIO, we will use the inefficiencies for electrons and positrons measured by Inagaki et al. along with estimates of the pion charge exchange cross sections.

Fortunately, there are two extra kinematic handles on the K_{e3} background: the two photon mass ($m_{\gamma\gamma}$), which tends to be much larger than m_{π^0} and the energy of the two photons in the kaon rest frame ($E^*_{\pi^0}$) which tends to be at the end point of the phase space. Due to the use of a low energy beam, the photons from $\pi^- p \to n\pi^0$ can be identified as two photon clusters, which provides the extra rejection power needed to suppress this mode.

Figure 85(a) shows the π^0 momentum distribution produced by the $\pi^- p \to n\pi^0$ reaction for the K_{e3} background. Here, we conservatively assume that only those events below 250 MeV/c can be rejected by the photon clustering cut. Figure 85(b) and (c) show $m_{\gamma\gamma}$ and $E^*_{\pi^0}$ distributions for the signal and K_{e3} background. Selecting the phase space region below the $K_{\pi 2}$ peak in the $E^*_{\pi^0}$ distribution is particularly effective.

Overall, the $K_L^0 \to \pi^- e^+ \nu$ background is expected to be 0.02 events.

$K_L^0 \to \gamma\gamma$

$K_L^0 \to \gamma\gamma$ is very tightly constrained by kinematics. For example, by knowing the direction of one photon, one obtains the energies of both photons and the direction of the other photon. Cutting on the monochromatic photon energies in the kaon rest frame (E^*_γ) using an invariant mass cut on 2 photons($m_{\gamma\gamma}$) and the CM energy of the 2 photons ($E^*_{\pi^0}$), brings this

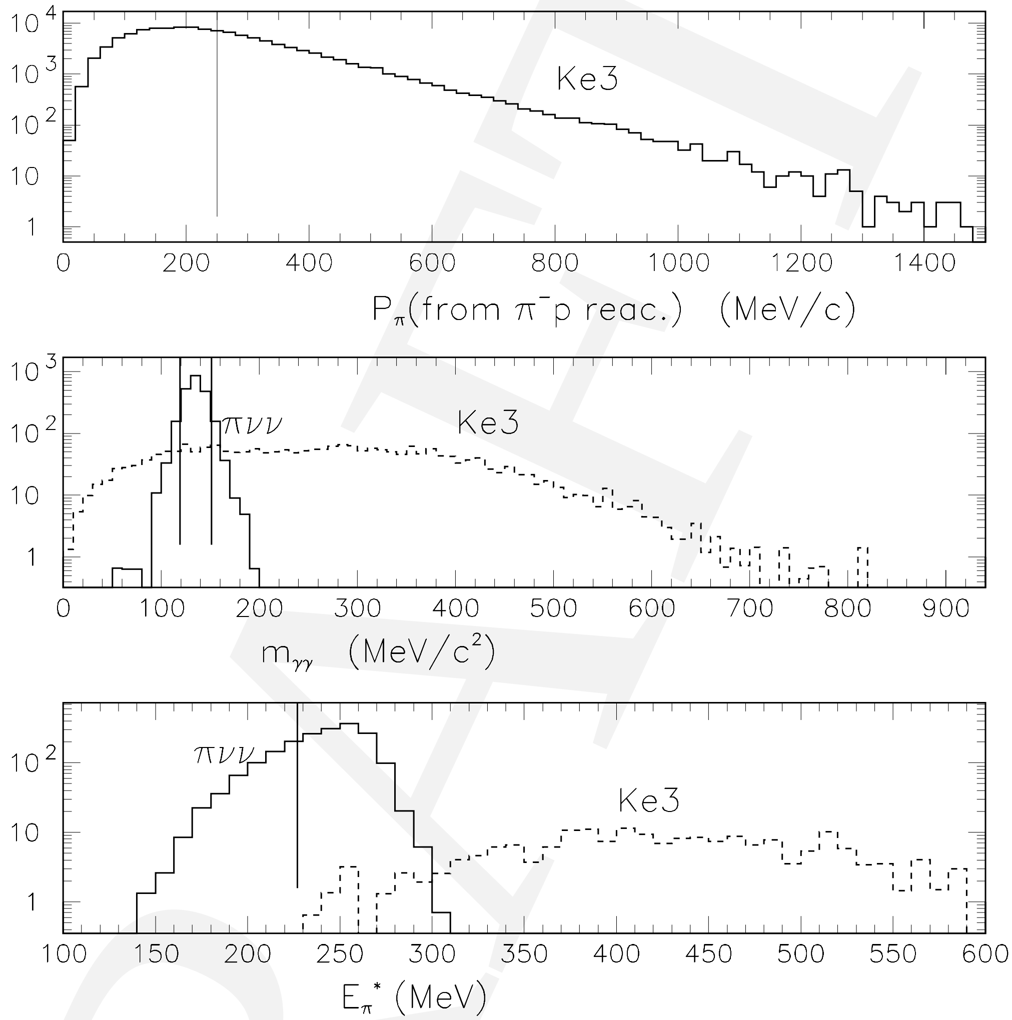

Fig. 85. (a) Momentum of π^0, (b) invariant mass of 2 “photon” energy clusters ($m_{\gamma\gamma}$) and the (c) the center of mass energy of the two photons ($E^*_{\pi^0}$) of the K_{e3} background.

process under control. We expect 0.02 events from this background source.

$K_L^0 \to \pi^\pm e^\mp \nu\gamma$

Background from $K_{e3\gamma}$ (principally $K_L^0 \to \pi^- e^+ \nu\gamma$) can occur when the positron converts asymmetrically before detection in the scintillator of the charged veto lining the inner wall of the vacuum vessel and the π^- is missed. This is shown schematically in Figure 86. Large suppression of this background is achieved by application of the charged veto to the π^-. The two photon mass is the most effective kinematic tool in suppressing this background and cuts on $E^*(\pi)$ and $|E^*_{\gamma 1} - E^*_{\gamma 2}|$ designed for suppression of $K_{\pi 3}$ and $K_{\pi 2}$-odd backgrounds are also effective (Figure 87). To a good approximation, in the $e^+e^- \rightarrow \gamma_0\gamma_1$ annihilation process, $p(\gamma_1) \approx p(e^+)$ and $p(\gamma_0) \approx p(e^-)$. Some background suppression is also achieved both by the poorer χ^2 of the vertex fit due to the change in direction of γ_1 with respect to the e^+ and the possibility of vetoing the lower energy photon (γ_0). To calculate the $K_{e3\gamma}$ background rate, we used a veto inefficiency for the π^- of approximately $\overline{\epsilon}_{\pi^-}$ = 1.5×10^{-4}.[‡§] The $K_{e3\gamma}$ background is expected to produce 4.4 events.

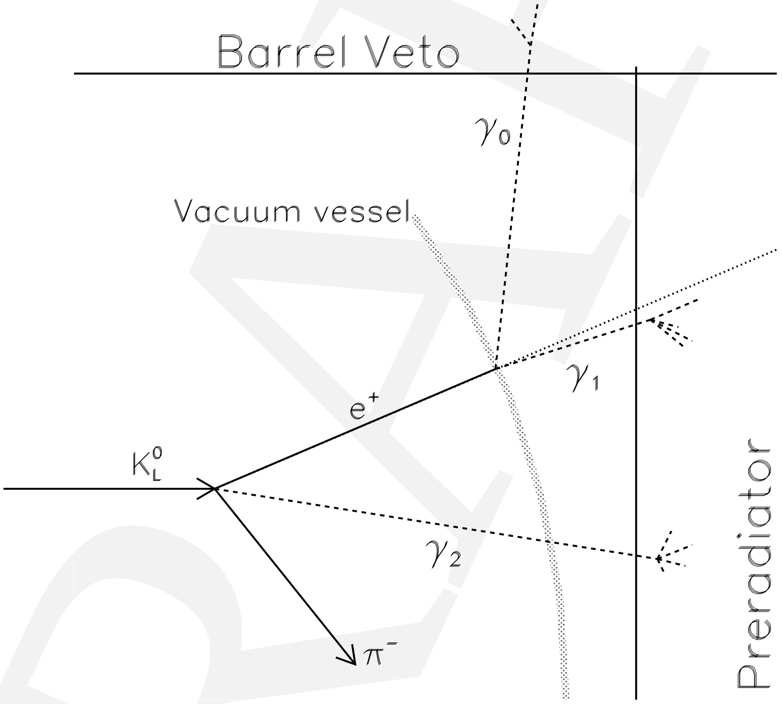

Fig. 86. Schematic representation of origin of the $K^0_L \rightarrow \pi^\pm e^\mp \nu\gamma$ background.

[‡§] To approximate the influence of the $\pi^- C \rightarrow nn$ cross section we use $\overline{\epsilon}_{\pi^-}$ = $1.5 \times 10^{-4} + 1.5 \times 10^{-2}/\max(200, P_e[\mathrm{MeV}/c])$ for the π^- and the approximation $\overline{\epsilon}_{\pi^-}$ = $0.05/E_e(\mathrm{MeV})$ for the positron to account for the annihilation cross section in 1.5 mm of scintillator. The angular and energy dependence of the annihilation photons is taken from the e^+C annihilation cross section. In addition, the angle between γ_0 and γ_1 must be at least 20° for γ_0 to be considered as a veto.

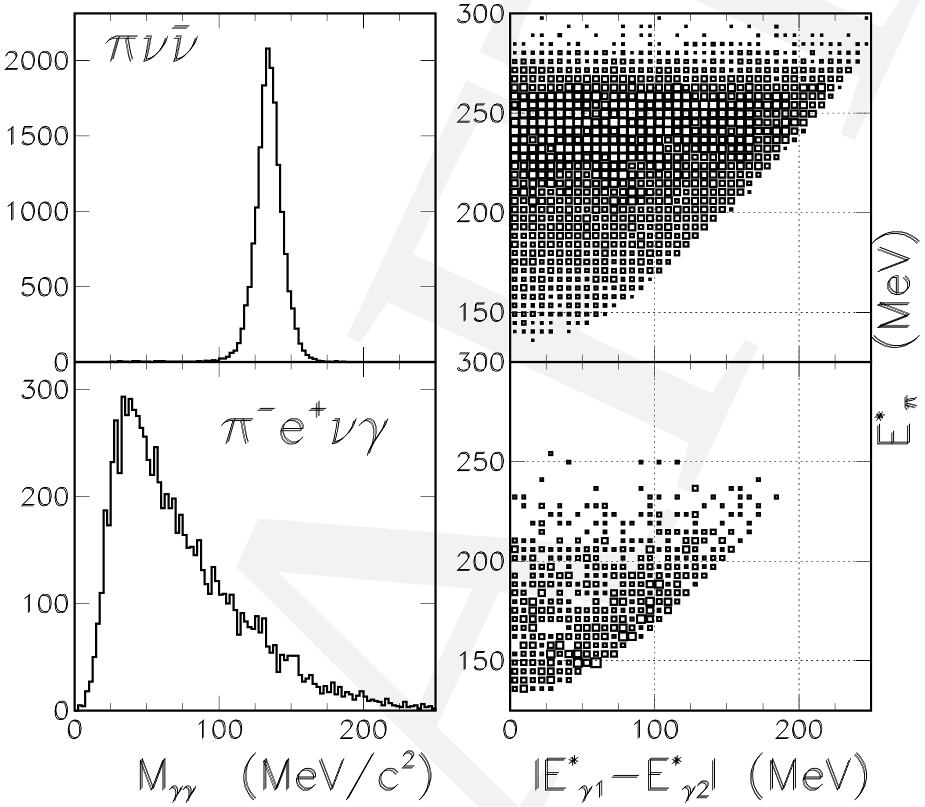

Fig. 87. Two photon mass (left) and $E^*(\pi)$ *vs.* $|E^*_{\gamma1} - E^*_{\gamma2}|$ (right) for $K^0_L \to \pi^0\nu\bar{\nu}$ (upper) and $K^0_L \to \pi^\pm e^\mp \nu\gamma$ (lower).

$\Lambda \to \pi^0 n$

Because of the large angle of the neutral beam used here, the cross section for producing Λs is low and they decay completely before reaching the decay volume. Backgrounds could arise from Λ's produced by halo neutrons and K^0_L's. Again, the production cross section of Λs by the beam halo is low because the beam is soft and it is hard for Λs to reach the fiducial decay volume from the interaction point. Good collimation of the beam as well as a vertex cut to eliminate events produced near the surface of the last collimator suppresses this background to a negligible level of 0.01 events.

$nA \to \pi^0 A$

Neutrons interacting with the residual gas in the decay volume can produce single π^0s without any other easily detectable activity. This background is primarily suppressed by having an excellent vacuum (10^{-7} torr) and by the reduced number of neutrons above the π^0 production threshold (800MeV/c) at the 45 degree production angle. The micro-bunching of the beam provides further suppression of the neutrons as illustrated in Fig. 88 which shows the arrival time of K_L^0's and neutrons with respect to photons at 10m from the production target. Neutrons with momenta between 0.76 and 2.64 GeV/c fall into our arrival time of interest (i.e. K_L^0 with momenta between 0.4 and 1.4 GeV/c). Within this time window, the neutron to K_L^0 ratio is reduced by a factor of 5. Despite the fact that a low energy beam is used here, the effective n/K_L^0 ratio is as good as or better than in higher energy experiments. This background is further suppressed by the kinematic cuts used for $K_L^0 \rightarrow \pi^0\pi^0$ because it includes a large unphysical kinematical phase space due to the miss-assignment of an incoming neutron as a K_L^0. We expect 0.2 events from this background source.

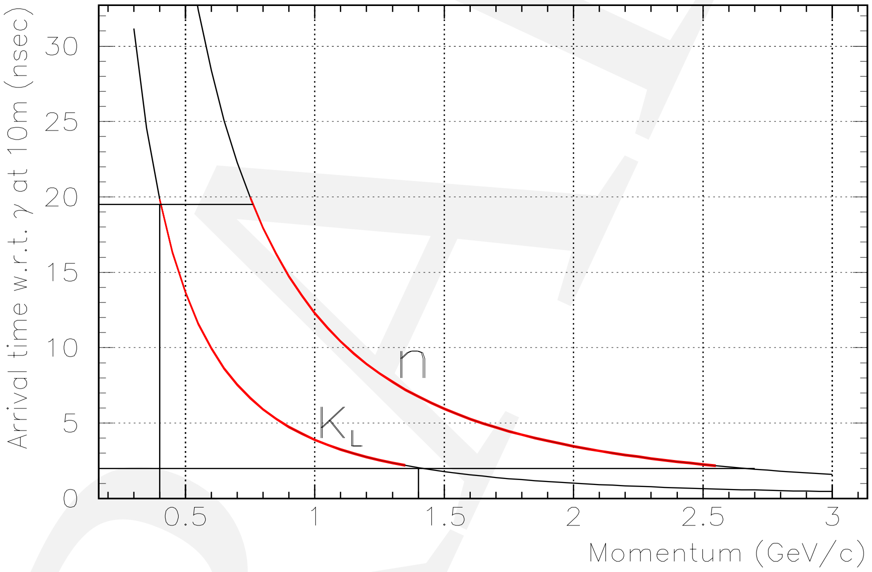

Fig. 88. Arrival time of K_L^0's and neutrons with respect to photons at 10m downstream from the production target.

8.2 Accidentals

Accidental backgrounds are caused by beam halo neutrons, photons and K_L^0's which are scattered from the last collimator and get into the detector. Multiple stages of collimation of the narrow vertical beam should provide good collimation. From our measurements and GEANT calculations of our beam, confirmed by our correct simulation of the E791 beam, we would expect to bring the neutrons, kaons and gammas scattered into the detector down to ~1MHz, 100 KHz, and 10 KHz, respectively. Requiring the converted track in the preradiator further suppresses neutrons and K_L^0s because they show different track characteristics from photon conversions in the preradiator. Finally, photon tracking allows us to reject those photons coming from the upstream collimators.

Assuming the signal event coincidence timing window of 1 ns, the rate of the accidental background is estimated to be ~ 0.8 events.

8.3 Sensitivity and Measurement Precision.

Our estimates of sensitivity for $K_L^0 \rightarrow \pi^0 \nu \bar{\nu}$ decay are tightly coupled to the cuts required for background suppression, particularly for the $K_L^0 \rightarrow \pi^0 \pi^0$ and $K_{\pi 3}$ backgrounds. Fig. 89 illustrates the KOPIO methodology based on kinematic reconstruction in the K_L^0 c.m. system. On the left is a pure kinematic scatter-plot of c.m. pion energy ($E^*_{\pi^0}$) vs. the difference of gamma energies in the c.m. system ($|E^*_{\gamma 1} - E^*_{\gamma 2}|$), for the $K_{\pi 2}$ background (blue dots) and $K_L^0 \rightarrow \pi^0 \nu \bar{\nu}$ (red dots). Regions 1, 2 and 3 are free of background. Now, even when the resolution and acceptance effects are included in the simulations, Regions 1 and 2 remain virtually background free as indicated on the right hand plot in Fig. 89.

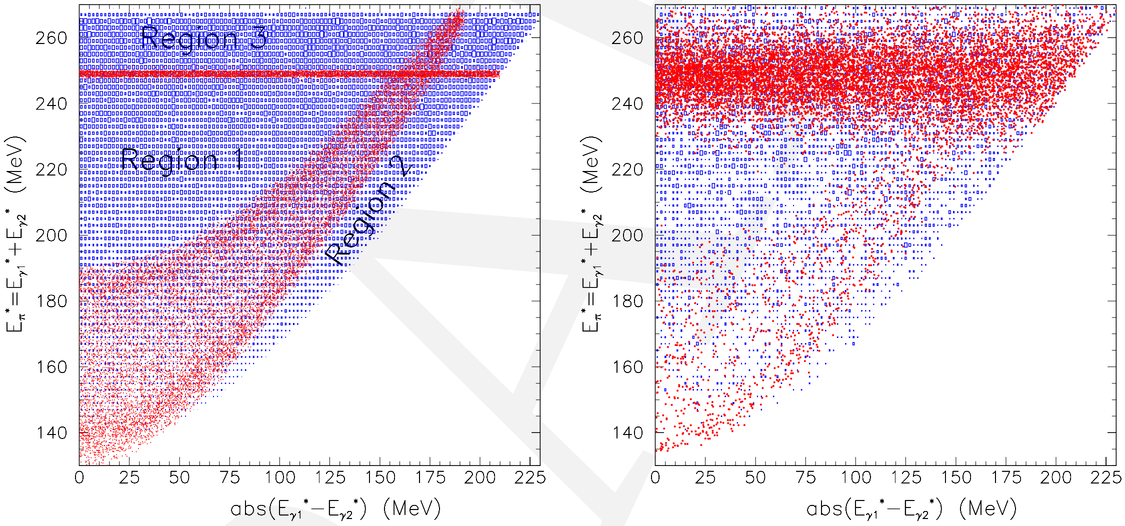

Fig. 89. $E^*_{\pi^0}$ vs. $|E^*_{\gamma 1} - E^*_{\gamma 2}|$ for the $K_{\pi 2}$ background (red dots) and signal (blue boxes). The left hand figure shows the pure kinematic effects while the right hand figure includes experimental resolution effects.

Table 17 gives the breakdown leading to the estimated acceptance for $K_L^0 \rightarrow \pi^0 \nu \bar{\nu}$ with two photons converting in the preradiator. The list includes factors for the 2.75 m long Z fiducial region and the K_L^0 momentum cut (0.4 GeV/c $< P_K <$ 1.4 GeV/c), the solid angle acceptance, the conversion and reconstruction of two photons in the preradiator, and the accessible $K_L^0 \rightarrow \pi^0 \nu \bar{\nu}$ phase space (E^*_π) acceptance. In addition, there are cuts on missing energy and mass and on photon energy sharing. The inefficiency due to accidental spoiling of good events is estimated to be 8% for a threshold of a few MeV in the preradiator, calorimeter and barrel veto, 300 MeV in the catcher, and a timing window of 2 ns. Including the estimated accidental loss, the overall detection efficiency becomes 7.3×10^{-3}. Accepting the cases where one photon converts in the preradiator and one in the calorimeter increases the overall acceptance to ϵ=8.7×10^{-3}.

The acceptance can be estimated for a variety of cut selections and levels of signal/noise

Table 17. Acceptance factors for $K_L^0 \to \pi^0\nu\bar{\nu}$ (two photons converting in the preradiator).

Requirement	Acceptance factor
Z fiducial region and P_K	0.47
Solid angle	0.27
Preradiator Conversion Probability	0.50
$m_{\gamma\gamma} = m_\pi$	0.70
E^*_π	0.26
Wrap-around/$K_{\pi 3}$ low energy	0.82
Photon veto	1.000
E^*_π vs. $\lvert E^*_{\gamma 1} - E^*_{\gamma 2}\rvert$	0.83
Acceptance	7.9×10^{-3}

(S/N). For the nominal $K_L^0 \to \pi^0\nu\bar{\nu}$ and background acceptance estimates given above, we have included events in which at least one of the photons converts in the preradiator. The signal yield is calculated as follows:

$$\begin{aligned}
N_K &= (2.6 \times 10^7\ K_L^0 \text{ decays/pulse}) \cdot 0.65(single\ decay) \cdot (9.2 \times 10^6 \text{ pulses}) \\
&= 1.55 \times 10^{14}\ K_L^0 \text{ decays} \\
N_{\pi\nu\bar{\nu}} &= N_K \cdot \epsilon \cdot \mathrm{B} \\
&= (1.55 \times 10^{14}) \cdot (8.7 \times 10^{-3}) \cdot (3 \times 10^{-11}) \\
&= 41 \text{ events}
\end{aligned}$$

where B= 3×10^{-11} is the SM central value for the branching ratio. The figure 0.65 is the fraction of unaccompanied K_L^0 decays assuming a 25 MHz microbunching frequency and a 2.4 s spill. A total AGS cycle time of 4.7 seconds is assumed. We expect to measure 41 $K_L^0 \to \pi^0\nu\bar{\nu}$ events in 12000 hours of beam. The single event sensitivity of the experiment would be approximately 10^{-12} if not limited by background. A summary of the signal and background estimates is given in Table 18. For the nominal cuts scenario, the signal would exceed the background by about a factor of 2.

8.3.1 Conclusions and Outlook

In estimating the signal and background values given in the previous section, efficiencies and resolutions based on measurements have been used. Energy resolutions, timing resolutions, and position and angular resolutions have been verified by test beam studies. In particular, the photon veto efficiencies assumed for KOPIO are based on modest extrapolations of the tagged-photon measurements made in E787. If, however, more optimistic photon veto expectations were to be used (such as those assumed in the KAMI proposal, Ref. 4, which are based on extrapolations from measurements of photo-nuclear processes), the KOPIO photon veto power would be improved by an order of magnitude. In that case, it is estimated that KOPIO would observe about 80 events with a signal to background ratio of 5-10.

Table 18. Estimated event levels for signal and backgrounds.

Process	Modes	Main source	Events
$K_L^0 \to \pi^0\nu\bar{\nu}$			41
K_L^0 decays ($\bar{\gamma}$)	$\pi^0\pi^0$,$\pi^0\pi^0\pi^0$,$\pi^0\gamma\gamma$	$\pi^0\pi^0$	12.8
$K_L^0 \to \pi^+\pi^-\pi^0$			0.65
$K_L^0 \to \gamma\gamma$			0.02
K_L^0 decays ($\overline{charge}$)	$\pi^\pm e^\mp\nu$,$\pi^\pm\mu^\mp\nu$,$\pi^+\pi^-$	$\pi^-e^+\nu$	0.02
K_L^0 decays ($\bar{\gamma}, \overline{charge}$)	$\pi^\pm l^\mp\nu\gamma$, $\pi^\pm l^\mp\nu\pi^0$,$\pi^+\pi^-\gamma$	$\pi^-e^+\nu\gamma$	4.4
Other particle decays	$\Lambda \to \pi^0 n, K^- \to \pi^-\pi^0, \Sigma^+ \to \pi^0 p$	$\Lambda \to \pi^0 n$	0.01
Interactions	n, K_L^0, γ	$n \to \pi^0$	0.2
Accidentals	n, K_L^0, γ	n, K_L^0, γ	0.8
Total Background			18.9

While the background rejection may be better by as much as an order of magnitude, it is unlikely to be worse. Pathological (rare failure) cases were studied and it was found that there are enough redundancies built into the KOPIO method to deal with them. In addition, using the approach of a “bifurcated analysis” developed in E787, in which separate independently measured factors are used to obtain reliable background predictions, confidence is obtained in the ability to recover from unexpected problems. In case the hardware does not perform as well as expected, backgrounds are still found to be under control at a modest cost of acceptance. A crude estimate of the uncertainty factor on the background estimates would be $1^{+0.25}_{-0.9}$.

There are also possibilities that the acceptance can be increased from the estimates given above. As indicated in Appendix A, the barrel photon veto system can also serve as a pointing calorimeter for low energy, large angle photons from K_L^0. If it can be demonstrated that the backgrounds are controllable, an additional factor of two gain in acceptance may be realized.

Since we expect that the actual background levels will be determined reliably from the data, it will be feasible to select the cuts in order to optimize the precision of the extraction of the $K_L^0 \to \pi^0\nu\bar{\nu}$ branching ratio, and to demonstrate the stability of the result at varying levels of background suppression. For example, by tightening the cut on E_π^* vs. $|E_{\gamma1}^* - E_{\gamma2}^*|$ (see Table 18) the number of events could be reduced from 41 to 26 while the S/N ratio would increase from 2 to 3.

Figure 90 shows a plot of the numbers of events obtainable with various S/N ratios for KOPIO’s nominal parameters and also the precisions obtainable on B($K_L^0 \to \pi^0\nu\bar{\nu}$), at the SM central value. A 10% uncertainty on the background subtraction has been assumed. If the other relevant CKM parameters were known well, it would then be possible to extract η with a precision of approximately 10% from the KOPIO measurement of $K_L^0 \to \pi^0\nu\bar{\nu}$.

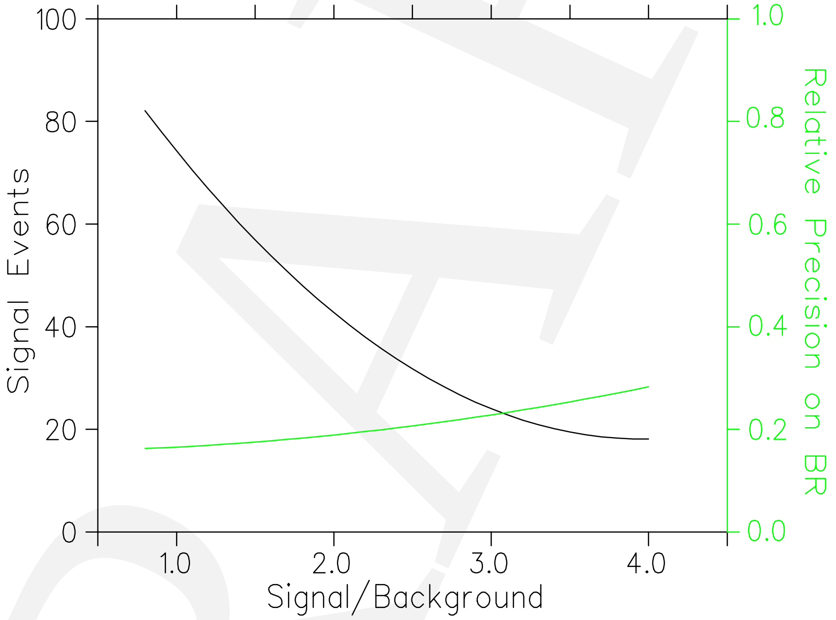

Fig. 90. Number of signal events (S) vs. Signal/Noise (S/N) using standard assumptions. On the right scale is shown the precision of the B($K_L^0 \rightarrow \pi^0\nu\bar{\nu}$) measurement.

APPENDIX A

A The barrel veto as a photon calorimeter

The motivation for using the veto barrel as a calorimeter is presented in Table 19. The table reflects the purely kinematic distribution of photons from $K_L^0 \to \pi^0\nu\bar{\nu}$ decays in a 4 m long decay region. The simulation was done with the real momentum spread of the neutral kaon beam. The inner size of the veto barrel is 3.5×3.5 m^2, the length is 4.2 m. The acceptance of γs in the preradiator is calculated as a geometrical solid angle without taking into account the beam hole region, which would reduce this acceptance. Moreover, the detection efficiency of the preradiator is limited by its radiation thickness. We are interested in recovering the events in which 1 γ hits the preradiator and the other is detected by the veto barrel. The angular distributions for events of various categories are shown in Fig. 91. Assuming the good angular resolution of the preradiator we can tolerate moderate angular resolution for the veto barrel. The photons detected in the barrel are emitted at an average angle of 70°, whereas the corresponding average of those detected in the preradiator is $\sim 2°$. The measuring accuracy on the kaon vertex depends linearly on the distance between the decay point and the photon interaction position. Both factors, the near-normal photon incidence and the constant distance between beam and the barrel, favor the reconstruction of the kaon decay vertex from the photon angle measured in the barrel. Using these 'mixed' events the total acceptance of the detector can be increased almost by a factor of 2. The main concern in the barrel is shower separation. We have to develop the algorithm for reliable identification of two photons which overlap or fuse in the barrel. In such a case $K_L^0 \to \pi^0\pi^0$ decay can appear as background to $K_L^0 \to \pi^0\nu\bar{\nu}$ if one photon is missed. One of the ways to suppress this background is the condition that the photon's transverse and longitudinal distribution of energy be consistent in shape with that of a typical electromagnetic cluster.

Table 19. Geometrical acceptance of photons from $K_L^0 \to \pi^0\nu\bar{\nu}$.

Pattern	Fraction, %
2γ in preradiator	37.2
1γ in preradiator, 1γ in barrel veto,	37.8
2γ in barrel veto	18.2
1γ in preradiator, 1γ in upstream veto	4.8
1γ in barrel veto, 1γ in upstream veto	1.8
2γ in upstream veto	0.1

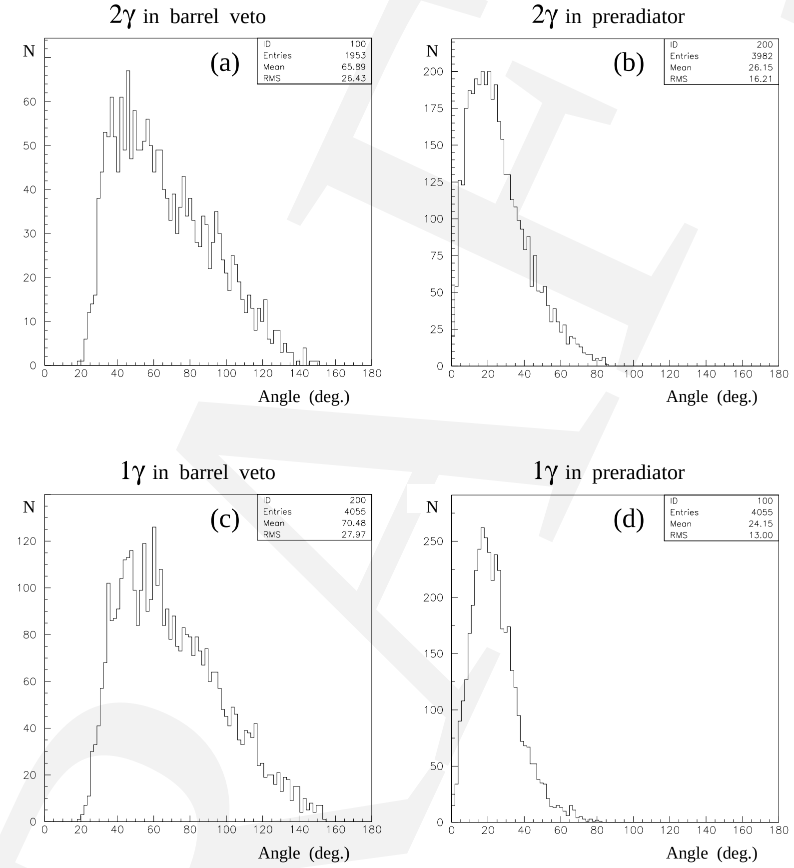

Fig. 91. The angular distribution of photons from $K_L^0 \to \pi^0 \nu \bar{\nu}$ decays for events when (a) both γs hit the barrel veto, (b) both γs hit the preradiator. The latter two plots refer to the case when one γ hits the barrel veto and one hits the preradiator. In this case (c) shows the distribution of the γ hitting the barrel veto and (d) shows the distribution of the γ hitting the preradiator. The angle is that between the photon and the z–axis.

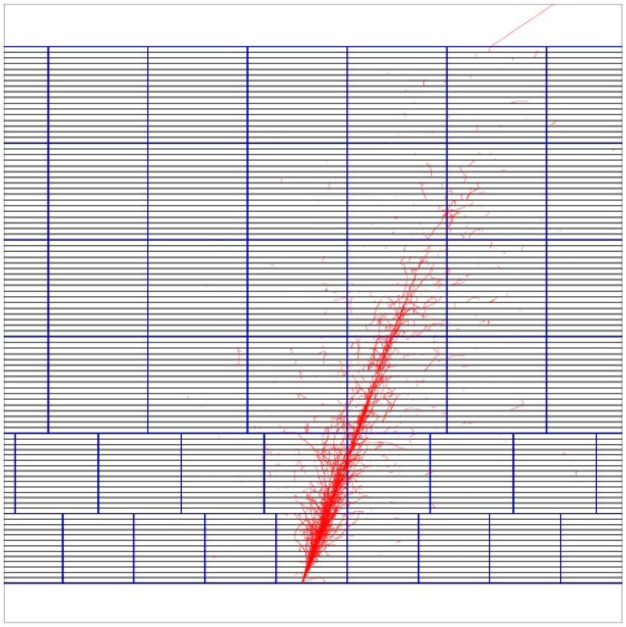

Fig. 92. Shower distribution of simulated 100 MeV photon which strikes the barrel sandwich at $\sim 20^\circ$.

While achieving the requisite time and energy resolutions seems to be rather a technical issue, the angular resolution needed for π^0 kinematic reconstruction (and corresponding for measuring the K_L^0 momentum) is a critical parameter in the proposed apparatus. The basic idea of the angle measurement is shown in Fig. 92. The coordinates in the plane displayed are measured by the center-of-gravity method. The coordinates along the modules are measured by the time difference between the signals from the two ends of that module.

Reducing the lead thickness to 0.5 mm, we can build the sandwich detector with the performance of a calorimeter. Sampling fluctuations which dominate the energy resolution are estimated by GEANT for a photon at normal incidence to be well below 3%/$\sqrt{E}$ for 7 mm thick scintillator layers (see Fig. 52). Here only sampling and leakage fluctuations contribute to the visible energy spread. Therefore these results limit the best resolution that can be achieved for the segmentation considered.

Shower development over the barrel depth is shown in Fig. 93 for a module composed of 11 layers, each of which is 0.5 mm lead plus 4 mm plastic scintillator. Half of the energy is deposited in the first 40 layers, and the rest in the next 130 layers.

The increase in cost of the detector with 0.5 mm thick lead comes mainly from the larger number of the WLS fibers, which are at least doubled with respect to the case of 1 mm thick lead. For cost considerations the modules in the outside section of the barrel can be made with a rough sampling structure (1 mm thick lead) without significant loss in energy resolution. The number of layers combined into one module determines the readout segmentation in the barrel thickness and consequently the number of phototubes.

The requirement for time resolution is 70 ps/$\sqrt{E_\gamma[GeV]}$. This value is sufficient for an accurate measurement of the K_L^0 momentum via the time-of-flight technique, allowing momentum resolution of a few percent.

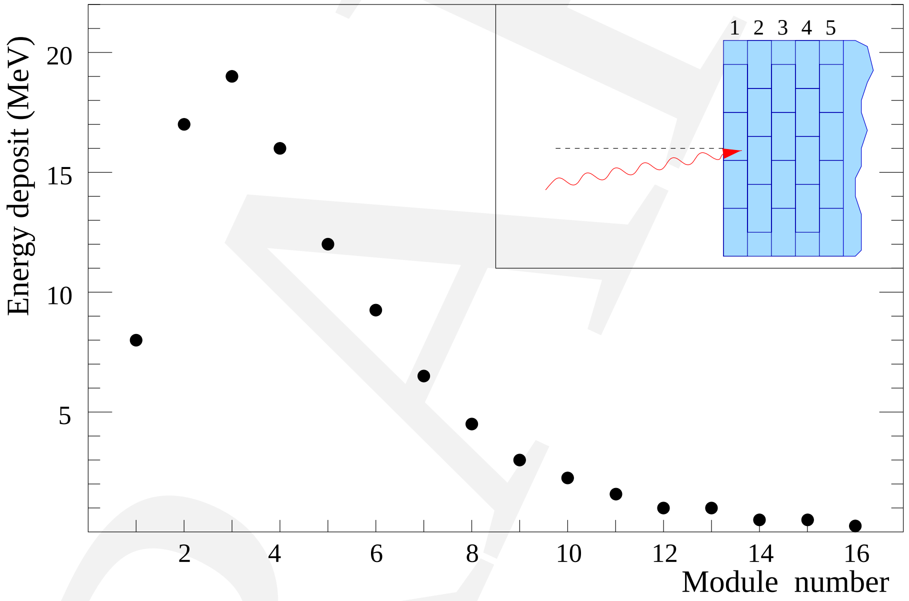

Fig. 93. The energy deposited in the sandwich modules along the barrel thickness. The simulated 250 MeV photon hits the barrel at an angle of 10°. The summed energy visible in a scintillator is about 100 MeV.

REFERENCES

Section-01

1. S. Adler *et al.*, *Phys. Rev. Lett.*, 84, 3768 (2000).
2. G. Buchalla and A.J. Buras, *Nucl. Phys.* **B548**, 309 (1999) hep-ph/9901288.
3. M.K. Gaillard and B.W. Lee, *Phys. Rev.* **D10**, 897 (1974); J. Ellis, M.K. Gaillard and D.V. Nanopoulos, *Nucl. Phys.* **B109**, 213 (1976); L. Littenberg, *Phys. Rev.* **D39**, 3322 (1989).

Section-02

1. M.K. Gaillard and B.W. Lee, *Phys. Rev.* **D10**, 897 (1974); J. Ellis, M.K. Gaillard and D.V. Nanopoulos, *Nucl. Phys.* **B109**, 213 (1976); L. Littenberg, *Phys. Rev.* **D39**, 3322 (1989).
2. A.R. Barker and S.H. Kettell, Ann. Rev. Nucl. Part. Sci. **50**, 249 (2000); L. Littenberg and G. Valencia, Ann. Rev. Nucl. Part. Sci. **43**, 729 (1993); B. Winstein and L. Wolfenstein, Rev. Mod. Phys. **65**, 1113 (1993); J.L. Ritchie and S.G. Wojcicki, Rev. Mod. Phys. **65**, 1149 (1993); G. Buchalla, A.J. Buras and M.E. Lautenbacher, Rev. Mod. Phys.**68**, 1125 (1996).
3. A.J. Buras and R. Fleischer, in *Heavy Flavours II*, World Scientific, eds. A.J. Buras and M. Linder, 65-238 (1997).
4. D. Rein and L.M. Sehgal, Phys. Rev. **D39**, 3325 (1989); G. Buchalla and G. Isidori, Phys. Lett. **B440**, 170 (1998).
5. W.J. Marciano and Z. Parsa, Phys. Rev. **D53**, R1 (1996).
6. G. Buchalla and A.J. Buras, Nucl. Phys. **B400**, 225 (1993).
7. M. Misiak and J. Urban, Phys. Lett. B **451**, 161 (1999) [hep-ph/9901278].
8. G. Buchalla and A.J. Buras, Nucl. Phys. **B548**, 309 (1999) hep-ph/9901288.
9. C. Jarlskog and R. Stora, Phys. Lett. **B 208**, 268 (1988).
10. G. Buchalla and A.J. Buras, Nucl. Phys. **B412**, 106 (1994).
11. S. Adler *et al.*, Phys. Rev. Lett. **79**, 2204 (1997).
12. S. Adler *et al.* [E787 Collaboration], Phys. Rev. Lett. **84**, 3768 (2000) [hep-ex/0002015].
13. M. Gronau, Phys. Lett. **B300**, 163 (1993).
14. A.J. Buras, Phys. Lett. **B333**, 476 (1994).
15. A. J. Buras, P. Gambino, M. Gorbahn, S. Jager and L. Silvestrini, hep-ph/0007085.
16. Y. Zhou and Y. Wu, Mod. Phys. Lett. A **15**, 185 (2000) [hep-ph/0001106].
17. C. Dib, D. London and Y. Nir, Int. J. Mod. Phys. **A6**, 1253 (1991).
18. Y. Grossman, Y. Nir, and R. Rattazzi, in *Heavy Flavours II*, eds. A.J. Buras and M. Lindner, World Scientific Publishing Co., Singapore, 755-794 (1997) hep-ph/9701231.
19. G. Buchalla and A. J. Buras, Phys. Lett. B **333**, 221 (1994) [hep-ph/9405259].
20. G. Bélanger, C.G. Geng and P. Turcotte, Phys. Rev. **D46**, 2950 (1992).
21. C.E. Carlson, G.D. Dorata and M. Sher, Phys. Rev. **D54**, 4393 (1996) hep-ph/9606269.
22. Y. Nir and M. Worah, Phys. Lett. **B423**, 319 (1998).
23. Z. Xiao, C. Li and K. Chao, Eur. Phys. J. **C10**, 51 (1999) hep-ph/9903348.
24. Y. Kiyo, T. Morozumi, P. Parada, M.N. Rebelo, and M. Tanimoto, Prog. Theor. Phys. **101**, 671 (1999) hep-ph/9809333.

25. Y. Grossman and Y. Nir, Phys. Lett. **B398**, 163 (1997).
26. T. Hattori, T. Hasuike, and S. Wakaizumi, *Phys. Rev.* **D60**, 113008 (1999).
27. A.J. Buras, A. Romanino, and L.Silvestrini, Nucl. Phys. **B520**, 3 (1998).
28. G. Colangelo and G. Isidori, JHEP **09**, 009 (1998) hep-ph/9808487 (1998).
29. A.J. Buras and L.Silvestrini, Nucl. Phys. **B546**, 299 (1999) hep-ph/9811471.
30. A.J. Buras, G. Colangelo, G. Isidori, A. Romanino and L. Silvestrini, supersymmetry," Nucl. Phys. B **566**, 3 (2000) [hep-ph/9908371].
31. A. Alavi-Harati *et al.* [KTeV Collaboration], Phys. Rev. Lett. **83**, 22 (1999) hep-ex/9905060.
32. V. Fanti *et al.* [NA48 Collaboration], neutral kaon," Phys. Lett. B **465**, 335 (1999) [hep-ex/9909022].
33. S. Bosch, A.J. Buras, M. Gorbahn, S. Jager, M. Jamin, M.E. Lautenbacher, and L. Silvestrini, Nucl. Phys. B **565**, 3 (2000) [hep-ph/9904408].
34. S. Plaszczynskiand M-H. Schune, hep-ph/9911280 (1999).
35. M. Brhlik, L. Everett, G.L. Kane, S.F. King and O. Lebedev, *Phys. Rev. Lett.* **84**, 3041 (2000).
36. M.S. Chanowitz, hep-ph/9905478(v2) (1999).
37. Z. Xiao, L. Lu, H. Guo, and G. Lu, *Eur. Phys. J.* **C7**, 487 (1999) .

[1] for a recent review, see A.R. Barker and S.H. Kettell, Ann. Rev. Nucl. Part. Sci. **50** , 249 (2000)

[2] J. Gasser and H. Leutwyler, Ann. Phys. **B158**, 142 (1984)
J. Gasser and H. Leutwyler, Nucl. Phys. **B250**, 465 (1985)

[3] D. Ambrose *et al*, Phys. Rev. Lett. **84**, 1389 (2000)

[4] H. Burkhardt *et al.*, Phys. Lett. **B199**, 139 (1987)

[5] V. Fanti *et al.*, Phys. Lett.**B458**, 553 (1999)

[6] A. Alavi-Harati *et al.*, http://*kpasa.fnal.gov*:8080/*public/pubps/ktev/prl_mmg_v4_4.ps*, submitted to Phys. Rev. Lett. (Jan 2001)

[7] A. Lai *et al.*, paper submitted to the 30th International Conference on High Energy Physics, Osaka 2000, hep-ex /0006040(2001)

[8] A. Alavi-Harati *et al.*, http://*kpasa.fnal.gov*:8080/*public/pubps/ktevk4e_prl_final.ps*, submitted to Phys. Rev. Lett. (Feb 2001)

[9] B. Quinn, in Proc. Meet. DPF, Columbus OH, August 2000 Singapore: World Sci(2001)

[10] L. Bergström, E. Massó and P. Singer, Phys. Lett. **131B**, 229 (1983)

[11] G. D'Ambrosio, G. Isidori and J. Portols, Phys. Lett. **B423**385 (1998)

[12] see, e.g., J.F. Donoghue *et al.*, Phys. Rev. **D51**, 2187 (1995)

[13] KTEV collab., A. Alavi-Harati *et al.*, Phys. Rev. Lett. **83**, 917 (1999)
NA48 collab., M. Contalbrigo, in J. Tran Thanh Van, ed. Proc. XXXV Rencontres de Moriond, Les Arcs, France, March 2000, Paris: Ed. Frontieres (2000)

[14] G. D'Ambrosio *et al.*, Nucl. Phys.**B492**417 (1997)

[15] P. Heiliger *et al.*, Phys. Lett. **B327**, 145 (1994)

[16] G.D. Barr *et al.*, Phys. Lett. **B358**, 399 (1995)

[17] P. Heiliger and L.M. Sehgal, Phys. Lett. **B307**, 182 (1993)

[18] G. Ecker, H. Neufeld and A. Pich, Nucl. Phys. **B413**, 321 (1994)

[19] G.D. Barr *et al.*, Phys. Lett. **B328**, 528 (1994)

Section-03

1. A. Alavi-Harati, *et al.*,, Phys. Rev. **D** 61, 072006.

Section-04

1. R. Cappi and Ch. Steinbach, IEEE Trans. Nucl. Sci. **NS-28** 2806 (1981); J.W. Glenn *et al.*, Proc. Particle Accelerator Conf., 967 (1997); J.W. Glenn *et al.*, Proc. Particle Accelerator Conf. 1258 (1999).
2. K. Brown, M. Blaskiewics, H. Brown and K. Reece, Technical Note No. **445**, Accelerator Division, AGS Department, Brookhaven National Laboratory (1996).

Section-05

5.1

1. C. Albajar *et al.*, Nucl. Instr. Meth. A364 (1995) 473.
2. G.S. Atoyan *et al.*, KOPIO technote 16, November, 2000.
3. Northern State Metal Corp.
4. http://www-hep.phys.emu.edu/cms/Welcome_archives_99.html.
5. Y. Arai, Nucl. Instr. Meth. A453 (2000) 365.
6. CMS Muon Technical Design Report, CERN/LHCC97-32 (1997), P175.

5.2

1. G.S. Atoyan, *et al.*, “Lead-scintillator electromagnetic calorimeter with wave length shifting fiber readout”, NIM, **A320**, 144 (1992)
2. G. David, *et al.*, “Performance of the PHENIX EM Calorimeter”, PHENIX Technote 236 (1996).
3. A. Golutvin, “Electromagnetic calorimeter for HERA-B”, HERA-B Tech. Note 94-073 (1994).
4. Technical Proposal, CERN LHCC 98-4, LHCC/P4, 20Feb. 1998.
5. G.S. Atoyan, *et. al.*, “Preliminary Research of Shashlyk Calorimeter for E926”, E926 Technote (1999).
6. A.L.Wintenberg et al., PHENIX Project, internal paper, 2000.
7. The LHCb Technical Proposal. CERN/LHCC 98-4.
8. The Front-End Electronics for LHCb calorimeters, LHCb 2000-028.
9. Zero dead-time charge sensitive shaper for calorimeter signal processing, LHCb 2000-041.
10. N. Harnew *et. al.*, Nucl. Instr. and Meth.**A279**, 290 (1989).
11. R. Appel *et. al.*, Nucl. Instr. and Meth. in Physics Res., (in print).
12. W.L. Reiter *et. al.*, Nucl. Instr. and Meth.**173**, 275 (1980).
13. A. Fyodorov *et. al.*, Nucl. Instr. and Meth. in Physics Res. **A413**,352-356 (1998).

5.3

1. W.R. Gibbs, and B.F. Gibson, Ann.Rev.Nucl.Part.Sci.**37** (1987) 411.
2. D. Ashery, and J.P. Schiffer, Ann.Rev.Nucl.Part.Sci.**36** (1986) 205.
3. T. Inagaki *et al.*, Nuc. Inst. and Meth. **A 359**, (1995) 478-484.
4. Internal report presented by P. Robmann, *http://pubweb.bnl.gov/people/e926/meetings/dec00/robmann.pdf*

5.4

1. W. Hofman et al. Nucl. Instr. and Meth. 195 (1982) 475.
2. M. Atiya et al. Nucl. Instr. and Meth. A321 (1992) 129.
3. M. Antonelli et al. Nucl. Instr. and Meth. A379 (1996) 511.
4. G. David et al. IEEE Trans. Nucl. Science NS–43 (1996) 1491.
5. A. Bodek, P. Auchincloss, Nucl. Instr. and Meth. A357 (1995) 292.
6. A. Ivashkin et al. Nucl. Instr. and Meth. A394 (1997) 321.
7. R. Wojcik et al. Nucl. Instr. and Meth. A342 (1994) 416.
8. Bicron Corporation, 12345 Kinsman Rd., Newbury, OH 44065 USA.
9. S. Belikov et al. Instr. and Exper. Technique, Vol. 39, No.4 (1996) 498.
10. V. Ananiev et al. IHEP Preprint 97–1, Protvino, 1997.
11. V. Brekhovskikh et al. Instr. and Exper. Technique, Vol. 38, No.6 (1995) 767.
12. Yu. Kudenko et al. Nucl. Instr. and Meth., (2001) to be published.

5.5

1. E. Aschenauer *et al.*, “OPTICAL CHARACTERIZATION OF N = 1.03 SILICA AEROGEL USED AS RADIATOR IN THE RICH OF HERMES.”, Nucl. Instrum. Meth. A **440**, 338 (2000).

Section-06

Section-07

1. CDF/D0 VRB board: http://www-ese.fnal.gov/eseproj/svx/vrb/vrb.pdf.
   STAR: http://daq.star.bnl.gov/ daq/HARDWARE/RB
   PHENIX reference??

Section-08

1. S. Ajmura et al., KEK preprint 97-243.
2. T. Inagaki et al., NIM A359 (1995) 478.
3. R. D. Ransome, et al., Phys. Rev. C 46 (1992) 273.
4. T. Yamanaka, talk at Kaon Decay Workshop for Young Physicists, KEK, Japan, Feb.14-16, 2001.